

UNIVERSITY OF OKLAHOMA
GRADUATE COLLEGE

NONLINEAR PROCESSES IN HOT SODIUM VAPORS AND
SODIUM SPINOR BOSE-EINSTEIN CONDENSATES FOR
ENTANGLEMENT GENERATION

A DISSERTATION
SUBMITTED TO THE GRADUATE FACULTY
in partial fulfillment of the requirements for the
Degree of
DOCTOR OF PHILOSOPHY

By
QIMIN ZHANG
Norman, Oklahoma
2021

NONLINEAR PROCESSES IN HOT SODIUM VAPORS AND
SODIUM SPINOR BOSE-EINSTEIN CONDENSATES FOR
ENTANGLEMENT GENERATION

A DISSERTATION APPROVED FOR THE
HOMER L. DODGE DEPARTMENT OF PHYSICS AND ASTRONOMY

BY THE COMMITTEE CONSISTING OF

Dr. Arne Schwettmann, Chair

Dr. Alberto M. Marino

Dr. Bruno Uchoa

Dr. Bin Wang

© Copyright by QIMIN ZHANG 2021
All Rights Reserved.

Acknowledgements

I would like to acknowledge many people who helped me through this amazing journey. Thanks to my doctoral committee members, Dr. Arne Schwettmann, Dr. Alberto M. Marino, Dr. Bruno Uchoa and Dr. Bin Wang for bringing me to this place through wise counsel and excellent instruction. Special thanks to my advisor, Dr. Arne Schwettmann, for his knowledge, guidance, and encouragement. I could not have done this without his help.

Next, I would like to thank my research team, Shan Zhong, Hio Giap Ooi, and Isaiah Morgenstern, for their friendship and dedicated team work. I thank Dr. Alberto M. Marino, Saesun Kim, and Timothy Woodworth for their insights and help on the four-wave mixing experiment. I also benefited from weekly meetings and discussions with Dr. Doerte Blume, Dr. Jianwen Jie and Dr. Qingze Guan.

Last but not least, I would like to express my gratitude to my parents and sister, for their endless love and unconditional support all the time. I would like to thank my beloved wife Qian Wang, who has been with me through good moments and bad, shined my life with her optimism and smile, and encouraged me during every dark moment I encountered. I also thank our daughter Hanna, who was born while I was writing this thesis, for bringing joy during the Covid pandemic and making me understand the meaning of love, responsibility, and family. I dedicate this thesis to them.

Table of Contents

List of Tables	viii
List of Figures	xviii
Abstract	xix
1 Introduction	1
1.1 Overview	1
1.2 Generating Entangled Photons in Hot Na Gases	2
1.3 Generating Entangled Atoms in Ultracold Na Gases	4
1.4 Outline of the Thesis	6
2 Theory of Four-Wave Mixing	8
2.1 Squeezed States of Light	8
2.1.1 Single-Mode Squeezed States	8
2.1.2 Two-Mode Squeezed States	15
2.2 Nonlinear Response of an Optical Medium	17
2.3 Four-Wave Mixing in Hot Na Vapors	20
2.4 Double-Lambda Configuration	22
3 Simulation of Four-Wave Mixing in Hot Na Vapors	25
3.1 Description of the Susceptibilities	25
3.2 Phase-Matching Condition	30
3.3 Four-Wave Mixing Gain Calculation	32
3.4 Summary	36
4 Experimental Setup for Four-Wave Mixing in Hot Na Vapors	38
4.1 Laser System	38
4.2 Four-Wave Mixing Beam Setup	42
4.3 Vapor Cell Oven	45
4.4 Signal and Noise Detection	47
4.5 Summary	47
5 Experimental Results on Four-Wave Mixing in Hot Na Vapors	48
5.1 Calibration of Shot Noise Limit	48
5.2 Four-Wave Mixing Gain Characterization	50
5.3 Four-Wave Mixing Noise Measurements	54
5.4 Saturated Absorption Light	55
5.5 A New Vapor Cell Design	59
5.6 Summary and Outlook	60
6 Theory of Spin-Mixing in Na Spinor BECs	62
6.1 Introduction to BEC	63
6.2 Spin-Mixing Hamiltonian	65
6.3 Laser Cooling and Trapping	70

6.3.1	Doppler Cooling	70
6.3.2	Magneto-Optical Trap	73
6.3.3	Optical Dipole Trap and Evaporative Cooling	77
6.4	Microwave Dressing	78
6.5	Interferometry Sequence	81
7	Quantum Interferometry with Microwave-Dressed $F=1$ Spinor Bose-Einstein Condensates: Role of Initial States and Long Time Evolution	85
7.1	Introduction	85
7.2	Computational Method	87
7.2.1	Full Quantum Evolution	88
7.2.2	Truncated Wigner Approximation (TWA)	89
7.2.3	Interferometer	91
7.3	Results	94
7.3.1	Comparison of TWA Evolution and Chebyshev Evolution	94
7.3.2	Simulation for Non-Seeded Initial States	96
7.3.3	Simulation for Seeded Initial States	97
7.4	Discussion	102
7.5	Conclusion and Outlook	104
8	Experimental Setup for Spinor BECs	106
8.1	Vacuum System	107
8.2	Optical Setup	112
8.2.1	Optics Layout	112
8.2.2	MOT Setup	115
8.2.3	Bias Coils	118
8.2.4	Optical Dipole Trap Setup	121
8.3	Imaging System	123
8.3.1	Absorption Imaging	123
8.3.2	Imaging System	124
8.4	Microwave and rf System	129
8.4.1	Signal Generation	130
8.4.2	Antenna	132
8.5	Control System	134
9	Experimental Results of Spinor BECs	137
9.1	Creating BECs in an All-Optical System	137
9.2	Initial State Preparation	140
9.3	Microwave-Dressed Spin Evolutions	144
9.4	Matter-Wave Interferometry Based on Spinor BECs	146
9.5	Discussion and Outlook	151
10	Conclusion and Outlook	152
	References	155

A Publications	165
A.1 Introduction	165
A.2 Publications	165
A.3 Presentations	165

List of Tables

8.1	Parameters of anti-Helmholtz coils.	117
-----	---	-----

List of Figures

1.1	A proposal to apply squeezed twin beams to absorption imaging of our spinor BEC. The probe and conjugate beams are used as probing and reference beams respectively. The intensity difference reveals the amount of absorption by the atomic cloud, and can be used to infer the number and density of BEC atoms.	3
2.1	Classical representation of electric field \mathbf{E} for monochromatic light in phase space. Here X and Y are quadratures. Both quadratures are perfectly accurate, so the representation is a point.	9
2.2	Representation of uncertainties of a single-mode electric field \mathbf{E} for monochromatic light in phase space. Here X and Y are quadratures. The shaded area are uncertainties associated with the quadratures.	10
2.3	Representation of the vacuum state of a single mode of light in phase space. Here X and Y are quadratures. The shaded area represents the uncertainties associated with the quadratures, with $P(X)$ and $P(Y)$ the probability distributions, which follow a Gaussian distribution for the vacuum state. . .	11
2.4	Representation of a coherent state of a single-mode of light in phase space. A coherent state is a displaced vacuum state with non-zero mean photon number and the same noise distributions. Here X and Y are quadratures. The shaded area represents the uncertainties associated with the quadratures, with $P(X)$ and $P(Y)$ the probability distributions, which follow Gaussian distributions for a coherent state.	12
2.5	Representation of a squeezed state of a single-mode light in phase space. Here X and Y are quadratures. The shaded area represents the uncertainties associated with the quadratures. Here, the uncertainty of Y is squeezed, and the uncertainty of X is anti-squeezed, but they still obey the Heisenberg uncertainty principle.	14
2.6	A schematic of a squeezed coherent state created by applying the squeezing operator $\hat{S}(\zeta)$ and displacement operator $\hat{D}(\alpha)$ on the vacuum state $ 0\rangle$. . .	15
2.7	(a) Quadrature fluctuations of individual fields \hat{E}_1 and \hat{E}_2 . (b) Joint quadrature fluctuations showing squeezing in \hat{X}_- and \hat{Y}_+ , as well as anti-squeezing in \hat{X}_+ and \hat{Y}_-	16
2.8	(a) Frequency doubling process, in which two photons at frequency ω are absorbed and a single photon at frequency 2ω is generated. (b) Parametric down conversion process, in which one photon at frequency ω is absorbed while two photons at frequencies ω_a and ω_b are emitted, the frequencies satisfy $\omega = \omega_a + \omega_b$	18
2.9	(a) Third harmonic generation process, in which three photons at frequency ω are absorbed and a single photon at frequency 3ω is generated. (b) Four-wave mixing process, in which two photons at frequencies ω_1, ω_2 , are absorbed while two new photons at frequencies ω_3 and ω_4 are emitted, the frequencies satisfy $\omega_1 + \omega_2 = \omega_3 + \omega_4$	20

2.10	(a) ^{23}Na D_1 line, showing the energy spacing between the ground state $3^2S_{1/2}$ and the excited state $3^2P_{1/2}$, and the corresponding hyperfine structures. (b) Measured absorption spectrum of the D_1 line at about 150 °C, showing the Doppler broadening and the two resonant absorptions from $F = 1$ and $F = 2$ of the ground state to the excited state, respectively.	21
2.11	Double- Λ scheme on sodium D_1 line. Δ and δ are the one-photon detuning and two-photon detuning, respectively. The hyperfine levels of the excited state are not resolved due to Doppler broadening at high temperatures. . .	23
2.12	Experimental schematic of 4WM beams. A weak seeding probe beam and an intense pump beam propagate and intersect inside a hot ^{23}Na vapor cell with an angle θ . Balanced photodiodes and a spectrum analyzer are used to measure the relative noise between generated probe and conjugate fields. SA: spectrum analyzer.	24
3.1	Energy level diagram of ^{23}Na D_1 line, showing the double- Λ configuration with a single pump beam field \mathbf{E}_0 and probe/conjugate field $\mathbf{E}_p/\mathbf{E}_c$, respectively. Ω , Ω_p , Ω_c are the Rabi frequencies of the couplings via pump, probe, and conjugate field, respectively.	26
3.2	Direct χ_{pp} , χ_{cc} (a, b) and cross χ_{pc} , χ_{cp} (c, d) susceptibilities for the probe and conjugate fields as a function of the two-photon detuning δ , in units of the excited state decay rate $\gamma = 2\pi \times 9.79$ MHz. The blue solid lines are the real parts, and the red dashed lines are the imaginary parts. The one-photon detuning is $\Delta_1 = 80\gamma$, and the ground state decoherence rate is set to $\gamma_c = 0.5\gamma$.	29
3.3	Direct susceptibility χ_{pp} as a function of δ over a larger range of detunings. The large one-photon resonance appears at $\delta \approx 100\gamma$	30
3.4	Illustration of the geometric phase matching condition. (a) In free space the matching condition is fulfilled ($\Delta k_z = 0$) when all beams are co-propagating. The wave vector sum of the probe and conjugate is equal to the two wave vectors of the pump. (b) The refractive index of the medium, n_p , changes the effective length of the probe wave vector, which results in a phase mismatch. By introducing an angle θ between the probe and the pump beam, the effective phase-matching condition is fulfilled. (c) $\Delta k_z > 0$ when effective phase-matching condition is fulfilled with $n_p > 1$	31
3.5	Simulated gain behavior of probe (G_p) and conjugate (G_c) over a range of δ and θ . Here $\Omega = 69\gamma$, $\Delta_1 = 80\gamma$	34
3.6	Calculated gain of the probe and conjugate beams as functions of two-photon detuning δ and probe-pump angle θ for different pump Rabi frequencies. (a) $\Omega = 60\gamma$, (b) $\Omega = 69\gamma$, (c) $\Omega = 80\gamma$	35
4.1	(a) Absorption profile for laser spectroscopy of Na D_2 line when pump beam is off. The two strong absorption regions are Doppler-broadened transitions between the $3^2S_{1/2}, F = 2$, $3^2S_{1/2}, F = 1$ ground state and the $3^2S_{1/2}, F' = 1, 2, 3$ excited states respectively. (b) Absorption profile for saturated absorption spectroscopy of Na. It resembles the profile from regular laser spectroscopy but with added Lamb dips.	39

4.2	Bottom trace (grey): closer view of the probe beam signal for transitions involving the $F = 2$ ground state. Top trace (red): the output error signal from the lock-in amplifier after FM modulation of the pump beam with an AOM. We choose the first positive to negative zero crossing point (at 0 MHz relative frequency in this figure), which is the maximum point of the probe signal, to be our locking point.	41
4.3	Experimental setup for FM-modulated saturated absorption spectroscopy. The pump beam (red line) and probe (blue line) are derived from the main laser. The pump is frequency shifted and FM modulated through an AOM to allow tuning of the lock point and lock-in detection with a derivative signal.	42
4.4	Experimental setup for 4WM experiment. The pump beam (red line) is derived from the main laser, with part of it frequency shifted through an AOM and used as the probe beam (green line) to seed the 4WM process. The probe beam is coupled into a single-mode polarization-maintaining fiber and propagates through the Na vapor cell at an angle θ with respect to the pump beam. The 4WM relative intensity noise is measured by subtracting the probe beam intensity from the conjugate beam intensity using a balanced detector. An attenuator is used on the probe beam to balance the intensities of the probe and conjugate beams.	43
4.5	Home-built oven used to adjust vapor cell temperature. (a) Picture of the oven positioned on the optical table. (b) Schematic of the oven design. Within the oven, a lens tube with two anti-reflection coated windows is used to hold the Na cell. Heat is transferred to the lens tube through heaters adhered to the outside of the tube. Mineral wool insulation is used between the oven and lens tube to prevent heat dissipation. The heaters are connected to a PID controller to keep the temperature constant. The temperature is monitored by thermocouples placed at the two ends and center of the lens tube (not shown here).	46
5.1	Illustration of shot noise calibration. (a) Experimental setup for balanced beam shot noise detection. The first waveplate and PBS are used to purify the light polarization, while the second waveplate and PBS are used to balance the beam powers. (b) Measured shot noise spectrum at a total power of 80 mW.	49
5.2	Measured shot noise limit as a function of power. The shot noise power is linear in the power of the laser light, as expected.	50
5.3	The response of probe and conjugate beams when the one-photon detuning (Δ) is scanned across the 4WM resonance spectrum. The probe spectrum without pump field (black solid) shows the Doppler-broadened absorption profile. The probe signal with pump field on (blue dash-dotted) shows the probe gain of the 4WM process. The conjugate signal (red dashed) is only observed when the pump field is applied. Here, the conjugate signal was shifted by ~ 3.4 GHz to illustrate where the conjugate frequency lies in the Doppler broadened absorption profile.	51

5.4	Dependence of probe gain on pump power and cell temperature. The probe was measured at a two-photon detuning $\delta = -11$ MHz, pump beam waist $w_p = 490 \mu\text{m}$, probe beam waist $w_{pr} = 264 \mu\text{m}$, input probe power $170 \mu\text{W}$ and probe-pump angle $\theta = 0.12^\circ$. The one-photon detuning Δ , was optimized at each data point for maximum gain. Each trace corresponds to a different pump power, as shown in the legend.	52
5.5	Dependence of probe gain on one-photon detuning Δ and two photon detuning δ	53
5.6	Measured noise spectrum of individual probe and conjugate beams, the relative intensity noise and the shot noise limit. Here, the cell temperature $T = 160$ °C, the probe-pump angle $\theta = 0.12^\circ$, and two-photon detuning $\delta = -11$ MHz. One-photon detuning was optimized for the lowest relative noise.	55
5.7	Experimental setup with an on-resonance saturating beam. The saturating beam is counter-propagating with the conjugate beam at the same frequency, to saturate the atomic absorption and reduce conjugate absorption loss. . .	56
5.8	4WM signals and noise with saturated absorption light. (a) Probe and conjugate intensities with and without saturated absorption light vs. time. (b) Saturated absorption light reduces the relative noise. The results suggest that by applying saturated absorption light, the gain of the probe and conjugate beams can be enhanced, and their relative noise can be reduced.	58
5.9	Vapor pressure of (a) Na and (b) Rb. The dashed lines are the corresponding vapor pressure at temperature $T = 120$ °C. Models are Eq. (1) in Ref. [45, 48].	59
5.10	The new stainless steel cell design. The main part of the system is made of stainless steel so it can work at much higher temperatures than a glass vapor cell. The removable sodium cup can contain more sodium material so that it lasts longer, and refills easily. The two anti-reflected coated sapphire windows can work at high temperatures with little reflection and without destructible reactions with hot Na vapor.	60
6.1	Cartoon of the phase transition to a BEC. At high temperatures, the inter-atomic distance is much larger than their wavelength, and atoms can be treated as classical particles. As the gas is cooled down, the wave nature becomes more dominant. At a critical temperature T_c , the atomic wavefunctions overlap and start to form a BEC. At zero temperature, the atoms form a pure BEC. Figure inspired by Ref. [60].	64
6.2	Cartoon of a spin-exchange collision. Two $m_F = 0$ atoms collide and change into a pair of entangled $m_F = \pm 1$ atoms.	66
6.3	Schematic of a quench process illustrated with pair-energy diagrams. Left: Effective quadratic Zeeman shift of F=1 spinors in the presence of a constant background magnetic field. The effective quadratic Zeeman shift $q > 0$, $q \approx h \times 277 \text{ Hz/G}^2$. Right: The system is quenched by a microwave field such that it is switched to $q < 0$. The curves with arrows means that spin-exchange collisions cause reversible population transfer between the $m_F = 0$ and the $m_F = \pm 1$ states.	69

6.4	Cartoon of scattering force: (a) an atom encounters a resonant photon with momentum $\hbar k = \hbar/\lambda$; (b) the atom absorbs the photon, and is slowed by $\hbar k/m$; (c) the atom re-radiates a photon in a random direction. During many cycles, the average momentum change by this radiation is zero, so on average the atom slows down.	71
6.5	Schematic of magnetic field gradient along z direction, and two-level energy diagram.	74
6.6	Schematic of one-dimensional MOT. A magnetic field gradient that has a value of zero at the trap center shifts excited state energy levels up or down depending on the position of the atoms. Counter-propagating laser beams with opposite circular polarizations are red-detuned. The selection rule for transitions between substates due to the Zeeman shift leads to an imbalanced radiative force. The force depends on position in such a way that it pushes atoms towards the center of the trap ($z = 0$).	75
6.7	Schematic of the MOT. Three pairs of circularly polarized laser beams come from three orthogonal directions. Two anti-Helmholtz coils provide an inhomogeneous magnetic field gradient.	76
6.8	Hyperfine structure of sodium ground state manifold in the presence of a constant external magnetic field. Lines with arrows represent the nine allowed transitions between $F = 1$ and $F = 2$ states due to the selection rules. The corresponding polarizations are also labeled. The dashed lines are the degenerate energy levels without Zeeman shift. The resonant frequency between $F = 1$ and $F = 2$ is around 1.7 GHz.	79
6.9	Spin-mixing interferometry sequence in a $F = 1$ spinor BEC. The first step is to prepare the initial state, with most of the atoms in $m_F = 0$ state and some initial seeds in $m_F = \pm 1$ states. The second step, “split”, is to quench to a specific q and let the system evolve. The third step is to apply a quick phase shift φ at time τ and let the system evolve for another time interval τ . The last step is to detect the total number of atoms in $m_F = +1$ and $m_F = -1$ state.	82
6.10	Seeding atoms via rf or microwave pulses. (a) Seeding atoms from the $m_F = 0$ state to the $m_F = \pm 1$ states using a resonant rf pulse. An rf pulse can seed equal number of atoms into $m_F = \pm 1$ states. (b) Seeding atoms from the $m_F = 0$ state to the $m_F = \pm 1$ states using resonant microwave pulses via intermediate states. Microwave pulses can seed $m_F = \pm 1$ states individually.	84
7.1	(Color online) Cartoon of the interferometer sequence with initial seeds. The phase shift $\varphi = \Delta\theta$ is applied via microwave dressing. The straight arrows denote time evolution. The wavy arrow denotes entanglement. The black detectors represent population measurements via Stern-Gerlach time-of-flight absorption imaging at the end of the sequence.	92
7.2	(Color online) Interferometer fringes for different evolution times. Shown is the phase dependence of (a) $\langle N_+ \rangle$ and (b) σ_{N_+} for $\langle N_{\text{inside}} \rangle = 2$ (red solid, left axis), 21 (blue dashed, left axis), 322 (black dash-dotted, right axis). Here, $c/h = 30$ Hz, $q/h = -35$ Hz, $N = 1,000$, and zero initial seed. For longer evolution times (larger $\langle N_{\text{inside}} \rangle$), interferometer fringes become highly non-sinusoidal.	93

7.3	(Color online) Evolutions of $\langle N_+ \rangle$ for the full quantum method (red solid) and TWA method (blue dashed), and evolutions of σ_{N_+} for the full quantum method (red dotted) and TWA method (blue dash-dotted). Shown are evolutions for (a) 0%, (b) 2% , and (c) 10% initial seeds. Here, $N = 1,000$ and $q/h = -2$ Hz. For large initial seeds, the standard deviations predicted by the TWA method are in disagreement with the full quantum method. . .	95
7.4	(Color online) Phase sensitivities for different N with zero initial seed. Shown are $N = 1,000$ (yellow circles), $N = 5,000$ (blue squares), $N = 10,000$ (green triangles), $N = 50,000$ (black diamonds). Here, $q/h = -2$ Hz. The red line depicts sensitivity/SQL = 1. Points below the red line correspond to quantum-enhanced sensitivity. The inset shows a zoomed-in region where enhanced sensitivities are found. The lines are intended as guide to the eye.	97
7.5	(Color online) Phase sensitivities for dual initial seeds (blue squares) and single initial seeds (green circles) with $N = 1,000$, coherent initial state and 2% initial seeds. Here, $q/h = -2$ Hz. The red line depicts the SQL. Points below the red line correspond to quantum-enhanced sensitivities. The lines are intended as guide to the eye.	98
7.6	(Color online) Phase sensitivities for coherent initial state (blue triangles) and Fock initial state (green squares) with $N = 1,000$ and 2% dual initial seeds. $q/h = -2$ Hz. The red line depicts the standard quantum limit. Points below the red line correspond to quantum-enhancement. The coherent initial state performs better than the Fock initial state for all values of $\langle \rho_{\text{inside}} \rangle$. The lines are intended as guide to the eye.	99
7.7	(Color online) Phase sensitivities for different initial seeds of 0% (blue circles), 2% (purple squares), 5% (green triangles), 10% (black diamonds), and 20% (yellow crosses). Here, $N = 1,000$ and $q/h = -2$ Hz. The inset shows a zoomed-in region where enhanced sensitivities are found. The SQL is shown as red solid line. Points below the red line correspond to quantum-enhanced sensitivities. The lines are intended as guide to the eye.	100
7.8	(Color online) Phase sensitivities as a function of $\langle \rho_{\text{inside}} \rangle$ for different total atom numbers $N = 100$ (black circles), $N = 1,000$ (green squares), and $N = 10,000$ (blue triangles), and initial seeds of (a) 0%, (b) 2%, and (c) 10%. Here, $q/h = -2$ Hz. The red line depicts the ratio of sensitivity/SQL = 1. Points below the red line correspond to quantum-enhancement. Even for large atom numbers of $N = 10,000$, quantum-enhancement is still predicted at longer evolution times. The lines are intended as guide to the eye.	101
7.9	(Color online) Interferometer phase shift needed to cause an approximate reversal of spinor dynamics as a function of effective quadratic Zeeman shift q and evolution time τ . Here, we assume a 3% single sided seed. The brightest color means a phase shift of π , and darkest means zero phase shift. The calculation represents an estimate using a semi-classical model following Ref. [107].	103

8.1	CAD drawing of our vacuum system. Following the atomic beam direction (left to right), there are the sodium cup, the sodium oven, the differential pumping chamber, the Zeeman slower, and the main chamber. Ion pumps, titanium sublimation pump and turbo pump (not shown in figure) are attached to the system to maintain UHV pressure. The blue square show the main chamber, with MOT coils and bias coils surrounding it.	108
8.2	Photo of oven chamber taken from the side window. The cold plate has a centered hole which is aligned with the nozzle, and a mechanical shutter in between can shut on/off the atomic flux. The yellow light is the fluorescence of the sodium beam.	109
8.3	Measured magnetic field generated by Zeeman slower coils (black dots) compared to the simulated field (red line).	110
8.4	(a) The 5'' × 10'' optical table that holds the main optical system. (b) The 4'' × 10'' optical table that holds the vacuum system. The laser beams derived from the main optical system are delivered to the vacuum system via optical fibers.	113
8.5	Optical layout for generating cooling, repumping and imaging beams. The abbreviations are AOM: acousto-optic modulator, Q: quarter wave plate, Sat. Abs: Saturated Absorption Spectroscopy, H: half-wave plate, numbers: focal length in mm. All cubes are polarizing beamsplitter cubes. The apertures shown before fibers and in the paths denote mechanical shutters.	114
8.6	Diagram of different laser beam frequencies compared to sodium D_2 line hyperfine structure. Frequencies are not drawn to scale.	115
8.7	Zoom-in of MOT CAD drawing. (a) The MOT cooling and repumping beams shine into the main chamber via four 2.77'' outer diameter viewports on the sides and two 8'' outer diameter viewports on top and bottom. (b) The two anti-Helmholtz coils for the MOT are mounted on the top and bottom viewports. The three pairs of Helmholtz bias coils surrounding the main chamber generate a uniform background magnetic field.	116
8.8	Photos of experimental chamber. A pair of anti-Helmholtz coils for the MOT are mounted on the top and bottom viewports and are wound around black-anodized aluminum frames. Three pairs of Helmholtz bias coils, mounted on blue plastic frames surrounding the main chamber, generate a uniform background magnetic field.	119
8.9	A photo of the trapped atomic cloud in the MOT at the center of the chamber. We use a large MOT cooling beam diameter of 0.8 inches to trap more atoms. Above the cloud, there is the half-dipole antenna for microwave-dressing and a loop antenna for rf radiation. See Sec. 8.4 for more details.	120
8.10	Schematic of our ODT setup. The far-detuned IR light originates from a fiber laser and is focused at the center of the MOT after passing through an AOM. The laser beam exiting the chamber is reflected and focused at the chamber again. The two beam paths crossed at the center of the MOT.	122

8.11	Schematic of our absorption imaging setup. Top and side imaging systems are used to obtain absorption images of the ultracold atomic cloud inside the vacuum chamber. Camera 1 along with lenses L1, L2, L3 and quarter-wave plate (QWP) make up the side imaging system. Camera 2 and associated optics comprise the top imaging system. The positions of the lenses and cameras can be adjusted to change the magnification of the imaging systems for different detection purposes. The focal length of L1, L2, L4 and L5 is $f = 150$ mm, the focal length of L3 and L6 is $f = 50$ mm.	125
8.12	False color images from absorption imaging. (a) The MOT absorption image taken after a few milliseconds of time-of-flight. (b) Time of flight expansion of the optical molasses. The $1/\sqrt{e}$ width was obtained from Gaussian fits to absorption images. The line is a fit to Eq. (8.8). The fit gives a temperature of $65.5 \pm 0.1 \mu\text{K}$. (c) Stern-Gerlach absorption image showing atoms in different spin states after 10 ms time of flight. From left to right are absorption images of $m_F = -1$, $m_F = 0$ and $m_F = +1$ state.	128
8.13	Schematic of microwave and rf transitions. Red, blue and green arrows represent microwave fields coupling to transitions between $F = 1$ and $F = 2$. Black arrows represent rf field coupling to transitions between $F = 1$ Zeeman sublevels.	129
8.14	Schematic of microwave system. The output signal can be controlled remotely on a computer. The FPGA receives data packets and sends input parameters to the DDS, which generates a high-speed tunable sine wave signal at frequencies around 30 MHz. The low frequency sine wave is mixed with a stable, high frequency (~ 1.74 GHz) sine wave via a single-sideband modulator to generate the desired sum frequency (~ 1.77 GHz) sine wave, which is close to the hyperfine splitting of the sodium ground state. After amplification, filtering, and impedance matching, the signal is then emitted from a half-dipole antenna to irradiate trapped cold atoms. FPGA: field programmable gate array. DDS: direct digital synthesizer. SSB: single-sideband modulator. TTL: transistor-transistor logic.	131
8.15	Schematic of rf system. The rf signal generated from a function generator is filtered by a low-pass filter before passing through the rf amplifier. A home-built rf coil antenna is installed inside the vacuum chamber so that it is close to the atoms and therefore can induce strong interactions.	132
8.16	(a) CAD rendering of the microwave and rf antennas mounted inside the vacuum chamber. The microwave antenna is a half-dipole antenna and mounted about 3 cm from the center of trapped atoms inside the vacuum chamber via an electrical feedthrough. The rf antenna is a small copper loop with diameter of 25 mm, and it is also installed close to the center of the atomic cloud to improve the rf intensity at the position of the atomic cloud. (b) A photo of the chamber showing microwave and rf antennas.	133
8.17	A control panel of the LabVIEW interface. There are 24 digital channels with green circles as on/off switches. Bright green represents status on while dark green represents off. There are also 16 analog channels with input boxes. These panels are stacked vertically to create any desired timing sequence, with time increasing towards the bottom.	136

9.1	Empirically optimized experimental dipole trap ramping sequence. The ODT is kept at constant power during the loading phase. It then ramps to its maximum power for a one-second long free evaporation period. Finally, there is a forced evaporation cooling phase where the trap intensity is reduced exponentially until a BEC is formed.	138
9.2	Top view absorption images of ODT. (a) A typical image of our crossed ODT in the presence of MOT atoms at the beginning of free evaporation phase. (b) A typical image of ODT after one-second free evaporation, after most MOT atoms escaped. OD: optical density.	139
9.3	Absorption images taken during the forced evaporative cooling process. The ODT power decreases from (a) to (c). (a) Hot atoms are escaping from the trap and the atomic cloud temperature is reducing. (b) The BEC appears at the center as a sharp density peak. (c) The thermal atoms are escaping from the trap and the BEC fraction is increasing. Finally, a nearly pure BEC is achieved. OD: optical density.	140
9.4	Stern-Gerlach absorption images of sodium atoms in three spin states. (a) and (b) show different spin populations in the three spin states due to different applied rf pulses. The rf pulse amplitude and duration are chosen to transfer certain number of atoms.	141
9.5	Rabi oscillations on resonance for (a) σ_- , (b) σ_π and (c) σ_+ transitions. Shown is the measured number of atoms (black circles) and a sinusoidal fit (red line) in $ F = 1, m_F = 0\rangle$ state versus microwave pulse duration. The fit is used to extract the Rabi frequency of Ω_{σ_-} , Ω_{σ_π} , Ω_{σ_+} . The measurements are done at the maximum microwave power of 20 W.	143
9.6	Spin oscillations at $q/h = -10$ Hz for 2% and 8% seeding in $m_F = \pm 1$ states. Each data point is an average of 5 measurements. Error bars are standard errors.	145
9.7	Spin oscillations at $q/h = 0$ Hz, $q/h = -10$ Hz, $q/h = -15$ Hz for 5% seeding in $m_F = \pm 1$ states. Each data point is an average of 5 measurements. Error bars are standard errors.	145
9.8	Evolution of $N_+ = N_{+1} + N_{-1}$ with microwave pulses applied at $\tau = 4$ ms, $q_{rev}/h = 0$ Hz (red, solid), $q_{rev}/h = -1,200$ Hz (blue, dotted) and $q_{rev}/h = -625$ Hz (yellow, dashed). Shaded region depicts $\pm\sigma_{N_+}$. Here $\langle N \rangle = 1,000$, 2% dual initial seeds, $c/h = 30$ Hz, and $t_{rev} = 0.25$ ms.	147
9.9	Sinusoidal interferometer fringe for evolution time $\tau = 3$ ms. Black circles are experimental data and red line is a sine wave fit. Each data point is an average of five measurements, with error bars represent standard errors. Here we use $q/h = -15$ Hz and 10% initial seeds. The total atom number is about 20,000.	148
9.10	Non-sinusoidal interferometer fringe for evolution time $\tau = 15$ ms. Black circles are average data points of five measurements. The red dots are simulation results using full quantum calculation without adjustable parameters. Our measured results qualitatively agree with the simulations with some discrepancies. Error bars represent standard errors. Here we use $q/h = -15$ Hz and 10% initial seeds. The total atom number is about 20,000.	149

9.11 Interferometer fringe for evolution time $\tau = 15$ ms. Black circles are average data points of five measurements. Here we use $q/h = -10$ Hz, with all the other conditions the same as in Fig. 9.10. 150

Abstract

The primary purpose of this thesis is to study the generation of quantum entanglement via nonlinear processes in hot sodium vapors and ultracold sodium spinor Bose-Einstein condensates. The creation of entanglement can induce quantum squeezing. Such squeezing has important applications for metrology with quantum-enhanced precision beyond the classical limit, known as quantum-enhanced sensing. In this thesis, I present my research on generating quantum entangled states of light in hot atomic vapors via four-wave mixing and generating quantum entangled atoms in ultracold spinor Bose-Einstein condensates via spin-mixing dynamics.

Non-degenerate four-wave mixing (4WM) in a hot atomic vapor cell has been shown to be an effective method to produce quantum entangled states of light. Most of the recent work on entangled states of light has focused on Rb and Cs in the near infrared regime. Generating entangled light near the Na resonance at 589 nm is challenging but beneficial for interfacing with cold gases and atomic sensors based on Na. I present our investigation on 4WM in a double- Λ configuration on the Doppler-broadened D_1 line of ^{23}Na . The construction and characterization of a 4WM apparatus to generate entangled light via hot sodium vapor is introduced. The calculation of susceptibilities in the presence of the light fields and 4WM gain is presented. Experimentally, we characterized the 4WM gain and noise properties of the intensity difference between the generated beams of light. In addition, I discuss directions to boost 4WM gain and reduce absorption loss, including a new design of a stainless steel vapor cell and application of saturated absorption light. The squeezed states of light generated by 4WM can be used to enhance the signal-to-noise ratio of atom number measurements of our sodium spinor Bose-Einstein condensates, where entangled states of atoms can be created via spin-mixing.

A Bose-Einstein condensate (BEC) is a novel state of matter where identical bosonic

particles occupy the same quantum state below an ultracold critical temperature. I present our experimental system for an all-optical production of sodium spinor BECs. We verify that the matter wave coherence of the BEC, where particles share the same quantum wave function and phase, can be extended to the internal spin degrees of freedom in a spin-1 BEC by observing coherent spin-exchange collisions. Spin-exchange collisions in $F = 1$ spinor BECs, where two atoms with magnetic quantum number $m_F = 0$ collide and change into a pair with $m_F = \pm 1$, are useful to implement matter-wave quantum optics in spin space, such as quantum-enhanced interferometry, because the collisions generate entanglement and they can be precisely controlled using microwave dressing. We demonstrate control of the coherent spin evolution by controlling initial states and using microwave dressing fields during the evolution process to apply quenches. Using these control methods, we experimentally investigate atomic interferometry based on spin-exchange collisions in the regime of long evolution times where the Bogoliubov and truncated Wigner approximations break down, and compare the results with our numerical simulations. The results of our atomic interferometry experiments are promising and suggest a pathway to achieve quantum-enhanced sensitivities and/or enhanced sensitivities given the nonlinear nature of our measurements.

Chapter 1

Introduction

This chapter begins with a general overview of quantum entanglement, continues with brief introductions of the topics of four-wave mixing based on hot sodium vapors and spin-mixing in ultracold spinor BECs. The chapter concludes with an outline of the thesis.

1.1 Overview

Entanglement plays a central role in many quantum technologies, such as quantum computing, quantum communication and quantum sensing. Today's most precise classical measurement instruments work above the shot noise limit, the precision bound set by the discrete nature of photons in quantum mechanics. Over the past decades, research on quantum enhanced metrology to overcome the shot noise limit has been developed. The use of quantum squeezing as a resource offers the possibility to perform measurements that have precision beyond the shot noise limit. A widely used technique in recent years is to induce squeezing by “transferring” some of the uncertainty on a variable that is to be measured onto a conjugate variable whose precision is less important. A famous application is the improvement of the sensitivity of LIGO interferometers to detect gravitational waves by using squeezed states of light [1].

Quantum entanglement has been demonstrated on different particles, for example, entangled pairs of photons [2, 3], entangled pairs of atoms [4, 5, 6], and entangled pairs of atom-photon [7, 8]. Here in our lab, we generate entangled photons via hot atomic vapors and entangled atoms via collisions in ultracold Bose-Einstein condensates.

1.2 Generating Entangled Photons in Hot Na Gases

Squeezed light has been shown to be the working horse for many promising quantum technologies. Besides detecting gravitational waves, squeezed light has important applications, for example, in quantum teleportation [9], quantum sensing [10, 11], quantum imaging [12, 13], and many others. Entangled photons can be generated by certain nonlinear optical processes. In 1985, the first experimental realization of squeezed light was observed by generating entangled pairs of photons using a four-wave mixing (4WM) process in an optical cavity, where a twin-beam was generated with a noise squeezing of 0.3 dB [14]. Another successful method is parametric down-conversion (PDC), where a pump photon is incident on a medium with $\chi^{(2)}$ nonlinearity and is converted into two new photons: signal and idler, whose photon numbers are correlated [15]. Other popular systems to generate entanglement and squeezed states of light include optical parametric oscillation (OPO), where the PDC process takes place inside a cavity [16], micro-cavity [17], optical fiber [18] and atomic ensembles [2, 19] to enhance the effective nonlinearities.

In our work, we generate squeezed states of light via a four-wave mixing process in sodium atomic vapors. In this system, a strong pump beam interacts with a weak seeding probe beam efficiently inside the atomic vapor. The output probe beam is amplified and a new conjugate beam is generated simultaneously. With the quantum correlation between the probe and the conjugate fields, the intensity difference squeezing and quadrature entanglement can be established. Since the first recorded squeezed light was generated via four-wave mixing in a sodium vapor with a squeezing of only 0.3 dB, investigations on atomic-based four-wave mixing have led to higher squeezing rates. For example, a squeezing of close to 9 dB was observed in the four-wave mixing process in a hot rubidium vapor [2]. Compared to other methods of generating squeezed light, such as parametric down-conversion in nonlinear

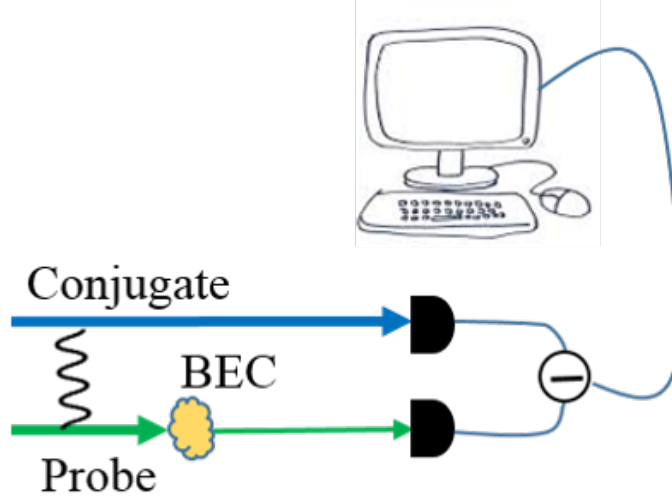


Figure 1.1: A proposal to apply squeezed twin beams to absorption imaging of our spinor BEC. The probe and conjugate beams are used as probing and reference beams respectively. The intensity difference reveals the amount of absorption by the atomic cloud, and can be used to infer the number and density of BEC atoms.

crystals [20, 21], the four-wave mixing could generate light resonant with an atomic transition and narrow-band squeezed light, which is more suitable for applications in atomic experiments.

Our goal is to generate squeezed states of light that is resonant with sodium atoms so that it can be used in our sodium BEC experiment to improve the measurement of the number of atoms in BECs with absorption imaging. In a standard absorption imaging process, a resonant probing laser beam is incident on the BEC and the shadow of the atomic cloud is captured by a CCD camera. The amount of absorption is obtained by comparing the shadow with a reference beam which is supposed to have the same intensity but without absorption. The corresponding number of atoms in the atomic cloud is extracted from the absorption profile. Any intensity difference between the incident probing and reference beam will result in a discrepancy in the number of atoms, the accuracy of which is critical to BEC experiments. Since four-wave

mixing can generate the probe and conjugate beams whose intensity difference noise is reduced, if we apply the probe/conjugate beam into the absorption imaging as the probing/reference beam respectively, it has the potential to reduce the noise and improve the accuracy in the atom number measurement. The concept of this proposal is shown as a cartoon in Fig. 1.1. Interfacing the spinor BEC with quantum states of light will also allow us to study the interaction of quantum states of light with exotic entangled spin states of atoms in the future.

1.3 Generating Entangled Atoms in Ultracold Na Gases

A Bose-Einstein condensate (BEC) is a novel state of matter where identical bosonic particles lose their individuality and act like a collective matter wave when cooled to nearly absolute zero temperature, typically in the nanoKelvin range. The concept of Bose-Einstein condensation dates back to 1924 by Einstein [22], following a study of photon statistics by Bose [23]. Due to the extremely low-temperature requirement, a BEC was not observed experimentally until 1995 using atoms of rubidium [24], and later of sodium [25] and lithium [26], with the help of the new cooling techniques of laser cooling and evaporative cooling. These BECs were in a single spin state known as scalar BECs. The atoms were magnetically trapped allowing only one spin state to be trapped. Therefore, their spin degrees of freedom were frozen. A spinor BEC, however, is a BEC where the spin F is a free variable, and it was first observed in spin-1 ^{23}Na gases in 1998 [27]. Here, F is the total angular momentum, $F = L + S + I$, with L the orbital angular momentum, S the spin angular momentum, and I the nuclear angular momentum.

Research on BECs has been growing rapidly with applications in condensed matter physics, atomic collision physics, quantum computing, quantum simulation and precision measurements. In a BEC, all atoms share an identical spatial wavefunction,

resulting in a macroscopic coherent matter wave. The coherence property was demonstrated by interfering two independent BECs [28]. More observations on BECs, such as Josephson tunneling of BECs between adjacent trapped optical lattices [29], Josephson junctions [30] and quantum phase transitions from a superfluid to a Mott-Insulator [31], show the potential of simulating condensed matter systems by applying the excellent control we can exert on atomic gases.

With the liberated spin degree of freedom in addition to the external ones, spinor BECs provide a platform to study macroscopic quantum systems, whose parameters such as spin, temperature and dimensionality are controllable by laser fields and magnetic fields. The spin-exchange collisions, due to the spin-dependent inter-particle interaction, lead to spin-mixing dynamics and corresponding spin population oscillations. For example, in a $F = 1$ spinor BEC with $2F + 1 = 3$ magnetic sublevels, two atoms in the $m_F = 0$ sublevel can coherently and reversibly collide into a pair of atoms in $m_F = +1$ and $m_F = -1$ sublevels. The difference of populations in the $m_F = \pm 1$ sublevels is preserved throughout this process due to the conservation of total spin, so the $m_F = \pm 1$ atoms are always created in pairs. This suggests the opportunity to create multi-particle entanglement and spin squeezed states via spin-exchange collisions. This process can be compared to four-wave mixing in optics [32]. The possibility to create massively entangled atomic states is of particular interest to scientists for their potential application in quantum information, quantum communication and quantum sensing [33].

In this thesis, I will introduce an all-optical setup to create spinor BECs and the microwave/rf systems used to manipulate spinor BECs. We perform nonlinear atomic interferometry and investigate enhanced sensitivities based on entangled atoms created via controllable spin-mixing dynamics.

1.4 Outline of the Thesis

The main body of this thesis consists of two parts: Part I (Chapter 2-5) introduces the research of four-wave mixing to generate two-mode squeezed states of light via hot sodium vapors, and Part II (Chapter 6-9) describes the study of quantum-enhanced atomic interferometry based on ultracold sodium spinor Bose-Einstein condensates.

Chapter 2 of this thesis describes the basic idea of four-wave mixing. The concepts of squeezed states of light and nonlinearity of the optical medium are introduced. I also introduce the idea of implementing four-wave mixing experiments using hot sodium vapors as the nonlinear optical medium based on the double- Λ configuration.

In Chapter 3, I numerically investigate the atomic susceptibilities of the sodium medium in response to external light fields and the effect of the phase-matching condition. The intensity gain of the probe and conjugate fields is calculated over various parameter regions.

In Chapter 4, I give a detailed explanation of our four-wave mixing experimental setup, including some critical parts such as the laser system, the vapor cell oven and the detection system.

Chapter 5 shows our experimental results of four-wave mixing. The gain and noise measurements are presented, followed by a new oven design and discussion of future improvements.

Chapter 6 to 9 are devoted to the studies of sodium spinor BECs. Chapter 6 introduces the basic theory of BEC, the spin-mixing Hamiltonian, and the laser cooling and trapping methods used. I introduce the tool of microwave dressing as a versatile method to control the spin dynamics. I present the timing sequence to implement nonlinear matter-wave interferometry based on microwave-dressing of spinor BECs.

In Chapter 7, I show simulation explorations of realizing an atomic interferometer with quantum-enhanced sensitivity based on microwave-dressed spinor BECs. Two

computational methods, the full quantum evolution and the truncated Wigner approximation (TWA) are explained and compared. The effect of initial states and long-time evolution on the interferometry sensitivity is investigated.

Chapter 8 details the experimental setup to create spinor BECs and realize atomic interferometry. The design of our vacuum system, optical setup, imaging system and microwave and rf system is presented.

Chapter 9 gives our experimental results of spinor BECs. I explain the generation of spinor BECs in our all-optical system, and the initial state preparation. The results of microwave-dressed spin evolutions and matter-wave interferometry are presented.

Lastly, Chapter 10 concludes this thesis, and provides some possible future research directions.

Chapter 2

Theory of Four-Wave Mixing

Four-wave mixing (4WM) is a nonlinear optical process in which two or three waves interact with each other via a medium producing one or two new waves due to the third order nonlinear susceptibility of the medium. 4WM can be used to create quantum entangled light, which has many applications, for example, in quantum information, [34], quantum imaging [35], optical parametric amplification [36], and more. In this chapter, I introduce the theory of squeezed light, nonlinear optics, and 4WM as an effective way to generate quantum squeezed states of light. I discuss the properties of twin beams produced by 4WM, and our method to realize the 4WM process in hot sodium vapors.

2.1 Squeezed States of Light

2.1.1 Single-Mode Squeezed States

Light is an electromagnetic wave consisting of an electric field and a magnetic field. The electric field $\mathbf{E}(t)$ can be written in terms of X and Y , called quadratures because they differ by $\pi/2$ in phase space, such that

$$\mathbf{E}(t) = 2E_0[X \cos(\omega t) + Y \sin(\omega t)], \quad (2.1)$$

where $E_0 = \sqrt{\hbar\omega/2\epsilon_0V}$, ω is the frequency of the field, ϵ_0 is the permittivity of vacuum and V is the volume in which the field is excited. A classical field of arbitrary amplitude and phase can be described as a phasor, a vector with length denoting its amplitude and angle with respect to the x axis corresponding to the phase, as shown in Fig. 2.1. The electric field could thus be represented as a point in phase space with its magnitude and phase known precisely.

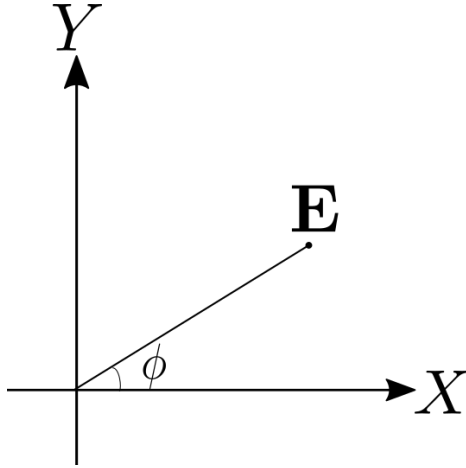


Figure 2.1: Classical representation of electric field \mathbf{E} for monochromatic light in phase space. Here X and Y are quadratures. Both quadratures are perfectly accurate, so the representation is a point.

However, in a quantum mechanical description, there is always noise, or uncertainty, of the light field, which comes from the quantum nature of the light field and cannot be eliminated by any classical means. The Heisenberg uncertainty principle in quantum mechanics states that for a pair of conjugate variables, the product of their uncertainties must be no less than a certain value. Unlike the classical case, the quadratures in quantum mechanics cannot be simultaneously determined with unlimited accuracy. In other words, there are always uncertainties associated with these variables. This is shown in Fig. 2.2, where the shaded area illustrates the uncertainties associated with each of the quadratures. In a quantum mechanical description, the electric field is quantized and quadratures X, Y are replaced with Hermitian operators \hat{X}, \hat{Y} with definitions of

$$\hat{X} = \frac{\hat{a} + \hat{a}^\dagger}{2}, \quad (2.2a)$$

$$\hat{Y} = \frac{\hat{a} - \hat{a}^\dagger}{2i}, \quad (2.2b)$$

where \hat{a}, \hat{a}^\dagger are the photon (bosonic) annihilation and creation operators, respectively.

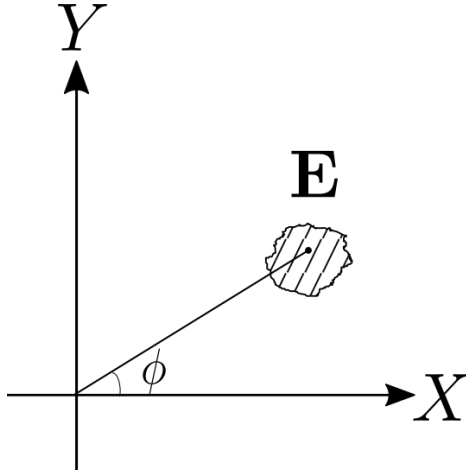


Figure 2.2: Representation of uncertainties of a single-mode electric field \mathbf{E} for monochromatic light in phase space. Here X and Y are quadratures. The shaded area are uncertainties associated with the quadratures.

\hat{X} and \hat{Y} are conjugate variables that are experimentally measurable.

In order to understand the quantum properties of light, consider a single mode of light at frequency ω . After second quantization, any state of this light can be represented as an eigenstate or a superposition of eigenstates of a harmonic oscillator. For a single mode, these eigenstates $|n\rangle$ represent the number of photons n present in the mode with fixed wavevector \mathbf{k} , fixed polarization, and frequency ω in the field. The Hamiltonian operator of the field is

$$\hat{H} = \hbar\omega \left(\hat{a}^\dagger \hat{a} + \frac{1}{2} \right) = \hbar\omega \left(\hat{n} + \frac{1}{2} \right) = \hbar\omega (\hat{X}^2 + \hat{Y}^2), \quad (2.3)$$

where \hat{a}^\dagger and \hat{a} are creation and annihilation operators, $\hat{n} = \hat{a}^\dagger \hat{a}$ is the number operator, \hat{X} and \hat{Y} are quadrature operators, and \hbar is the reduced Planck constant. Therefore, for eigenstate $|n\rangle$, we have

$$\hat{H}|n\rangle = \hbar\omega \left(n + \frac{1}{2} \right) |n\rangle. \quad (2.4)$$

The ground state of the field corresponds to $n = 0$, which is also known as the vacuum

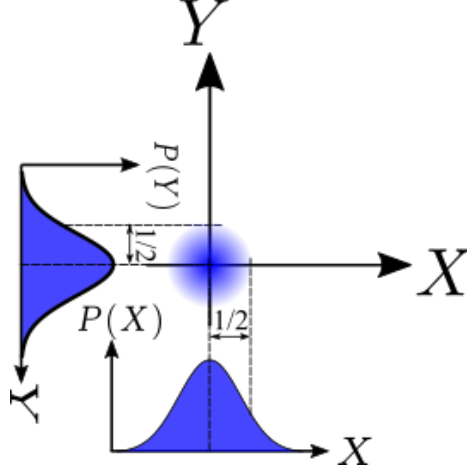


Figure 2.3: Representation of the vacuum state of a single mode of light in phase space. Here X and Y are quadratures. The shaded area represents the uncertainties associated with the quadratures, with $P(X)$ and $P(Y)$ the probability distributions, which follow a Gaussian distribution for the vacuum state.

state $|0\rangle$, with energy $E_0 = \frac{1}{2}\hbar\omega$. In the vacuum state, the mean number of photons $\langle n \rangle$ is zero, however, the fluctuation in the field is non-zero. Quadrature operators \hat{X} and \hat{Y} satisfy the commutation relation [37]

$$[\hat{X}, \hat{Y}] = \frac{i}{2}. \quad (2.5)$$

This leads to a Heisenberg uncertainty relation of the following form

$$\Delta^2 \hat{X} \Delta^2 \hat{Y} \geq \frac{1}{16}, \quad (2.6)$$

where $\Delta^2 \hat{A} = \langle (\hat{A} - \langle \hat{A} \rangle)^2 \rangle$ represents the variance of an operator \hat{A} . The Heisenberg uncertainty implies that even in the vacuum state $|0\rangle$, the variances of \hat{X} and \hat{Y} are non-zero, which means measurements of the quadratures cannot be infinitely precise simultaneously. In the vacuum state, $\langle \hat{X} \rangle = \langle \hat{Y} \rangle = 0$, $\Delta \hat{X} = \Delta \hat{Y} = 1/2$, so the minimum noise limit $\Delta^2 \hat{X} \Delta^2 \hat{Y} = 1/16$ is reached, as shown in Fig. 2.3. This minimum noise limit for the quadratures is known as the shot noise limit (SNL). The probability

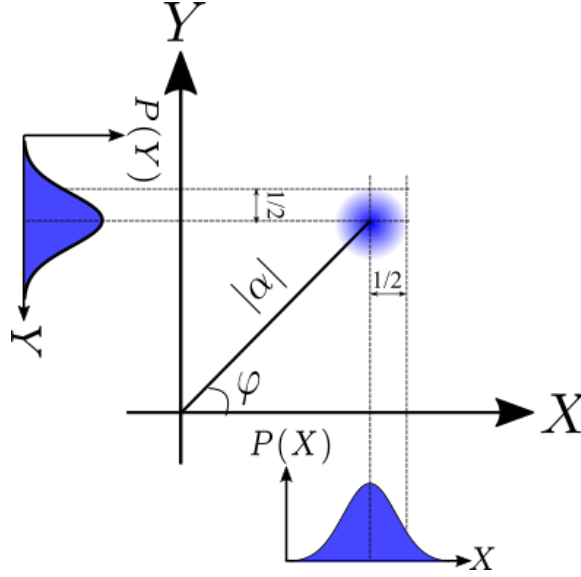


Figure 2.4: Representation of a coherent state of a single-mode of light in phase space. A coherent state is a displaced vacuum state with non-zero mean photon number and the same noise distributions. Here X and Y are quadratures. The shaded area represents the uncertainties associated with the quadratures, with $P(X)$ and $P(Y)$ the probability distributions, which follow Gaussian distributions for a coherent state.

density $P(X)$ and $P(Y)$ for the vacuum state are Gaussian, with mean of 0 and standard deviation of $1/2$.

One can also have a state of light with a non-zero mean photon number while still having quadrature variances of $\Delta^2 \hat{X} = \Delta^2 \hat{Y} = 1/4$ and satisfying the SNL. Such a state is called a coherent state, as shown in Fig. 2.4. The coherent state can be represented as a phasor in phase space with mean magnitude $|\alpha|$ and a surrounding circular area of uncertainty. The probability distribution of the quadratures are Gaussian, with non-zero mean values of $\langle \hat{X} \rangle$ and $\langle \hat{Y} \rangle$, and standard deviations of $\Delta \hat{X} = \Delta \hat{Y} = 1/2$ [37]. The vacuum state is also a coherent state, with $|\alpha| = 0$ so that $\langle \hat{X} \rangle = \langle \hat{Y} \rangle = 0$. Mathematically, a coherent state $|\alpha\rangle$ is the eigenstate of the

annihilation operator \hat{a} , this reads

$$\hat{a}|\alpha\rangle = \alpha|\alpha\rangle. \quad (2.7)$$

Since \hat{a} is not Hermitian, it is, in general, a complex number. A coherent state $|\alpha\rangle$ can be expressed as $|\alpha\rangle = |\alpha|e^{i\varphi}$, where $|\alpha|$ and φ are the amplitude and phase of the coherent state $|\alpha\rangle$.

The vacuum state and the coherent state obey the minimum limit of Heisenberg uncertainty principle Eq. (2.6), and the two quadratures have the same standard deviation, i.e., $\Delta^2\hat{X} = \Delta^2\hat{Y} = 1/4$. The Heisenberg principle sets a lower bound of the product of the variances for the quadratures of a given field, however, it does not fix any constraint on the individual variances. So one of the variances could possibly be squeezed. A quadrature-squeezed state, or a squeezed state, by definition, is a state in which any of the quadrature standard deviation is smaller than the SNL at the expense of the other quadrature standard deviation being larger than the SNL, in such a way that the Heisenberg uncertainty principle is still satisfied. The phase space representation of a squeezed state is shown in Fig. 2.5, where quadrature \hat{Y} is squeezed, with $\Delta^2\hat{Y} < 1/4$, while quadrature \hat{X} is anti-squeezed, such that $\Delta^2\hat{X} > 1/4$.

Mathematically, a squeezed coherent state can be defined by

$$|\alpha, \zeta\rangle = \hat{D}(\alpha)\hat{S}(\zeta)|0\rangle, \quad (2.8)$$

where $|0\rangle$ is the vacuum state, $\hat{D}(\alpha)$ is the displacement operator and $\hat{S}(\zeta)$ is the squeezing operator. These unitary operators are given by

$$\hat{D}(\alpha) = \exp(\alpha\hat{a}^\dagger - \alpha^*\hat{a}), \quad (2.9)$$

and

$$\hat{S}(\zeta) = \exp\left[\frac{1}{2}(\zeta^*\hat{a}^2 - \zeta\hat{a}^{\dagger 2})\right], \quad (2.10)$$

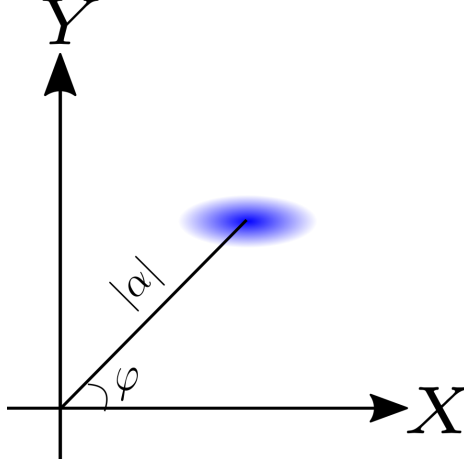


Figure 2.5: Representation of a squeezed state of a single-mode light in phase space. Here X and Y are quadratures. The shaded area represents the uncertainties associated with the quadratures. Here, the uncertainty of Y is squeezed, and the uncertainty of X is anti-squeezed, but they still obey the Heisenberg uncertainty principle.

with \hat{a} , \hat{a}^\dagger the annihilation and creation operators, respectively. ζ is defined as

$$\zeta = se^{i\theta}, \quad (2.11)$$

where s is referred to as the squeezing parameter and θ is known as the squeezing phase. As Fig. 2.6 illustrates, a squeezed coherent state could be generated by applying the squeezing operator $\hat{S}(\zeta)$ and displacement operator $\hat{D}(\alpha)$ on the vacuum state $|0\rangle$.

For a squeezed coherent state $|\alpha, \zeta\rangle$ defined by Eq. (2.8), the variances of the quadratures along the ellipse axes are [39]

$$\langle(\Delta\hat{X}')^2\rangle = \frac{1}{4}e^{-2s}, \quad (2.12a)$$

$$\langle(\Delta\hat{Y}')^2\rangle = \frac{1}{4}e^{2s}, \quad (2.12b)$$

where $\hat{X}' = \hat{X}e^{-i\theta/2}$, $\hat{Y}' = \hat{Y}e^{-i\theta/2}$, are rotated quadratures by angle $\theta/2$ that are along the major and minor axes of the squeezing ellipse.

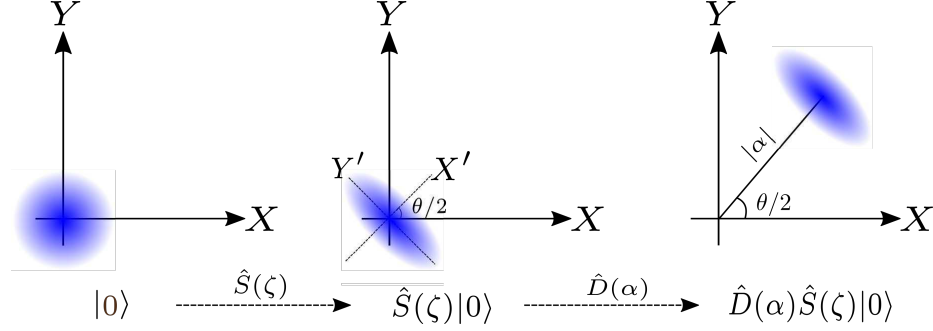


Figure 2.6: A schematic of a squeezed coherent state created by applying the squeezing operator $\hat{S}(\zeta)$ and displacement operator $\hat{D}(\alpha)$ on the vacuum state $|0\rangle$.

2.1.2 Two-Mode Squeezed States

The concept of squeezed states can be extended to multimode fields, such as the two-mode squeezed state (TMSS). As the name suggests, TMSS is a squeezed state of two-mode light fields, in which two distinguishable light fields are quantum correlated. Specifically, we are interested in two-mode relative intensity squeezing, in which two entangled optical fields have correlated amplitude fluctuations. If we have two electric fields with frequencies ω_1 and ω_2 , they can be described as

$$\hat{E}_1(t) = 2E_0[\hat{X}_1\cos(\omega_1 t) + \hat{Y}_1\sin(\omega_1 t)], \quad (2.13a)$$

$$\hat{E}_2(t) = 2E_0[\hat{X}_2\cos(\omega_2 t) + \hat{Y}_2\sin(\omega_2 t)], \quad (2.13b)$$

where \hat{X}_i, \hat{Y}_i ($i = 1, 2$) are quadrature operators of the individual field respectively.

The two-mode quadratures can be generalized as joint quadratures of each field where

$$\hat{X}_+ = \frac{1}{\sqrt{2}}(\hat{X}_1 + \hat{X}_2), \quad (2.14a)$$

$$\hat{X}_- = \frac{1}{\sqrt{2}}(\hat{X}_1 - \hat{X}_2), \quad (2.14b)$$

$$\hat{Y}_+ = \frac{1}{\sqrt{2}}(\hat{Y}_1 + \hat{Y}_2), \quad (2.14c)$$

$$\hat{Y}_- = \frac{1}{\sqrt{2}}(\hat{Y}_1 - \hat{Y}_2). \quad (2.14d)$$

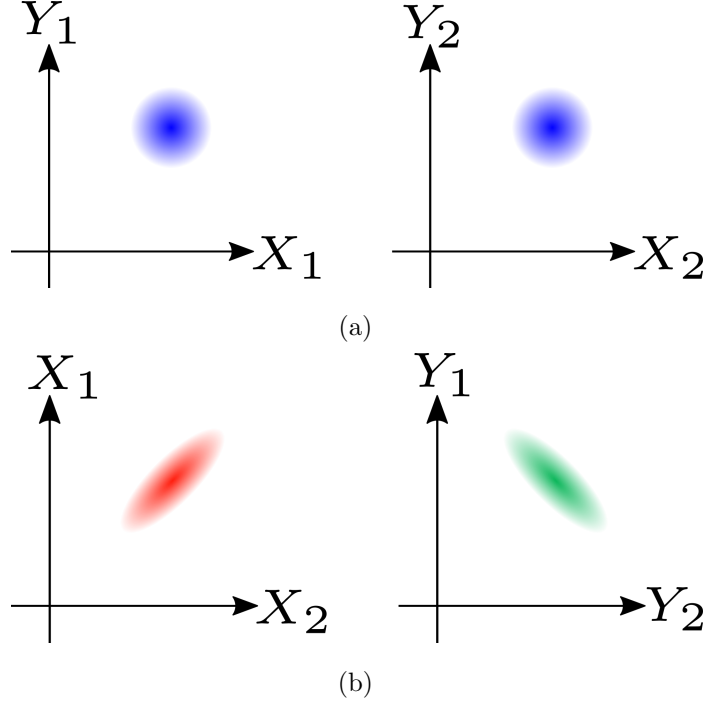


Figure 2.7: (a) Quadrature fluctuations of individual fields \hat{E}_1 and \hat{E}_2 . (b) Joint quadrature fluctuations showing squeezing in \hat{X}_- and \hat{Y}_+ , as well as anti-squeezing in \hat{X}_+ and \hat{Y}_- .

The definitions for the joint quadratures also satisfy the commutation relations,

$$[\hat{X}_\pm, \hat{Y}_\pm] = \frac{i}{2}, \quad (2.15a)$$

$$[\hat{X}_\pm, \hat{Y}_\mp] = 0. \quad (2.15b)$$

Eq. (2.15) implies that the quadratures of a two-mode state share the same properties of a single-mode state, so a two-mode state can also be squeezed. If the intensities of E_1 and E_2 are temporally correlated, and increase in the amplitude of E_1 , i.e., the X_1 quadrature, will correspondingly occur with the same fluctuation in E_2 , i.e., the X_2 quadrature, this will cause a reduction of the variance of two-mode quadrature X_- at the expense of an increase in the variance of quadrature \hat{Y}_- . Such a state is known as a TMSS. As shown in Fig 2.7, the individual quadratures of E_1 and E_2 are

not squeezed, but their joint quadratures of \hat{X}_- , \hat{Y}_+ are squeezed, with \hat{X}_+ and \hat{Y}_- anti-squeezed. Mathematically, a TMSS is defined as

$$|\alpha, \beta; \zeta\rangle = \hat{D}_a(\alpha)\hat{D}_b(\beta)\hat{S}_{ab}(\zeta)|0, 0\rangle, \quad (2.16)$$

where $\hat{D}_a(\alpha)$ and $\hat{D}_b(\beta)$ are displacement operators of field \hat{E}_1 and \hat{E}_2 respectively, similar to the single-mode field, and the squeezing operator $\hat{S}_{ab}(\zeta)$ has the form

$$\hat{S}_{ab}(\zeta) = \exp(\zeta^*\hat{a}\hat{b} - \zeta\hat{a}^\dagger\hat{b}^\dagger), \quad (2.17)$$

where \hat{a}^\dagger (\hat{a}), \hat{b}^\dagger (\hat{b}) are the creation (annihilation) operators of the two modes respectively.

2.2 Nonlinear Response of an Optical Medium

Generation of two-mode squeezed light states requires creating two photons simultaneously, which can be realized through a nonlinear optical process. Methods commonly used in generating squeezed light include four-wave mixing in hot atomic vapors and photon-pair production in crystals.

When the light propagates in a medium, it induces a polarization in the material. The induced polarization P can be expressed as $P(E)$, a function of the electric field strength E . Depending on the relation between P and E , the medium can be classified as a linear or nonlinear optical medium. A linear medium is characterized by a linear relation between P and E , i.e., $P(E) = \epsilon_0\chi E$, where ϵ_0 is the permittivity of free space and χ is the electric susceptibility of the medium. A nonlinear medium, on the other hand, is characterized by a nonlinear relation between P and E [40],

$$P(E) = \epsilon_0\chi(E) = \epsilon_0(\chi^{(1)}E + \chi^{(2)}E^2 + \chi^{(3)}E^3 + \dots), \quad (2.18)$$

where the coefficients $\chi^{(n)}$ are the n-th-order susceptibilities of the medium, and the presence of such a term is generally referred to as an n-th-order nonlinearity.

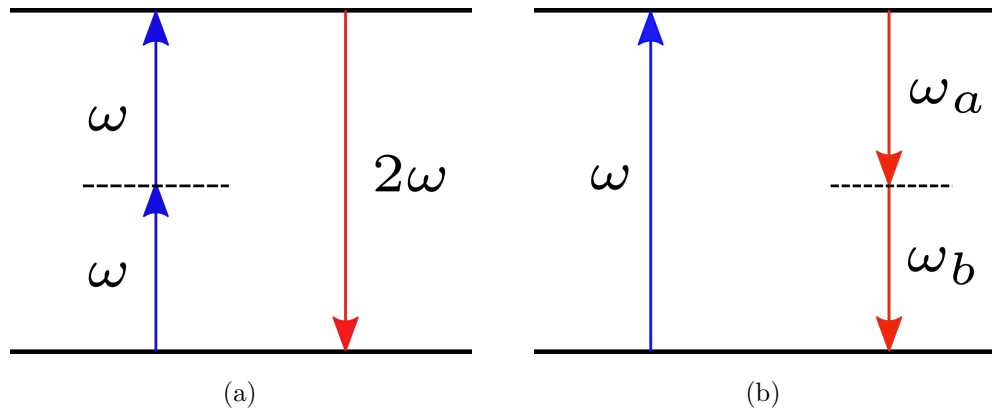


Figure 2.8: (a) Frequency doubling process, in which two photons at frequency ω are absorbed and a single photon at frequency 2ω is generated. (b) Parametric down conversion process, in which one photon at frequency ω is absorbed while two photons at frequencies ω_a and ω_b are emitted, the frequencies satisfy $\omega = \omega_a + \omega_b$.

Examples of the second-order nonlinear process, or $\chi^{(2)}$ processes, are second harmonic generation and parametric down conversion, as shown in Fig. 2.8. Second harmonic generation is also known as frequency doubling. Two photons with the same frequency ω are annihilated simultaneously when interacting with the nonlinear medium and a new photon with frequency ω_2 is generated. Since the photon energy is $E = \hbar\omega$, where \hbar is the reduced Planck constant, the rule of energy conservation yields

$$\omega_2 = \omega + \omega = 2\omega. \quad (2.19)$$

So the new generated photon has a frequency that is doubled compared to the initial photon, which is a direct consequence of the energy conservation during the interaction. At the same time, the momentum conservation gives

$$\mathbf{k}_2 = \mathbf{k} + \mathbf{k} = 2\mathbf{k}. \quad (2.20)$$

The generation of the second harmonic is very useful technically, because it offers the possibility to double the frequencies of a light field. For example, the main laser used

in our experimental setup is a Toptica SHG-Pro diode laser, the SHG system doubles the frequency, which is equal to halving the wavelength λ , from the infrared light of $\lambda \approx 1178$ nm to the yellow light of $\lambda \approx 589$ nm via the second harmonic generation (SHG) process.

Parametric down conversion is the process of absorbing one photon with frequency ω and emitting a pair of photons with frequencies ω_a and ω_b such that $\omega_a + \omega_b = \omega$. Both of the $\chi^{(2)}$ processes involve three fields total. Parametric down conversion is only one of many possible processes to generate photon pairs.

Similar to the case of second-order nonlinear phenomena, as a result of the $\chi^{(3)}$ nonlinear susceptibility, the third-order nonlinear process can involve three photons from the fundamental waves with frequency $\omega_1, \omega_2, \omega_3$ and generate a new photon with frequency ω_4 . If the three annihilated photons have the same frequency ω , the frequency of the newly generated photon is tripled, as shown in Fig. 2.9a, this is called third harmonic generation (THG). The rules of energy and momentum conservation are applied to the involved photons in THG:

$$\omega_4 = \omega_1 + \omega_2 + \omega_3 = 3\omega, \quad (2.21a)$$

$$\mathbf{k}_4 = \mathbf{k}_1 + \mathbf{k}_2 + \mathbf{k}_3 = 3\mathbf{k}. \quad (2.21b)$$

With third-order nonlinear effects it is also possible that two fundamental photons are annihilated during the interaction, and two new photons are generated simultaneously, as shown in Fig. 2.9b. The energy and momentum conservation are also valid for all involved photons:

$$\omega_1 + \omega_2 = \omega_3 + \omega_4, \quad (2.22a)$$

$$\mathbf{k}_1 + \mathbf{k}_2 = \mathbf{k}_3 + \mathbf{k}_4. \quad (2.22b)$$

This third-order nonlinear effect is called four-wave mixing. 4WM is of particular interest for many applications, since the two generated photons are emitted in pairs

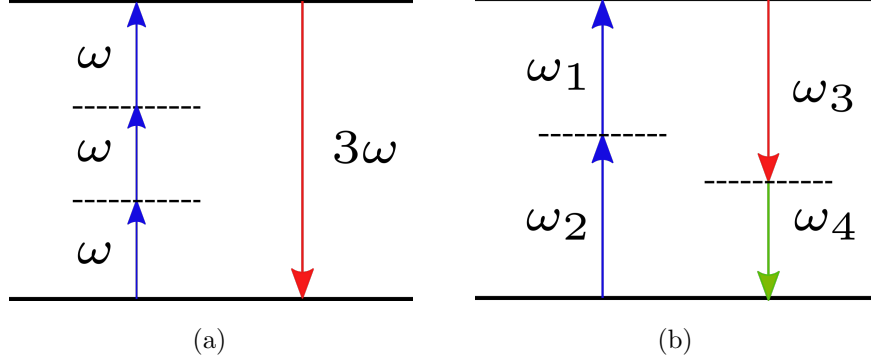


Figure 2.9: (a) Third harmonic generation process, in which three photons at frequency ω are absorbed and a single photon at frequency 3ω is generated. (b) Four-wave mixing process, in which two photons at frequencies ω_1, ω_2 , are absorbed while two new photons at frequencies ω_3 and ω_4 are emitted, the frequencies satisfy $\omega_1 + \omega_2 = \omega_3 + \omega_4$.

and the amplitudes of the two light fields are correlated.

2.3 Four-Wave Mixing in Hot Na Vapors

Four-wave mixing is one of the most effective methods to generate two-mode squeezed light beams [41]. As we know from Sec. 2.2, in order to generate squeezed light via 4WM, the light and medium interaction must produce a nonzero third-order polarization term. Atomic vapors, such as Rb and Na, are $\chi^{(3)}$ media, which means the lowest order nonlinear effect is of the third order. This is because, unlike crystals, atomic vapors have inversion symmetry, such that all the even orders of the susceptibilities, $\chi^{(\text{even})}$, vanish. This is obvious to show, in an inversion symmetric medium,

$$\begin{aligned}
 P(-E) &= \epsilon_0 \sum_1^n \chi^{(n)} (-E)^n \\
 &= -P(E) \\
 &= -\epsilon_0 \sum_1^n \chi^{(n)} (E)^n,
 \end{aligned} \tag{2.23}$$

which is only possible when all the even terms, $\chi^{(\text{even})}$, are zero.

In our experiment, we use a hot sodium (Na) vapor as the nonlinear optical medium. Na, like hydrogen and other alkali metals, has a single outermost valence electron, which makes its energy level structure simple. Therefore, Na is a good candidate for many atomic optical experiments.

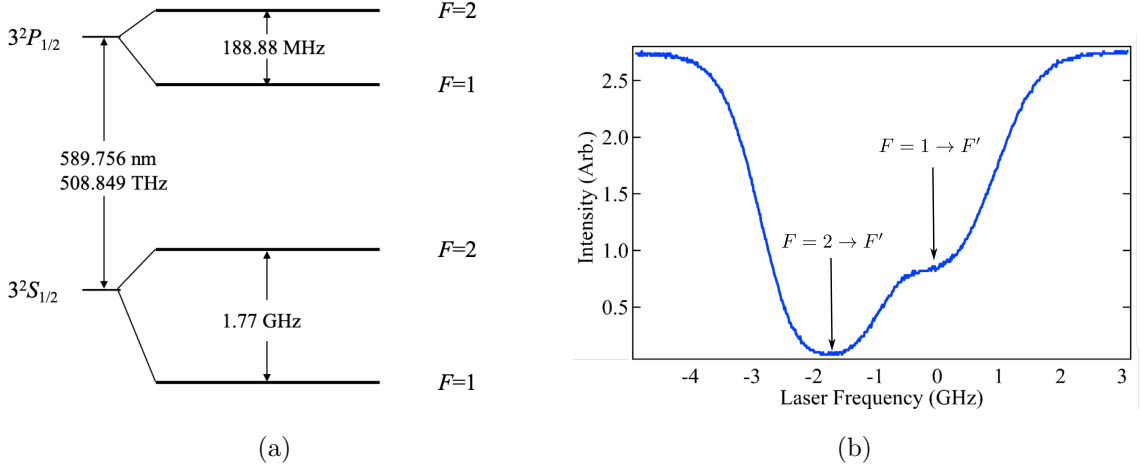


Figure 2.10: (a) ^{23}Na D_1 line, showing the energy spacing between the ground state $3^2S_{1/2}$ and the excited state $3^2P_{1/2}$, and the corresponding hyperfine structures. (b) Measured absorption spectrum of the D_1 line at about 150°C , showing the Doppler broadening and the two resonant absorptions from $F = 1$ and $F = 2$ of the ground state to the excited state, respectively.

The ground state of ^{23}Na is $3^2S_{1/2}$; its first two excited states are the $3^2P_{1/2}$ and $3^2P_{3/2}$ states. The $3^2S_{1/2} \rightarrow 3^2P_{1/2}$ and the $3^2S_{1/2} \rightarrow 3^2P_{3/2}$ transitions, which are also referred to as D_1 line and D_2 line, are the components of the famous fine-structure doublet, which can be observed on a spectrograph as two closely spaced yellow lines at 589 nm.

The D_1 line of ^{23}Na is shown in Fig. 2.10a. Due to hyperfine splitting, the ground and excited states of the ^{23}Na D_1 line separate into two energy levels of $F = 1$ and $F = 2$, which can be modeled as a four-level system. Usually, the hyperfine splitting of the excited state is not considered due to the large Doppler broadening at

high temperatures, and the atom is approximated as a three-level system. Shown in Fig. 2.10b is our measured absorption spectrum from the ground state $3^2S_{1/2}$ to the excited state $3^2P_{1/2}$ in the presence of Doppler broadening, in which the two dips are the resonant absorptions from $F = 1$ and $F = 2$ of the ground state to the excited state, respectively, measured at ~ 150 °C.

2.4 Double-Lambda Configuration

We use a double- Λ configuration on the Na D_1 line to generate two-mode squeezed light in our experiment, as shown in Fig. 2.11. $F = 1$ and $F = 2$ are hyperfine levels of the ground state $3^2S_{1/2}$, and $3^2P_{1/2}$ is the first excited state. In a double- Λ configuration, there are two original input beams, called pumps, and two newly created twin beams, referred to as probe and conjugate. The name “double- Λ ” originates from the fact that the four beams look like two Λ s in the energy level scheme: the lower Λ consists of the probe and one pump, the upper Λ consists of the other pump and the conjugate. In the lower Λ transition, a pump photon at frequency ω_0 is absorbed and causes a transition from $3^2S_{1/2}, F = 2$ to $3^2S_{1/2}, F = 1$ via the intermediate state $3^2P_{1/2}$, emitting a photon, called probe, at frequency ω_p . The upper Λ transition is the reverse process, where a pump photon at frequency ω_0 is absorbed and a new photon called conjugate is emitted at frequency ω_c , resulting in a transition from $3^2S_{1/2}, F = 1$ back to $3^2S_{1/2}, F = 2$ via state $3^2P_{1/2}$. The one-photon detuning, Δ , is defined as the detuning of the pump photon frequency ω_0 from the transition $3^2S_{1/2}, F = 1 \rightarrow 3^2P_{1/2}$. The emitted probe is detuned from the pump by ω_{HF} plus a two-photon detuning δ , that is,

$$\delta = \omega_p - \omega_0 - \omega_{\text{HF}}, \quad (2.24)$$

where ω_{HF} is the hyperfine splitting between $F = 1$ and $F = 2$ ground states, which is about 1.77 GHz for ^{23}Na .

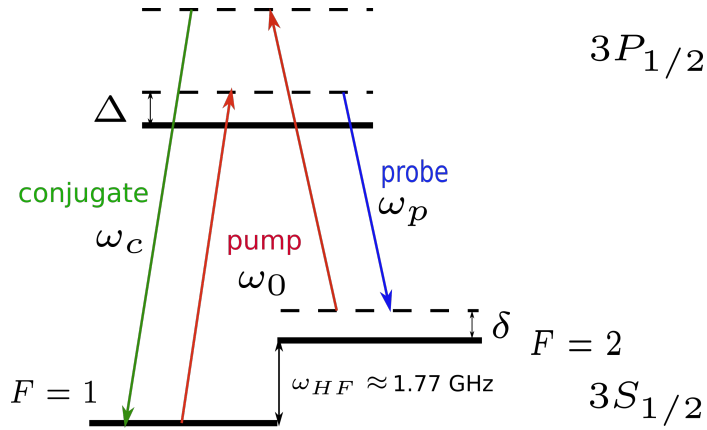


Figure 2.11: Double- Λ scheme on sodium D_1 line. Δ and δ are the one-photon detuning and two-photon detuning, respectively. The hyperfine levels of the excited state are not resolved due to Doppler broadening at high temperatures.

In a four-wave mixing process, an atom gets excited by absorbing two pump photons and then relaxes back to the ground state by emitting a pair of probe and conjugate photons simultaneously. Due to energy conservation, according to Eq. (2.22a), the photon frequencies must satisfy

$$2\omega_0 = \omega_p + \omega_c. \quad (2.25)$$

The probe and conjugate photons are always created in pairs in four-wave mixing, so the numbers of the probe and conjugate photons are highly correlated. The probe and conjugate fields can become quantum entangled. The relative intensity noise of the probe and conjugate beams can be lower than the individual beam noise, and even below the shot noise limit. As a reminder, shot noise is the noise level we would expect from two independent coherent light fields of the same intensities, keeping the total intensity of the two beams unchanged. The shot noise can be measured by splitting a beam with a simple 50/50 beam splitter cube, for example.

In experiments, a hot ^{23}Na vapor is illuminated with a bright pump beam at frequency ω_0 . Pairs of photons are generated at frequencies ω_p and ω_c in the forward

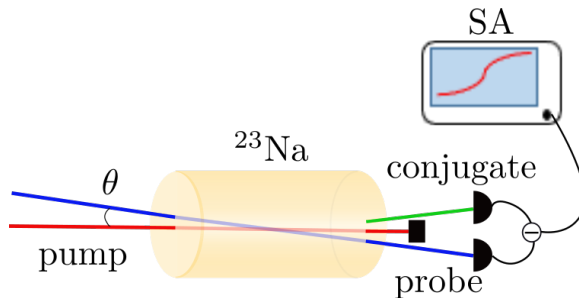


Figure 2.12: Experimental schematic of 4WM beams. A weak seeding probe beam and an intense pump beam propagate and intersect inside a hot ^{23}Na vapor cell with an angle θ . Balanced photodiodes and a spectrum analyzer are used to measure the relative noise between generated probe and conjugate fields. SA: spectrum analyzer.

direction with an angle θ relative to the pump beam. By applying a weak incident probe beam with angle θ relative to the pump beam, as shown in Fig. 2.12, the process can be stimulated. This is also called seeding.

The double- Λ configuration has been shown to be an effective way to generate two-mode squeezed states of light, and high levels of squeezing (-3.5 dB, -8.1 dB, -9 dB) have been observed in Rb [42, 2, 41]. In this thesis, we use a similar double- Λ configuration in ^{23}Na to generate two-mode squeezed states of light and characterize the gain and relative noise. The simulation results and experimental apparatus to perform a 4WM experiment in hot sodium vapors are described in detail in the next chapters.

Chapter 3

Simulation of Four-Wave Mixing in Hot Na Vapors

In this chapter we theoretically investigate the atomic susceptibilities of the sodium vapor medium in response to external light fields. We also discuss the effect of the phase-matching condition and of the effective phase-matching condition. The intensity gain of the probe and conjugate fields is calculated and plotted over various parameter regions. Finally, the limitations of our simulation will be discussed.

3.1 Description of the Susceptibilities

As discussed in Chapter 2, a nonlinear optical process is a result of induced polarization in the medium in the presence of external fields. In order to understand the 4WM process, we first study the polarization response of the atomic medium in the presence of external light fields. The full polarization in a double- Λ system as described in Fig. 2.11 is given by [43, 44]

$$P(\omega_p) = \epsilon_0 \chi_{pp}(\omega_p) \mathbf{E}_p e^{i\mathbf{k}_p \cdot \mathbf{r}} + \epsilon_0 \chi_{pc}(\omega_p) \mathbf{E}_c^* e^{i(2\mathbf{k}_0 - \mathbf{k}_c) \cdot \mathbf{r}}, \quad (3.1a)$$

$$P(\omega_c) = \epsilon_0 \chi_{cc}(\omega_c) \mathbf{E}_c e^{i\mathbf{k}_c \cdot \mathbf{r}} + \epsilon_0 \chi_{cp}(\omega_c) \mathbf{E}_p^* e^{i(2\mathbf{k}_0 - \mathbf{k}_p) \cdot \mathbf{r}}, \quad (3.1b)$$

where $P(\omega_p)$, $P(\omega_c)$ are induced polarizations due to the presence of the probe and conjugate field, respectively. χ_{ij} ($i, j = p, c$) is the susceptibility of the atomic medium, which characterizes the response of the atomic system for a given field. The direct susceptibilities χ_{pp} and χ_{cc} are the effective linear susceptibilities for the probe and conjugate fields, respectively. The two cross terms χ_{pc} , $\chi_{cp} = \chi_{pc}^*$, describe the cross-coupling susceptibilities, which are responsible for the 4WM process. The susceptibilities are derived from the master equation for the density matrix describing

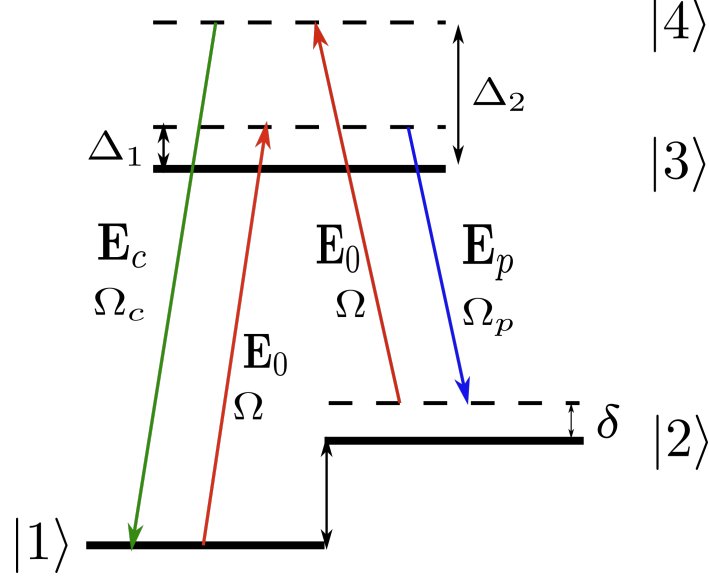


Figure 3.1: Energy level diagram of ^{23}Na D_1 line, showing the double- Λ configuration with a single pump beam field \mathbf{E}_0 and probe/conjugate field $\mathbf{E}_p/\mathbf{E}_c$, respectively. Ω , Ω_p , Ω_c are the Rabi frequencies of the couplings via pump, probe, and conjugate field, respectively.

the double- Λ system shown in Fig. 3.1. They can be expressed by [44]

$$\chi_{pp} = \frac{iN|d_{23}|^2\xi_{41}^*}{\epsilon_0\hbar D^*} \left[\frac{\xi_{21}^*}{\xi_{42}^*} \sigma_{22,44} + \frac{\xi_{43}^*}{\xi_{31}^*} \sigma_{11,33} - \left(\frac{\xi_{21}^* + \xi_{43}^*}{\xi_{41}^*} + \frac{\xi_{21}^*\xi_{43}^*}{|\Omega|^2/4} \right) \sigma_{22,33} \right], \quad (3.2a)$$

$$\chi_{cc} = \frac{iN|d_{14}|^2\xi_{32}^*}{\epsilon_0\hbar D} \left[\frac{\xi_{43}}{\xi_{42}^*} \sigma_{22,44} + \frac{\xi_{21}}{\xi_{31}^*} \sigma_{11,33} - \left(\frac{\xi_{21} + \xi_{43}}{\xi_{32}^*} + \frac{\xi_{21}\xi_{43}}{|\Omega|^2/4} \right) \sigma_{11,44} \right], \quad (3.2b)$$

$$\chi_{pc} = \frac{iNd_{14}d_{23}\xi_{41}^*\Omega^2}{\epsilon_0\hbar D^*|\Omega|^2} \left[\frac{\xi_{21}^*}{\xi_{31}^*} \sigma_{11,33} + \frac{\xi_{43}^*}{\xi_{42}^*} \sigma_{22,44} + \left(\frac{\xi_{21}^* + \xi_{43}^*}{\xi_{41}^*} \right) \sigma_{11,44} \right], \quad (3.2c)$$

$$\chi_{cp} = \frac{iNd_{14}d_{23}\xi_{32}^*\Omega^2}{\epsilon_0\hbar D|\Omega|^2} \left[\frac{\xi_{43}}{\xi_{31}^*} \sigma_{11,33} + \frac{\xi_{21}}{\xi_{42}^*} \sigma_{22,44} + \left(\frac{\xi_{21} + \xi_{43}}{\xi_{32}^*} \right) \sigma_{22,33} \right], \quad (3.2d)$$

where N is the atomic number density of the medium, d_{ij} is the dipole moment corresponding to the transition from state $|i\rangle$ to state $|j\rangle$. D is defined as

$$D = (\xi_{43} + \xi_{21})(\xi_{32}^* + \xi_{41}) + \frac{\xi_{32}^*\xi_{41}\xi_{43}\xi_{21}}{|\Omega|^2/4}. \quad (3.3)$$

$\sigma_{ii,jj}$ are population differences, with σ_{ij} the density matrix element between state $|i\rangle$ and state $|j\rangle$,

$$\sigma_{11,33} = \sigma_{11} - \sigma_{33} = \frac{|\xi_{31}|^2}{|\Omega|^2 + |\xi_{31}|^2 + |\xi_{42}|^2}, \quad (3.4a)$$

$$\sigma_{11,44} = \sigma_{11} - \sigma_{44} = \frac{|\xi_{31}|^2}{|\Omega|^2 + |\xi_{31}|^2 + |\xi_{42}|^2}, \quad (3.4b)$$

$$\sigma_{22,33} = \sigma_{22} - \sigma_{33} = \frac{|\xi_{42}|^2}{|\Omega|^2 + |\xi_{31}|^2 + |\xi_{42}|^2}, \quad (3.4c)$$

$$\sigma_{22,44} = \sigma_{22} - \sigma_{44} = \frac{|\xi_{42}|^2}{|\Omega|^2 + |\xi_{31}|^2 + |\xi_{42}|^2}. \quad (3.4d)$$

ξ_{ij} is the complex decay rate that relates to the field detunings, the natural decay rate γ of the excited states $|3\rangle$, $|4\rangle$, and the ground state decoherence rate γ_c ,

$$\xi_{43} = i(\Delta_2 - \Delta_1) - \gamma, \quad (3.5a)$$

$$\xi_{42} = i(\Delta_2 - \delta) - \frac{\gamma}{2}, \quad (3.5b)$$

$$\xi_{41} = i\Delta_2 - \frac{\gamma}{2}, \quad (3.5c)$$

$$\xi_{32} = i(\Delta_1 - \delta) - \frac{\gamma}{2}, \quad (3.5d)$$

$$\xi_{31} = i\Delta_1 - \frac{\gamma}{2}, \quad (3.5e)$$

$$\xi_{21} = i\delta - \gamma_c. \quad (3.5f)$$

The susceptibilities describe the total response of the medium to both the probe and conjugate fields. Experimentally, they can be adjusted by changing the frequencies of probe/conjugate fields, the atomic density, or the pump intensity.

In order to investigate the susceptibilities in the presence of light fields, we plot the four susceptibility components using expressions Eq. (3.2)–(3.5). The following parameters are optimized based on experimental conditions. The atomic number density N is set to $N = 1.6 \times 10^{17} \text{ m}^{-3}$, which is calculated from the vapor pressure taken from Ref. [45], assuming the sodium vapor cell is heated to about 150 °C. The dipole transitions d_{ij} are all set to be $d = 1.22 \times 10^{-29} \text{ C} \cdot \text{m}$, taken from the effective

far-detuned dipole moment for π -polarized light of the D_1 line from Ref. [45]. We assume the pump light has a power of 700 mW with beam waist 500 μm , which leads to an average intensity of 178 W/cm^2 . The pump field Rabi frequency Ω is then evaluated to be $\Omega = 69\gamma$ for a mean electric dipole $d = 1.22 \times 10^{-29} \text{ C} \cdot \text{m}$.

Fig. 3.2 displays χ as a function of two-photon detuning δ ranging from $\delta = -20\gamma$ to $\delta = 20\gamma$. The primary feature of the plots is that the two-photon resonance sits not at $\delta = 0$, but is shifted to $\delta \approx -8\gamma$ due to the light shift induced by the strong pump field. We also see that the imaginary part of χ_{pp} ($\text{Im}(\chi_{pp})$), which is responsible for the absorption of the probe field, is maximum at the two-photon resonance, where the 4WM cross-coupling (χ_{pc}) also reaches a maximum. Therefore it is not an ideal place to observe 4WM due to the large loss of the probe field, even in the presence of a strong 4WM cross-coupling. However, the absorption of the probe ($\text{Im}(\chi_{pp})$) decays faster than the 4WM cross-coupling ($|\chi_{pc}|$) on the side of resonance, leaving a region of δ on each side of the resonance where the competition between $\text{Im}(\chi_{pp})$ and $|\chi_{pc}|$ can result in a net gain for the probe, which is required for the observation of quantum squeezing. The one-photon resonance of the probe, visible when the calculation of χ_{pp} is extended to large δ range, lies at $\delta \approx 100\gamma$, due to the shifted one-photon detuning $\Delta_1 = 80\gamma$, as shown in Fig. 3.3. It should be noted that the amplitude of χ_{cc} is lower compared to χ_{pp} , indicating the off-resonant nature of the conjugate field. A small negative $\text{Im}(\chi_{cc})$ corresponds to a negative absorption, showing an amplification effect for the conjugate field. This is due to the fact that the effective linear terms are actually “self terms” that are nonlinear in the pump, so they can cause effects like Raman gain.

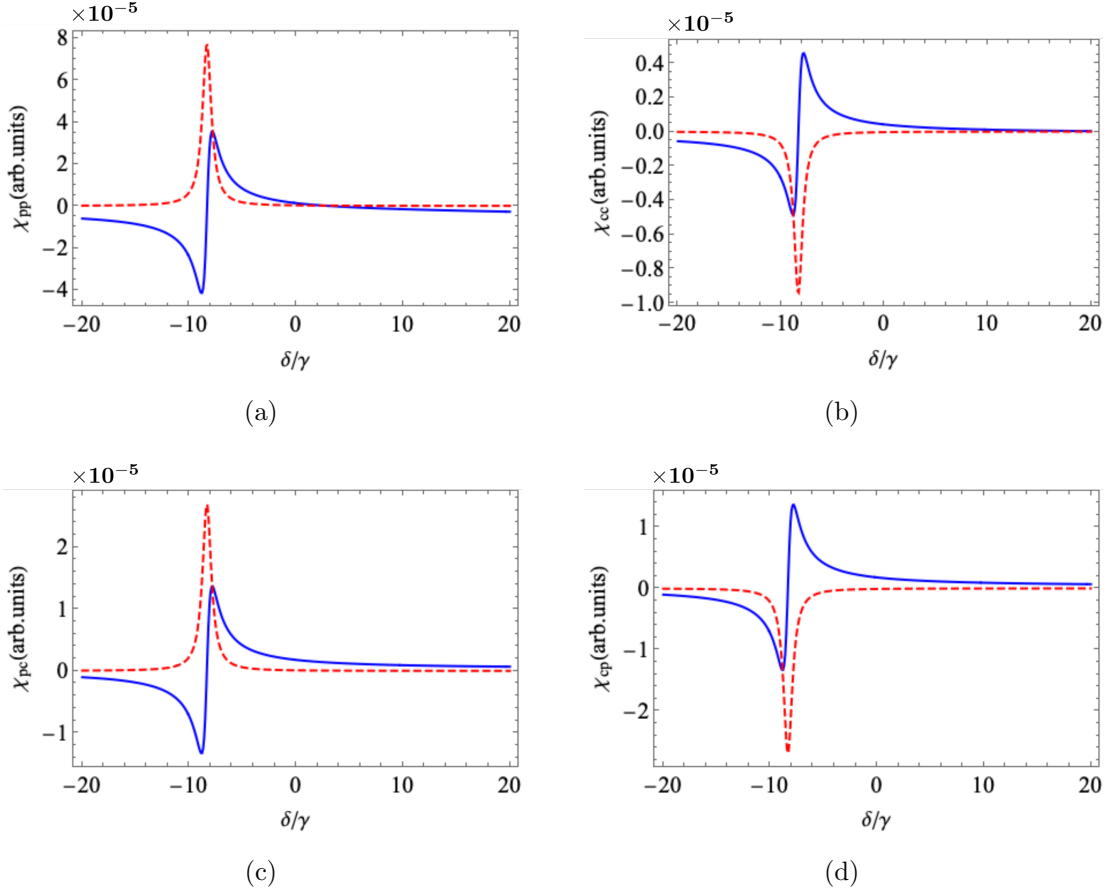


Figure 3.2: Direct χ_{pp} , χ_{cc} (a, b) and cross χ_{pc} , χ_{cp} (c, d) susceptibilities for the probe and conjugate fields as a function of the two-photon detuning δ , in units of the excited state decay rate $\gamma = 2\pi \times 9.79$ MHz. The blue solid lines are the real parts, and the red dashed lines are the imaginary parts. The one-photon detuning is $\Delta_1 = 80\gamma$, and the ground state decoherence rate is set to $\gamma_c = 0.5\gamma$.

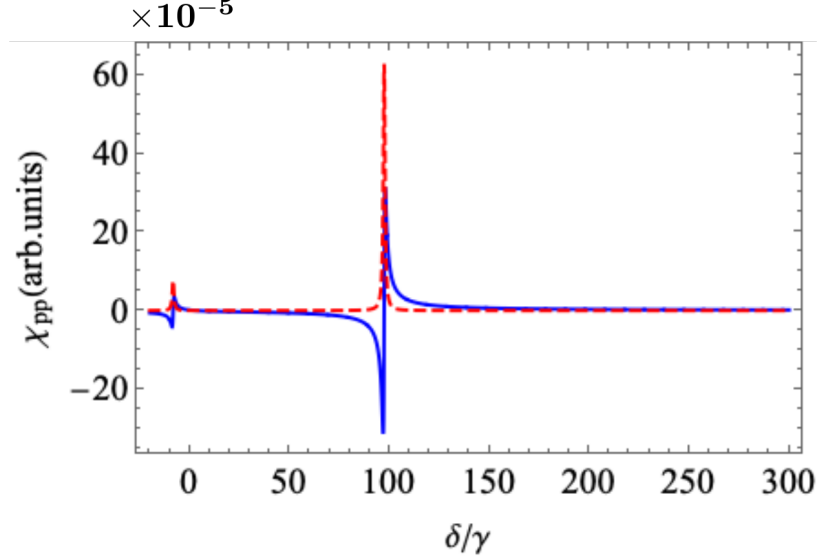


Figure 3.3: Direct susceptibility χ_{pp} as a function of δ over a larger range of detunings. The large one-photon resonance appears at $\delta \approx 100\gamma$.

3.2 Phase-Matching Condition

The propagation of the slowly-varying amplitudes of the probe and conjugate fields inside the atomic medium can be expressed in terms of the polarizations as

$$\frac{\partial}{\partial z} \mathbf{E}_p = \frac{ik_p}{2\epsilon_0} P(\omega_p) e^{-i\mathbf{k}_p \cdot \mathbf{r}}, \quad (3.6a)$$

$$\frac{\partial}{\partial z} \mathbf{E}_c = \frac{ik_c}{2\epsilon_0} P(\omega_c) e^{-i\mathbf{k}_c \cdot \mathbf{r}}. \quad (3.6b)$$

Considering nearly co-propagating beams along the z axis, these field equations in the co-moving frame are written as [44]

$$\frac{\partial}{\partial z} \mathbf{E}_p = \frac{ik_p}{2} \chi_{pp}(\omega_p) \mathbf{E}_p + \frac{ik_p}{2} \chi_{pc}(\omega_p) e^{i\Delta k_z z} \mathbf{E}_c^*, \quad (3.7a)$$

$$\frac{\partial}{\partial z} \mathbf{E}_c = \frac{ik_c}{2} \chi_{cc}(\omega_c) \mathbf{E}_c + \frac{ik_c}{2} \chi_{cp}(\omega_c) e^{i\Delta k_z z} \mathbf{E}_p^*, \quad (3.7b)$$

where Δk_z is the projection of the phase mismatch $\Delta \mathbf{k} = 2\mathbf{k}_0 - \mathbf{k}_p - \mathbf{k}_c$ on the z axis. In order to achieve efficient 4WM coupling, the phase-matching condition has to be

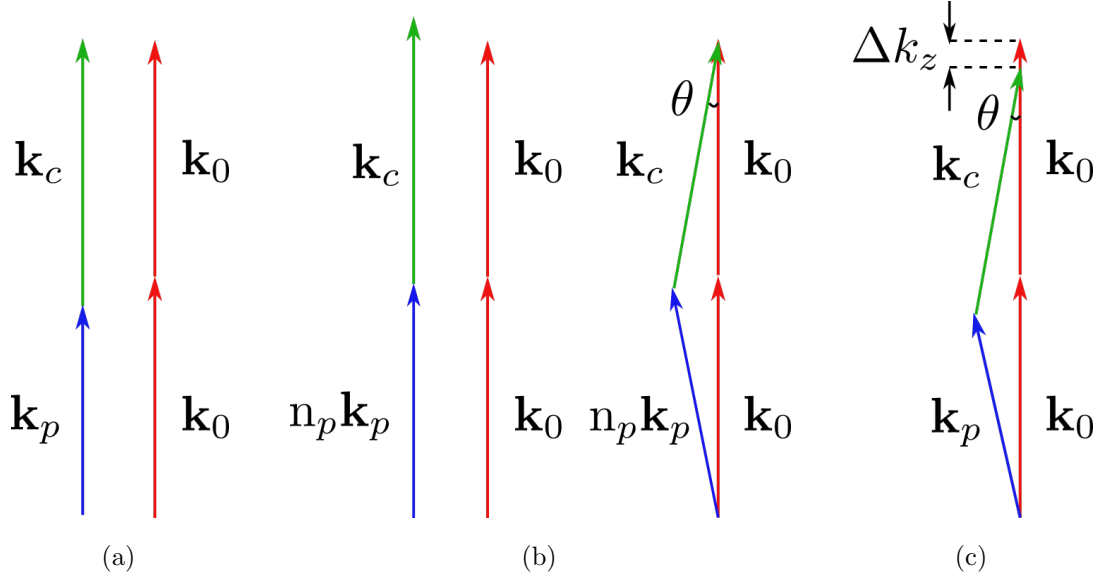


Figure 3.4: Illustration of the geometric phase matching condition. (a) In free space the matching condition is fulfilled ($\Delta k_z = 0$) when all beams are co-propagating. The wave vector sum of the probe and conjugate is equal to the two wave vectors of the pump. (b) The refractive index of the medium, n_p , changes the effective length of the probe wave vector, which results in a phase mismatch. By introducing an angle θ between the probe and the pump beam, the effective phase-matching condition is fulfilled. (c) $\Delta k_z > 0$ when effective phase-matching condition is fulfilled with $n_p > 1$.

fulfilled

$$\Delta \mathbf{k} = 2\mathbf{k}_0 - \mathbf{k}_p - \mathbf{k}_c = 0. \quad (3.8)$$

Eq. (3.7) shows the probe and conjugate fields depend not only on susceptibilities, but also phase mismatch Δk_z . In free space, the phase-matching condition in Eq. (3.8) leads to $\Delta k_z = 0$, which is satisfied when the beams are exactly co-propagating, as shown in Fig. 3.4a. However, this holds only for the case of free space. In a real experimental environment, the refractive index n induced by the 4WM process should

be considered. This leads to the effective phase-matching condition [44]:

$$\Delta \mathbf{k} = 2\mathbf{k}_0 - n_p \mathbf{k}_p - \mathbf{k}_c = 0, \quad (3.9)$$

where $n_p = \sqrt{1 + \text{Re}(\chi_{pp})}$.

As shown in Fig. 3.2, when δ is around resonance ($\delta \approx 0$), $\text{Re}(\chi_{pp}) \approx 0$, so $n_p \approx 1$ and free space configuration can approximately fulfill the phase-matching condition. However, as δ is shifted away from the resonance, $\text{Re}(\chi_{pp})$ increases and $n_p > 1$, which changes the probe wave vector and results in a phase mismatch. In order to correct this, an angle θ is introduced between the probe/conjugate and the pump beam so that the effective phase-matching condition Eq. (3.9) is fulfilled, as seen in Fig. 3.4b. As Fig. 3.4c shows, in this configuration, Δk_z is no longer 0. Δk_z can be expressed as

$$\Delta k_z = 2k_0 - n_p k_p \cos \theta - k_c \cos \theta. \quad (3.10)$$

Experimentally, Δk_z can be adjusted by changing the input angle between the input probe seeding field and the pump field.

3.3 Four-Wave Mixing Gain Calculation

From the previous sections, we note that the two-photon detuning δ and the phase mismatch Δk_z play important roles in the 4WM process, as δ affects the 4WM coupling strength and absorption loss, and Δk_z represents phase matching. In order to further investigate the effects of these parameters, we calculate the 4WM gain for the probe/conjugate fields by adjusting the various parameters. The solutions to the field propagation equations Eq. (3.7), with a seeding probe field \mathbf{E}_s and no input conjugate field, are given by [43]

$$\mathbf{E}_p(L) = \mathbf{E}_s e^{\delta a L} \left[\cosh(\xi L) + \frac{a}{\xi} \sinh(\xi L) \right], \quad (3.11a)$$

$$\mathbf{E}_c^*(L) = \mathbf{E}_s e^{\delta a L} \frac{a_{cp}}{\xi} \sinh(\xi L), \quad (3.11b)$$

where L is the medium length that the fields travel through, and

$$\xi = \sqrt{a^2 - a_{pc}a_{cp}}, \quad (3.12a)$$

$$\delta a = \frac{a_{pp} - a_{cc} + i\Delta k_z}{2}, \quad (3.12b)$$

$$a = \frac{a_{pp} + a_{cc} - i\Delta k_z}{2}, \quad (3.12c)$$

$$a_{pi} = \frac{ik_p\chi_{pi}}{2}, \quad (3.12d)$$

$$a_{ci} = \frac{ik_c\chi_{ci}^*}{2}. \quad (3.12e)$$

We define the gains of the probe and conjugate field intensities as the ratio between the output power and input power:

$$G_p = \frac{|E_p(L)|^2}{|E_s|^2}, \quad (3.13a)$$

$$G_c = \frac{|E_c(L)|^2}{|E_s|^2}. \quad (3.13b)$$

We first explore the dependencies of the probe and conjugate gain on the two-photon detuning δ and the input angle θ between the probe seeding beam and the pump beam. According to Eq. (3.10), changing input angle θ is equal to a change in Δk_z . Fig. 3.5 shows the corresponding gain against δ and input angle θ for the probe and the conjugate fields. Both of the gain curves are asymptotical as they approach the two-photon detuning resonance at $\delta \approx -8\gamma$, due to the phase-matching condition. When the input angle θ increases, i.e., Δk_z increases, a larger δ is required to maximize the gain. It is also shown in the figure that there is a large discrepancy between the behavior of the probe and conjugate. The maximum gain value of the conjugate is several times larger than the probe, due to the large absorption loss of the probe field. Moreover, the maximum gain for the probe and conjugate are located at different parameter regions for δ and θ , which makes it difficult to optimize the gain for the probe and conjugate simultaneously. The discrepancy between the probe and conjugate gain would reduce the possibility of observing quantum squeezing, because

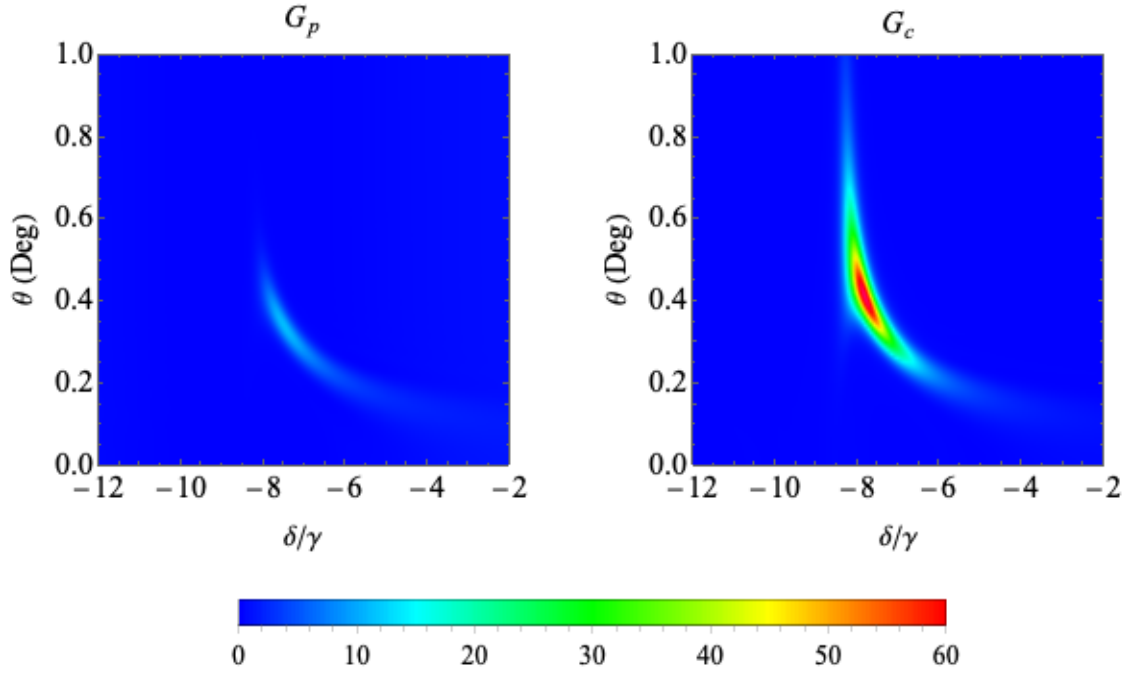
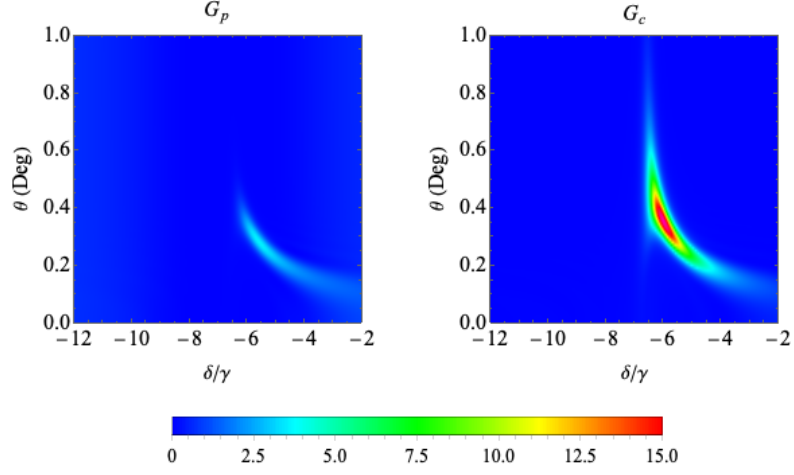


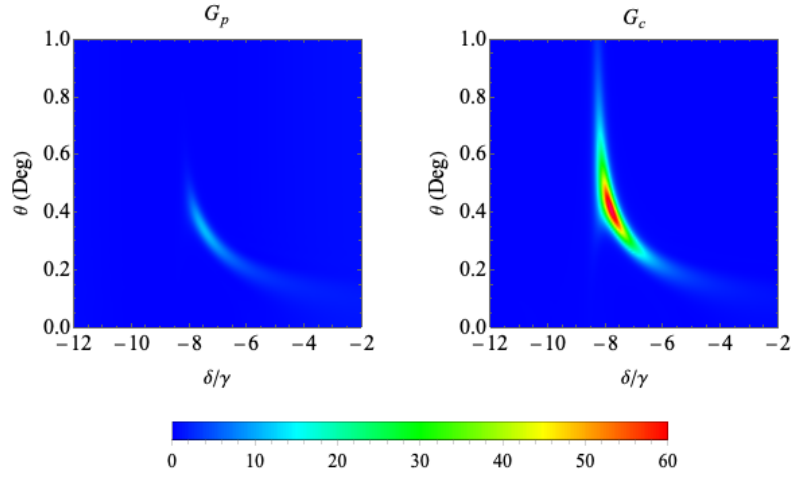
Figure 3.5: Simulated gain behavior of probe (G_p) and conjugate (G_c) over a range of δ and θ . Here $\Omega = 69\gamma$, $\Delta_1 = 80\gamma$.

for amplitude correlations the field amplitude of each beam should be similar.

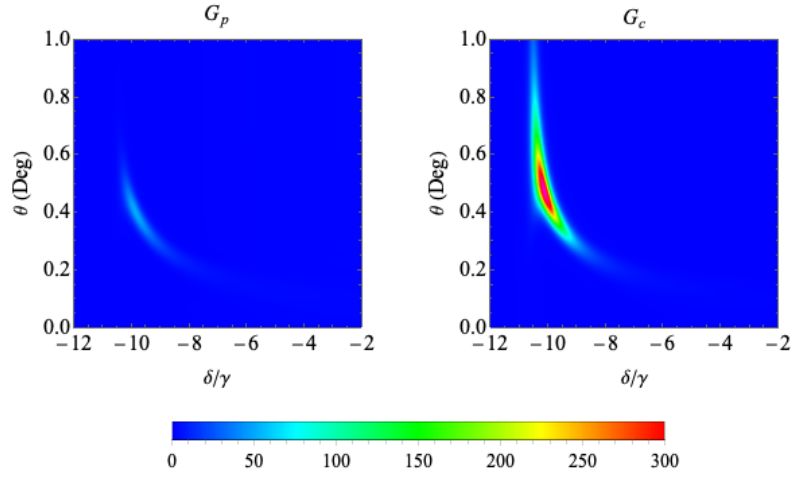
The Rabi frequency Ω for the pump, i.e., the intensity of the pump field, also affects the gain level and the two-photon resonance, as well as the optimized input angle θ . Fig. 3.6 shows the probe and conjugate gain for different pump Rabi frequencies Ω , all other parameters being the same. We find that a higher Ω increases the overall gain levels. Moreover, it shifts the δ resonance point further to the negative side, and also increases the input angle θ required to achieve the maximum gain.



(a) $\Omega = 60\gamma$



(b) $\Omega = 69\gamma$



(c) $\Omega = 80\gamma$

Figure 3.6: Calculated gain of the probe and conjugate beams as functions of two-photon detuning δ and probe-pump angle θ for different pump Rabi frequencies. (a) $\Omega = 60\gamma$, (b) $\Omega = 69\gamma$, (c) $\Omega = 80\gamma$.

3.4 Summary

We solved the coupled differential equations under the approximation of slowly-varying amplitudes and nearly co-propagating fields to calculate the gain of the probe and conjugate fields. The results predict significant gain, especially for the conjugate, when the experimental parameters are adjusted appropriately.

However, a few limitations have to be noted when evaluating the simulation results. First, the parameter region where large gain of the probe and conjugate is achieved does not necessarily indicate a large squeezing of the relative noise between the probe and conjugate fields, due to the enormous discrepancy between the probe and conjugate gain. In fact, maximum gain means high efficiency of the 4WM process, but it is not ideal for the squeezing measurement because of the highly imbalanced twin beams. Second, the model used for the calculation does not take the Doppler effect into account. The frequencies of the probe and pump fields, seen by the moving atoms, are shifted as

$$\omega'_c = \omega_c \left(1 + \frac{v}{c}\right), \quad (3.14a)$$

$$\omega'_0 = \omega_0 \left(1 + \frac{v}{c}\right), \quad (3.14b)$$

where ω_0 and ω_c , are the frequencies of the pump and probe fields, respectively. Even though the probe and pump beams are nearly co-propagating, since $\omega_0 \neq \omega_c$, the Doppler effect does not completely cancel out and there is still a residual Doppler shift which causes inhomogeneous broadening for the fields due to the motion of the atoms in the vapor cell. Besides, the large line broadening resulting from the Doppler effect at high temperatures causes a large absorption, considering the hyperfine splitting of ^{23}Na ground state is relatively small (≈ 1.77 GHz). In the future, we plan to include the Doppler effect by integrating atom velocities, which is more computationally intensive. The third limitation of the calculation is that it assumes a constant pump

Rabi frequency Ω , and constant index of refraction n_p through the entire process. In reality, the pump beam is Gaussian distributed and the change of intensity along the spatial profile results in a position-dependent Rabi frequency and phase matching condition, which causes a reduction on the gain level at the output.

Our simulation results are promising and can be used as a guide to indicate that 4WM with gain larger than one could be obtained in our setup in hot sodium vapors. However, in the experiments, it is still necessary to adjust all the parameters empirically, because several experimental effects such as self-focusing and others are not captured in the simulation model.

A future direction to improve our calculation is to incorporate the Doppler effect, as well as compare the calculation results with the experimental results to verify the methods. The simulation results presented here serve as guide for our experimental explorations. In the next chapter, I describe the setup of the experiments and the optimization of the 4WM gain according to the simulations presented here.

Chapter 4

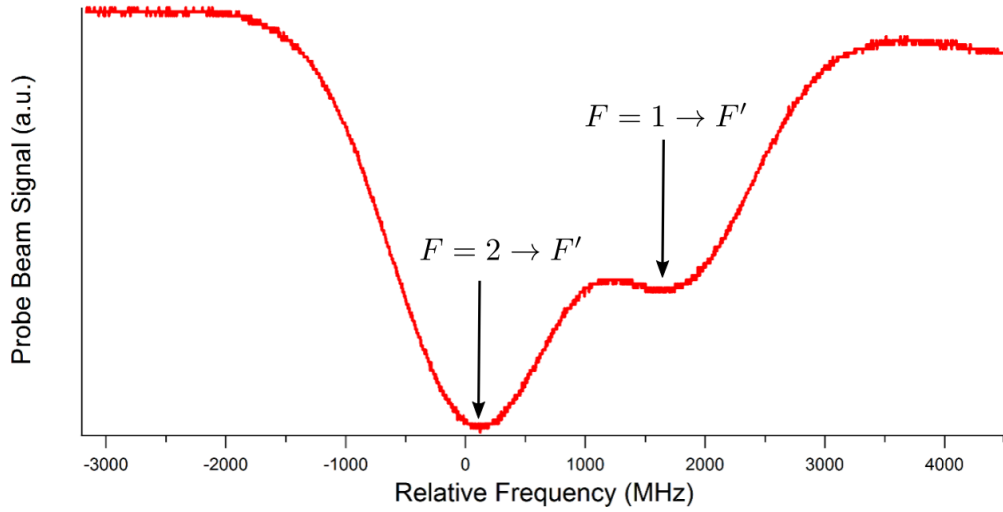
Experimental Setup for Four-Wave Mixing in Hot Na Vapors

In this chapter, we describe the experimental setup used to perform the 4WM experiments. Sec. 4.1 shows the laser system and laser frequency stabilization using saturated absorption spectroscopy, Sec. 4.2 gives a detailed description of our optics setup for 4WM, Sec. 4.3 introduces our home-built cell oven, and Sec. 4.4 describes the detection.

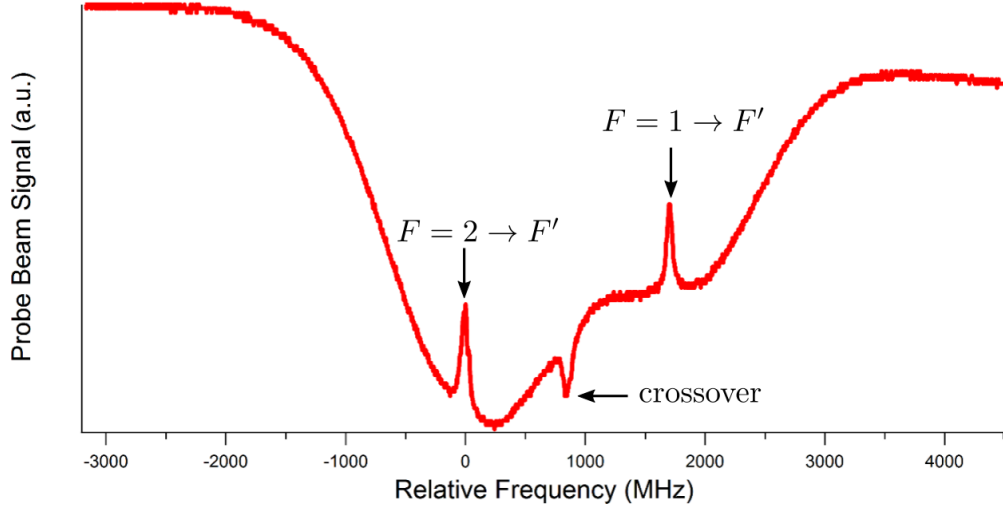
4.1 Laser System

The pump and probe beams used in 4WM transitions are derived from a commercial solid-state laser system that generates 1 Watt of 589 nm laser light (Toptica TA-SHG Pro). The second harmonic generation (SHG) module inside the laser means that the infrared light from a laser diode in external cavity configuration (ECDL) is amplified by a tapered amplifier and the frequency is doubled and converted into visible light in a bow-tie cavity. The system is capable of emitting a continuous light beam at a power of approximately 1 Watt over a tunable wavelength range of 589 ± 3 nm with instantaneous linewidth on the order of a few kHz. The laser frequency is monitored on an external wavelength meter, HighFinesse WS7, using a diagnostic low power output of the IR diode light before doubling. The wavelength meter delivers excellent absolute accuracy of 30 MHz with a measurement speed of up to 500 Hz for pulsed and continuous lasers, which allows us to monitor the laser frequency. To keep the laser frequency precise and stable without drifting, which is fundamental in our experiments, we actively lock the laser frequency through saturated absorption spectroscopy.

Saturated absorption spectroscopy is a frequently-used technique for precisely



(a)



(b)

Figure 4.1: (a) Absorption profile for laser spectroscopy of Na D_2 line when pump beam is off. The two strong absorption regions are Doppler-broadened transitions between the $3^2S_{1/2}, F = 2, 3^2S_{1/2}, F = 1$ ground state and the $3^2S_{1/2}, F' = 1, 2, 3$ excited states respectively. (b) Absorption profile for saturated absorption spectroscopy of Na. It resembles the profile from regular laser spectroscopy but with added Lamb dips.

determining the atomic transition frequency while counteracting the Doppler broadening from a hot atomic vapor. In regular laser spectroscopy, laser light propagates

through a hot atomic vapor, and the absorption profile is Doppler-broadened by a few hundred MHz to GHz, depending on the vapor temperature and atomic mass. Shown in Fig. 4.1a is our measured Doppler-broadened absorption profile of our Na vapor. The two dips are the transitions from $F = 1$ and $F = 2$ hyperfine ground states to the excited state of the D_2 line. In saturated absorption spectroscopy, a strong second laser light, called pump beam, with the same frequency as the weak probe beam, counter-propagates through the atomic vapor cell. If the laser is on resonance, both beams interact with atoms that have zero longitudinal velocity, and the probe absorption is significantly less because the pump beam is strong enough to saturate the transition. Fig. 4.1b shows the two peaks in the absorption profile measured in our saturated spectroscopy setup when the strong pump beam is turned on, known as Lamb dips. The two peaks are associated with two transitions respectively, and the center dip in between is the result of crossover resonances at frequencies directly between two peaks. A crossover resonance appears in the spectrum whenever the Doppler shift causes a velocity class with non-zero longitudinal velocity to be resonant on one transition with the Doppler shifted probe beam and on a different transition with the Doppler shifted pump beam. In our saturated absorption spectroscopy design, a lock-in amplifier (5207 Lock-in Amplifier from Princeton Applied Research) is used to generate an error signal that is proportional to the laser detuning from the desired frequency to create the feedback loop for locking the laser. The lock-in amplifier first creates a signal proportional to the derivative of the probe beam absorption signal, which will have zero crossings for each of the well-defined Lamb dips in the absorption profile, as shown in Fig. 4.2. This signal is then fed into a home-built analog PID controller to create the final error signal that is fed back into the laser control which adjusts the frequency, and a feedback loop is created.

Fig. 4.3 shows the experimental setup of our saturated absorption spectroscopy. A

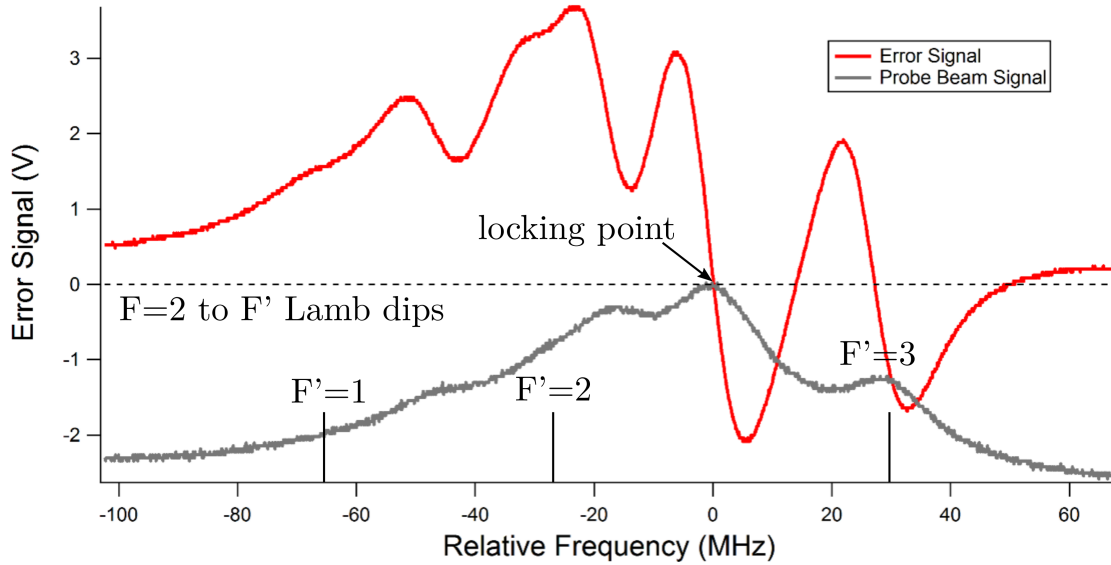


Figure 4.2: Bottom trace (grey): closer view of the probe beam signal for transitions involving the $F = 2$ ground state. Top trace (red): the output error signal from the lock-in amplifier after FM modulation of the pump beam with an AOM. We choose the first positive to negative zero crossing point (at 0 MHz relative frequency in this figure), which is the maximum point of the probe signal, to be our locking point.

portion of the beam from our main laser is split into the probe and pump beams which propagate through a Na vapor cell in opposite directions. The vapor cell is maintained at a temperature of 110 °C so that it is above the melting point of Na (97.8 °C), but not too high to react with the glass cell. The pump beam double-passes a 80 MHz AOM, which allows us to offset the frequency of the pump, and in turn gives us the capability of controlling the locking frequency of the main laser. The effect of shifting only the pump and not the probe is that the main laser frequency when locked is red shifted by 80 MHz (half the total pump shift away from resonance). This plus the 30 MHz to go from the crossover lock point to actual resonance is compensated by the 110 MHz AOM shift for the imaging beam, which needs to be on resonance. With saturated absorption spectroscopy, we are able to lock our main diode laser for over

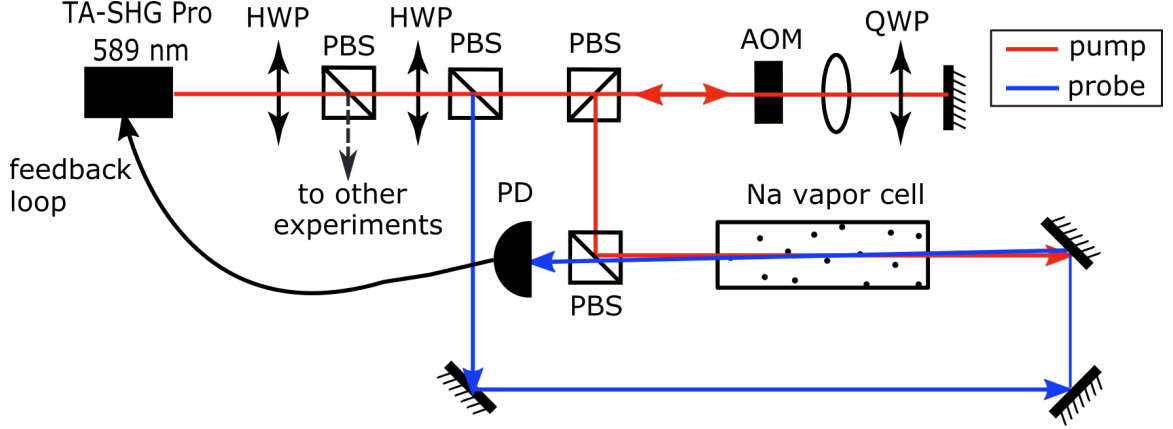


Figure 4.3: Experimental setup for FM-modulated saturated absorption spectroscopy. The pump beam (red line) and probe (blue line) are derived from the main laser. The pump is frequency shifted and FM modulated through an AOM to allow tuning of the lock point and lock-in detection with a derivative signal.

15 hours with a frequency accuracy within 1 MHz.

4.2 Four-Wave Mixing Beam Setup

Fig. 4.4 shows the optics setup of our 4WM experiment. The pump light is derived directly from our TA-SHG Pro laser beam tuned close to the D_1 resonance frequency (~ 508.335 THz) with a power of about 900 mW. A fraction of the pump beam (~ 100 mW) is diverted and frequency shifted by ~ 1.7 GHz as probe beam to seed the 4WM process. This frequency shift is achieved by sending the probe beam through a customized acousto-optical modulator (AOM) from Brimose operating at a frequency of 1.7 GHz. An AOM uses the acousto-optic effect to diffract and shift the frequency of light using sound waves (usually at radio-frequency),

$$f_{\text{out}} = f_{\text{in}} \pm n f_{\text{m}}, \quad (4.1)$$

where f_{m} is the modulation frequency of the AOM. The order of diffraction, $n=0,1,2,3,\dots$, and the sign of shift are governed by the angle of input. Here we down-shift the pump

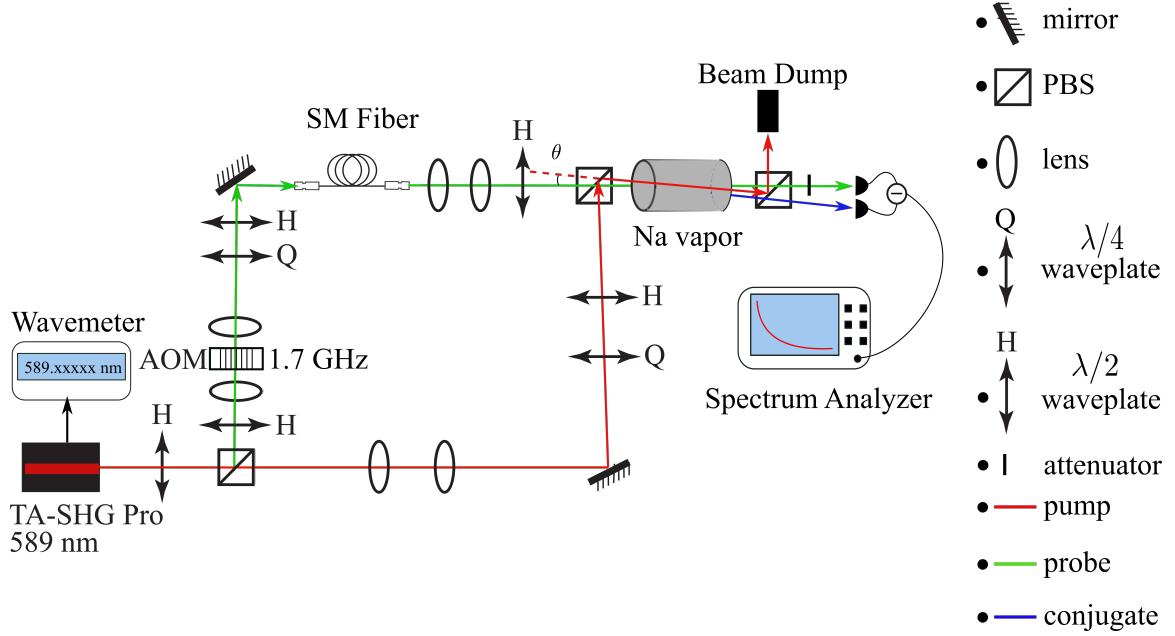


Figure 4.4: Experimental setup for 4WM experiment. The pump beam (red line) is derived from the main laser, with part of it frequency shifted through an AOM and used as the probe beam (green line) to seed the 4WM process. The probe beam is coupled into a single-mode polarization-maintaining fiber and propagates through the Na vapor cell at an angle θ with respect to the pump beam. The 4WM relative intensity noise is measured by subtracting the probe beam intensity from the conjugate beam intensity using a balanced detector. An attenuator is used on the probe beam to balance the intensities of the probe and conjugate beams.

frequency to the first order by 1.7 GHz to generate the probe beam that is used to seed the 4WM process.

Due to the unusual high operating frequency of the AOM (1.7 GHz), the diffraction efficiency is about 30%, lower than a regular AOM. Additionally, the output beam profile after the AOM is distorted as a result of the high-frequency shift. After passing the AOM, the probe beam is coupled into a single-mode, polarization-maintaining fiber to clean its spatial profile. After the fiber output coupler, an imaging system (two lenses) is used to resize and collimate the probe beam. The beam waist of the probe

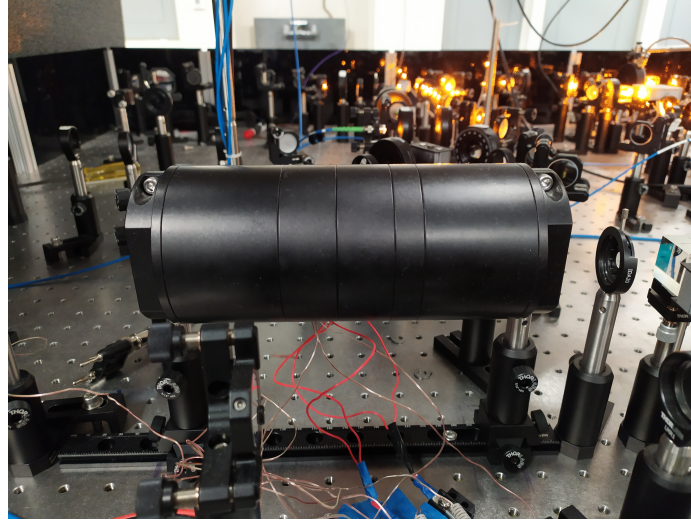
beam is positioned inside the cell, with a waist radius measured to be approximately $280 \mu\text{m}$ and a Rayleigh length of about 430 mm . The size and position of the pump beam is adjusted to have enough overlap with the probe beam. The pump beam is collimated to have a waist radius larger than the probe, around $w_0 = 520 \mu\text{m}$ inside the cell to allow more probe photons to interact with the pump photons. The pump power is much higher ($\sim 600 \text{ mW}$) than the power of the probe ($\sim 500 \mu\text{W}$), so the pump intensity remains large enough even with a large size of the pump beam.

The pump and probe beams are combined through a polarized beam splitter (PBS) placed right before the sodium vapor cell. Here, the bright pump and weak probe beam have orthogonal linear polarizations such that the p-polarized probe beam is transmitted and the s-polarized pump beam is reflected, with their portions sent into the vapor cell adjustable via the $\lambda/2$ waveplates placed before the beam-combining PBS, as shown in Fig. 4.4. At the exit of the vapor cell, another PBS is used to remove the pump light while transmitting the probe light as well as the newly created conjugate light. The removal of the pump beam after the cell is important since the bright pump light entering the detectors afterwards will add noise. In practice a small portion of the pump light is still transmitted through the PBS, but it can be blocked by a beam dump after it is separated from the probe and conjugate beam at a later point. The sodium cell is contained in a home-built oven, details of which are described in Sec. 4.3.

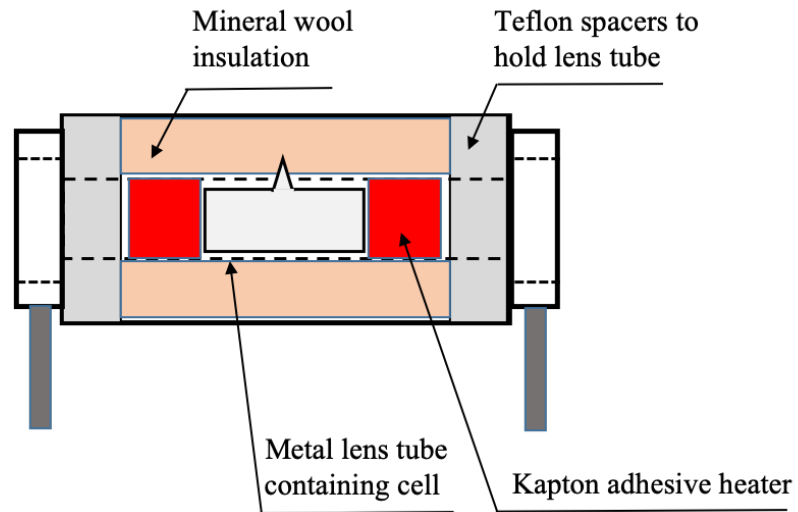
After blocking the pump light, the probe and conjugate light are sent into a balanced detector for intensity and noise detection, which will be discussed in detail in Sec. 4.4.

4.3 Vapor Cell Oven

The nonlinear medium used in our 4WM experiment is pure ^{23}Na gas contained in a 25 mm diameter, 75 mm path length Pyrex cell from Precision Glassblowing. We use a home-built oven to heat up the cell to above 150 °C, as shown in Fig. 4.5. The cell is encased in a metal lens tube with a hole on top to fit the protruding cell finger. The tube has anti-reflection coated windows to reduce losses on the generated beams, but keep the heated air inside the oven. Two Kapton heaters are adhered on the sides of the tube to generate heat, while keeping the cell windows hotter than the center to prevent sodium condensation on the windows. The heaters are connected to a PID controller to allow us to gently change the cell temperature as well as keep the temperature constant when needed. The temperature is monitored by thermocouples placed at three different positions of the cell. The lens tube is held by two Teflon spacers located at the ends of the oven, surrounded by mineral wool insulation to reduce heat dissipation as well as to keep the cell uniformly heated. With this oven combined with a corresponding optical setup, twin beams can be generated.



(a)



(b)

Figure 4.5: Home-built oven used to adjust vapor cell temperature. (a) Picture of the oven positioned on the optical table. (b) Schematic of the oven design. Within the oven, a lens tube with two anti-reflection coated windows is used to hold the Na cell. Heat is transferred to the lens tube through heaters adhered to the outside of the tube. Mineral wool insulation is used between the oven and lens tube to prevent heat dissipation. The heaters are connected to a PID controller to keep the temperature constant. The temperature is monitored by thermocouples placed at the two ends and center of the lens tube (not shown here).

4.4 Signal and Noise Detection

As shown in Fig. 4.4, after exiting the vapor cell, the pump beam is reflected by a PBS to a beam dump, with the residual blocked by another beam dump later where the three beams are spatially separated (not shown in Fig. 4.4). The probe/conjugate beams are transmitted through the PBS and separated after a long optical path (~ 1 m). Before entering the detector, a variable attenuator is placed in the path of the probe beam to introduce loss on the probe and balance the intensities between the probe and conjugate beams. The balanced detector used in this experiment is a PDB-450A from Thorlabs with an operating wavelength range of 320 - 1000 nm. This balanced detector has two Silicon photodiodes, which can be used to detect the probe and conjugate fields simultaneously. It has two monitor ports which output DC voltage signals that are proportional to the intensity of the probe and conjugate beam, respectively. There is also a RF output which is able to measure small differences between two optical input signals while suppressing common fluctuations. The RF output bandwidth is switchable, with options DC/150/45/4/0.3/0.1 MHz, and the corresponding RF output gains are $10^3/10^4/10^5/10^6/10^7$ V/A. The output RF signal is displayed on a spectrum analyzer to show the noise level.

4.5 Summary

In summary, we described how we derive probe and pump light from a diode laser and send them into a sodium vapor cell heated by a home-built oven. The four-wave mixing interaction, which occurs inside the sodium cell generates a new light field called conjugate light. The intensities of the newly generated conjugate light and the amplified probe light are measured by a balanced detector, which also measures their relative intensity noise together with a spectrum analyzer.

Chapter 5

Experimental Results on Four-Wave Mixing in Hot Na Vapors

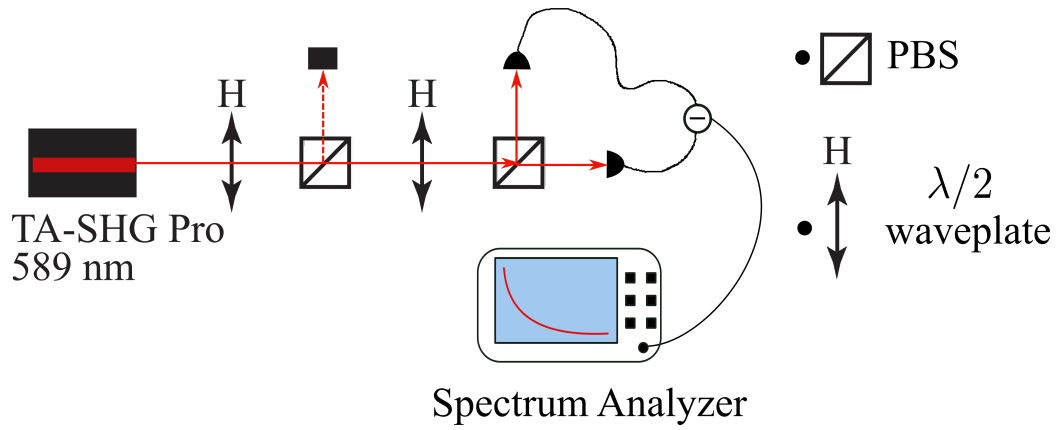
In this chapter, we show the implementation of 4WM experiments to generate two-mode squeezed states of light. The experimental results are presented, including the shot noise calibration, and the measurements of the 4WM gain and noise. We also present the application of saturated absorption light to reduce the absorption losses, and our design of a stainless steel vapor cell that will be able to function at higher temperatures to increase the gain in the future.

5.1 Calibration of Shot Noise Limit

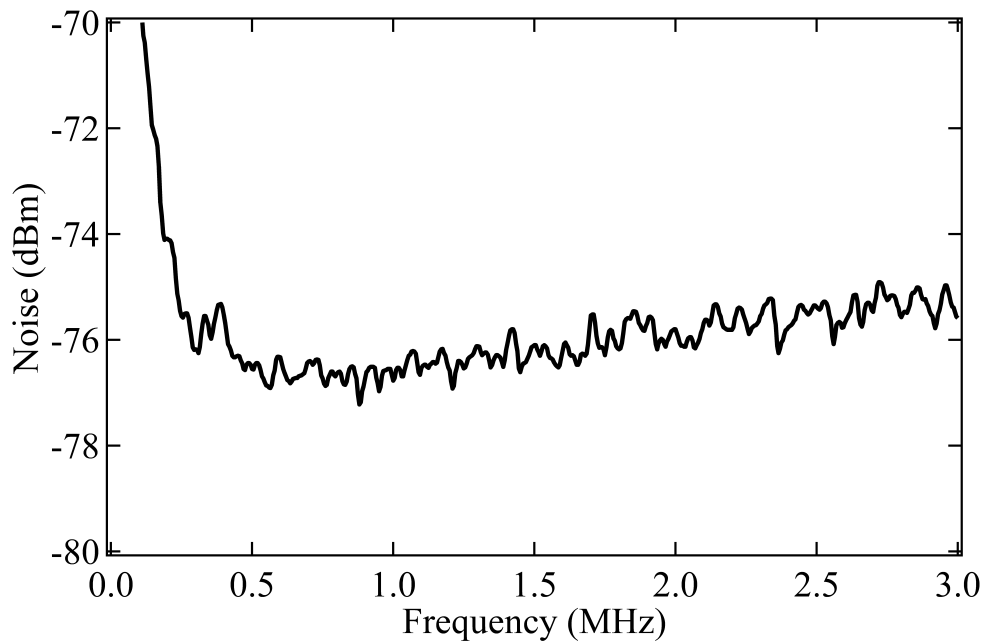
To characterize quantum squeezed states of light, we will compare the relative noise of the probe and conjugate signals with the shot noise limit (SNL). As mentioned in Chapter 2, the shot noise is an intrinsic property of light due to its particle nature. The statistical distribution of the shot noise can be modeled by a Poisson distribution. For coherent laser light, the fluctuation of a photo-current ΔI scales as the square-root of the light intensity I :

$$(\Delta I)^2 = \langle (I - \langle I \rangle)^2 \rangle \propto I. \quad (5.1)$$

Our shot noise was calibrated by measuring the electrical noise of two balanced beams generated by a PBS in the analysis frequency range of 0-3 MHz, where the noise spectrum is relatively flat, as described in Fig. 5.1. We calibrated the shot noise limit and it serves as a reference point for the experiment's other noise measurements since it is an intrinsic and expected property of light. As shown in Fig. 5.2, our measured shot noise has a linear relationship with total laser power. The noise was measured over a 3 MHz frequency range as a reference for all of our noise measurements. The spectrum



(a)



(b)

Figure 5.1: Illustration of shot noise calibration. (a) Experimental setup for balanced beam shot noise detection. The first waveplate and PBS are used to purify the light polarization, while the second waveplate and PBS are used to balance the beam powers. (b) Measured shot noise spectrum at a total power of 80 mW.

analyzer has a resolution bandwidth (RBW) of 30 kHz and a video bandwidth (VBW) of 100 Hz. The calibration is used to experimentally determine the shot noise limit, which is then compared with the relative intensity noise of probe and conjugate beams

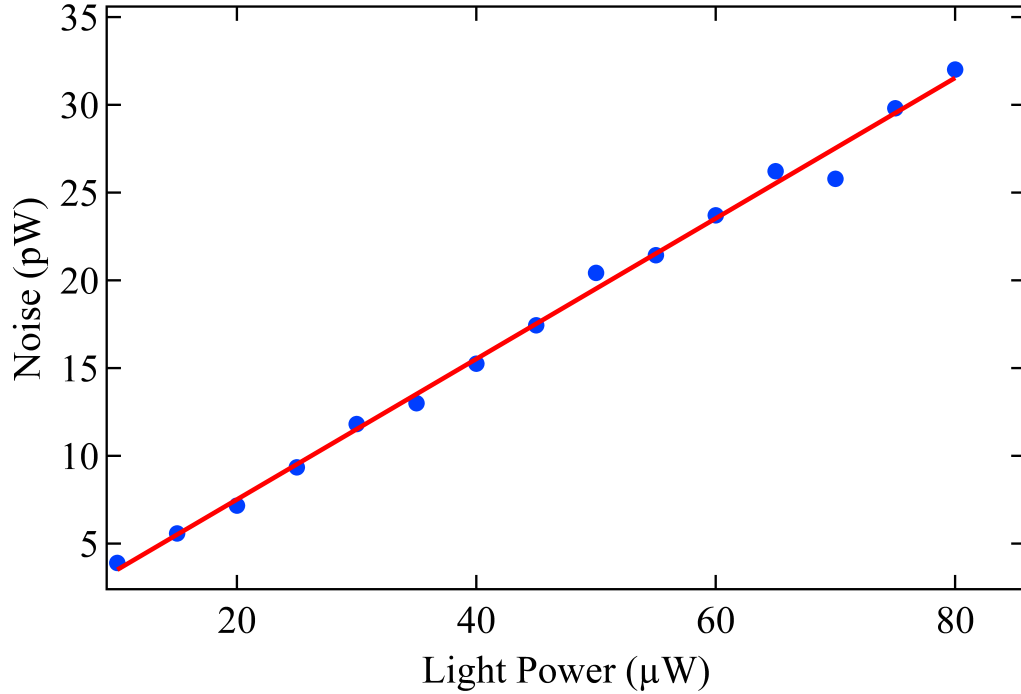


Figure 5.2: Measured shot noise limit as a function of power. The shot noise power is linear in the power of the laser light, as expected.

when investigating the relative intensity squeezing.

5.2 Four-Wave Mixing Gain Characterization

An important parameter to characterize the four-wave mixing interaction strength is the gain of probe and conjugate signals, which is defined as the gain in intensity and can be calculated using:

$$G = \frac{P}{P_{\text{off}}}, \quad (5.2)$$

where P is the power of the probe or conjugate signal, and P_{off} is the power of the probe beam when it is tuned far off-resonance and the pump beam is off. The gain is normalized against the probe intensity far away from resonance because at such a frequency the probe field does not interact with the atoms and thus provides a good

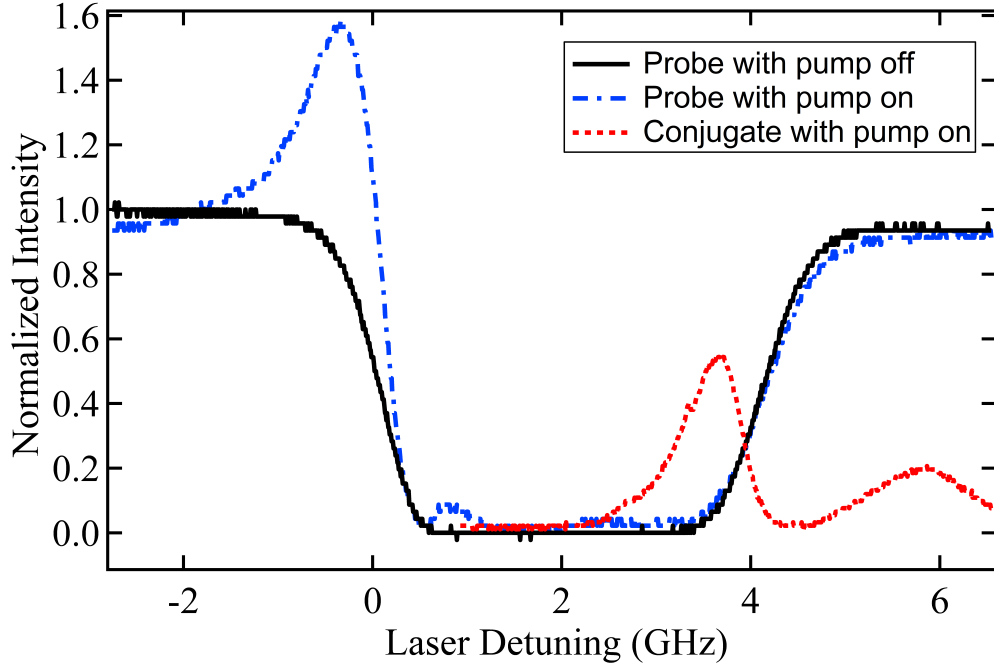


Figure 5.3: The response of probe and conjugate beams when the one-photon detuning (Δ) is scanned across the 4WM resonance spectrum. The probe spectrum without pump field (black solid) shows the Doppler-broadened absorption profile. The probe signal with pump field on (blue dash-dotted) shows the probe gain of the 4WM process. The conjugate signal (red dashed) is only observed when the pump field is applied. Here, the conjugate signal was shifted by ~ 3.4 GHz to illustrate where the conjugate frequency lies in the Doppler broadened absorption profile.

reference point.

Fig. 5.3 shows an example observation of the probe and conjugate fields on the Na D_1 line in the double- Λ configuration when scanning the one-photon detuning Δ . The observation of the probe and conjugate signals shows that the double- Λ configuration and our experimental setup are functioning on Na in principle. The probe and conjugate peaks can also be observed on an index card as the main laser is scanned. The probe peak in the off-resonance region gives a gain of ~ 1.6 . We observed two conjugate peaks, one in the off-resonance regime with a gain of 0.2, and

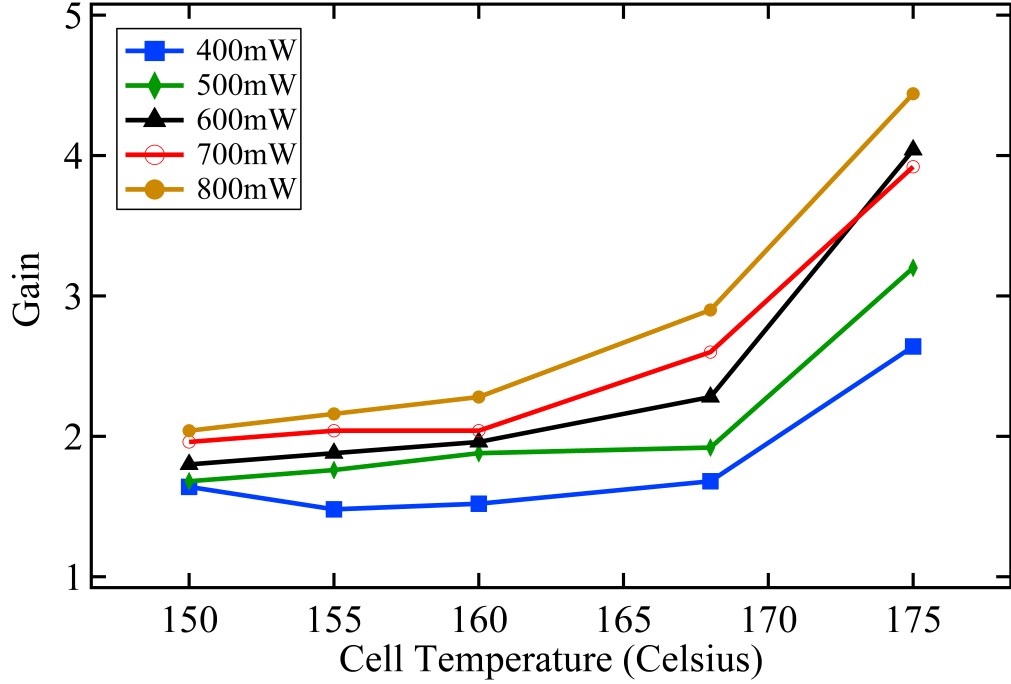


Figure 5.4: Dependence of probe gain on pump power and cell temperature. The probe was measured at a two-photon detuning $\delta = -11$ MHz, pump beam waist $w_p = 490 \mu\text{m}$, probe beam waist $w_{pr} = 264 \mu\text{m}$, input probe power $170 \mu\text{W}$ and probe-pump angle $\theta = 0.12^\circ$. The one-photon detuning Δ , was optimized at each data point for maximum gain. Each trace corresponds to a different pump power, as shown in the legend.

the other peak is in the near-resonance regime with a gain of 0.6, which corresponds to the off-resonance probe peak. The gain of the probe and conjugate are somewhat small compared with those in Rb 4WM experiments. So, we needed to optimize the experimental parameters to improve the gain.

The four-wave mixing gain depends on many experimental parameters. It can be optimized by adjusting the beam alignment to change the pump-probe angle θ , the one-photon detuning Δ , two photon detuning δ , pump power, and the vapor cell temperature T . Fig. 5.4 shows the probe gain dependence on pump power and vapor cell temperature. As revealed by the figure, increasing the pump power and

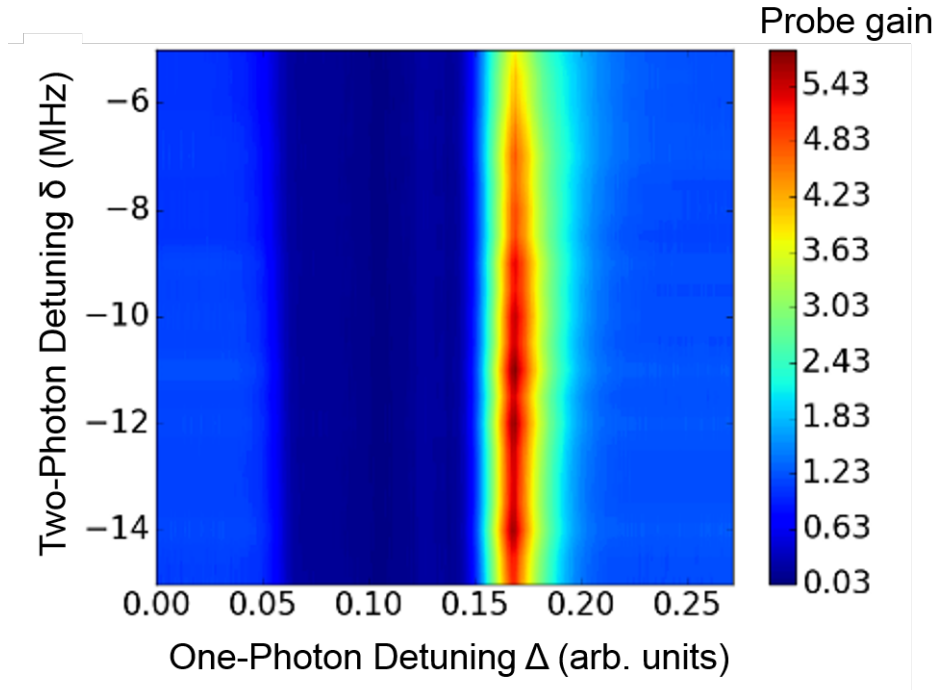


Figure 5.5: Dependence of probe gain on one-photon detuning Δ and two photon detuning δ .

cell temperature was found to increase the probe gain. However, increasing these two parameters is difficult due to experimental limitations. The pump power is limited due to the total power of 1 W from the main laser. The temperature is limited because the glass cell starts reacting with the sodium at temperatures above 120 °C. Several vapor cells were destroyed in the course of these measurements.

Apart from pump power and cell temperature, the impact of detunings on probe gain is also investigated. This experiment is performed by scanning the main laser frequency (corresponding to scanning one-photon detuning Δ), while the two-photon detuning δ and the input angle θ were fixed. We also scan the two-photon detuning δ by changing the AOM driving frequency while keeping Δ fixed. The measurements of the probe gain as a function of both detunings is shown in Fig. 5.5. There are large detuning regions (Δ and δ) where a net gain larger than one can be observed.

5.3 Four-Wave Mixing Noise Measurements

The noise spectrum of the beams generated by four-wave mixing are investigated to observe the correlations. We measure the noise spectrum of the individual probe and conjugate beams as well as their relative noise spectrum, which is then compared with the shot noise limit. The probe and conjugate beam exiting the cell have imbalanced intensities due to imbalanced gains and losses, as shown in Fig. 5.3. The intensity imbalance can increase the relative intensity noise, because the relative intensity noise reduction is achieved through adding correlated photons to the probe and conjugate beam that allow the fluctuations to be subtracted. A higher-intensity probe beam carries fluctuations which can not be cancelled by the conjugate beam [46]. In order to reduce this noise contribution, we use a variable density attenuator to introduce loss on the probe beam, at expense of destroying some correlated photons. By optimizing the probe attenuation, these two effects can be balanced and a minimum relative intensity noise is achieved. As shown in Fig. 5.6, we observe a significant noise reduction of the relative noise spectrum with respect to the individual beam noises, demonstrating the noise cancellation between the probe and conjugate beams. The relative noise approaches the shot noise limit, with an average of about 1 dB difference.

To summarize, we observe net gain in our 4WM experiment (gain of probe ranges from 1 to 5 depending on the cell temperature), and a significant lower relative noise than each individual noise of probe/conjugate beams at the same intensity. However, noise squeezing is not achieved yet, which we attribute to two main factors. Firstly, the large Doppler broadening and small hyperfine splitting (1.77 GHz for ^{23}Na vs. 3.03 GHz for ^{85}Rb) makes the absorption loss much higher compared to 4WM experiments using ^{85}Rb [2, 44]. The large absorption loss, which is as high as about 80%, destroys a large number of the correlated photons, which are needed to realize noise squeezing. Secondly, the intrinsic gain of the 4WM process is currently not high

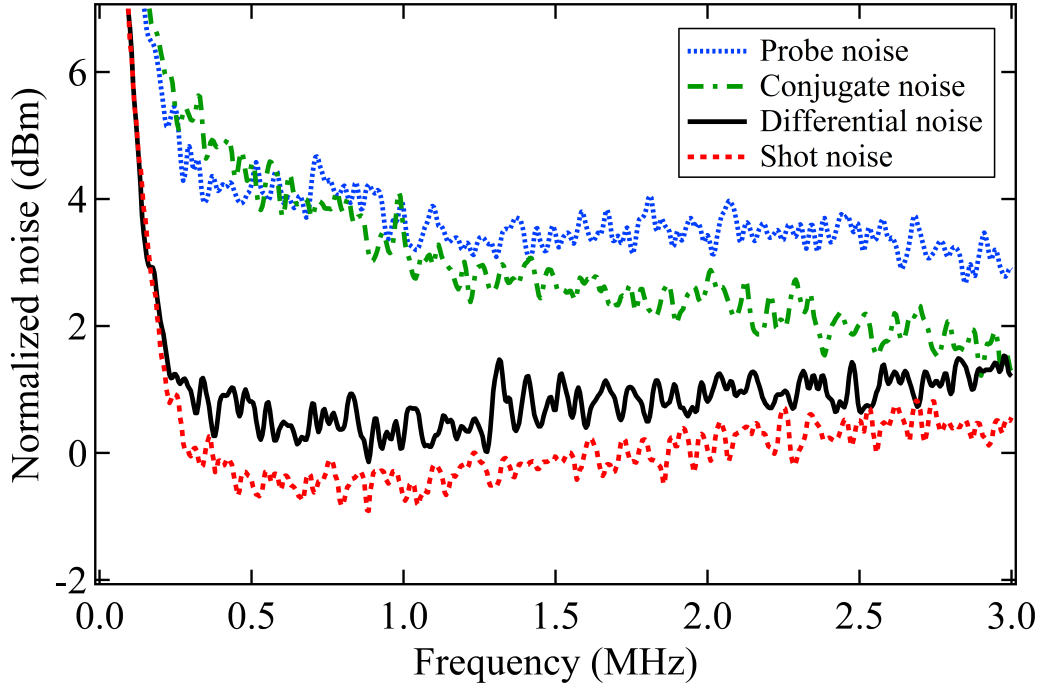


Figure 5.6: Measured noise spectrum of individual probe and conjugate beams, the relative intensity noise and the shot noise limit. Here, the cell temperature $T = 160$ °C, the probe-pump angle $\theta = 0.12^\circ$, and two-photon detuning $\delta = -11$ MHz. One-photon detuning was optimized for the lowest relative noise.

enough, especially in the presence of large losses. The competition between the gain and the loss determines the squeezing level of the relative noise. The gain generates the correlated photons, and loss reduces the correlated photons. So our efforts are directed to reducing the loss and increasing the gain.

5.4 Saturated Absorption Light

In order to reduce losses, we apply a saturated absorption method to reduce the conjugate absorption loss inside the hot vapor. In the saturated absorption method, a saturating beam with high intensity, $I \approx I_{sat}$, near resonance frequency, $\omega \approx \omega_0$, propagates in the opposite direction of the conjugate beam and saturates the atomic

transition. The saturation creates a narrow peak in the intensity of the conjugate beam transmitted through the medium [47]. We built a saturated absorption optical system using tunable yellow light from a dye laser (CR-599) providing 5 mW saturating power. Fig. 5.7 shows the optical setup of the 4WM experiment with saturated absorption beam aligned to counter-propagate the conjugate beam inside the vapor cell.

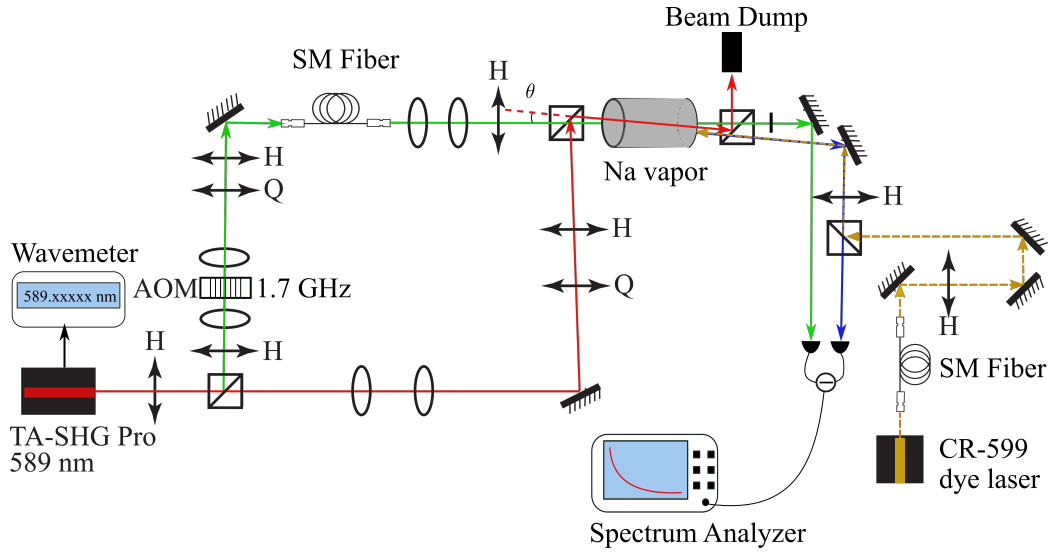
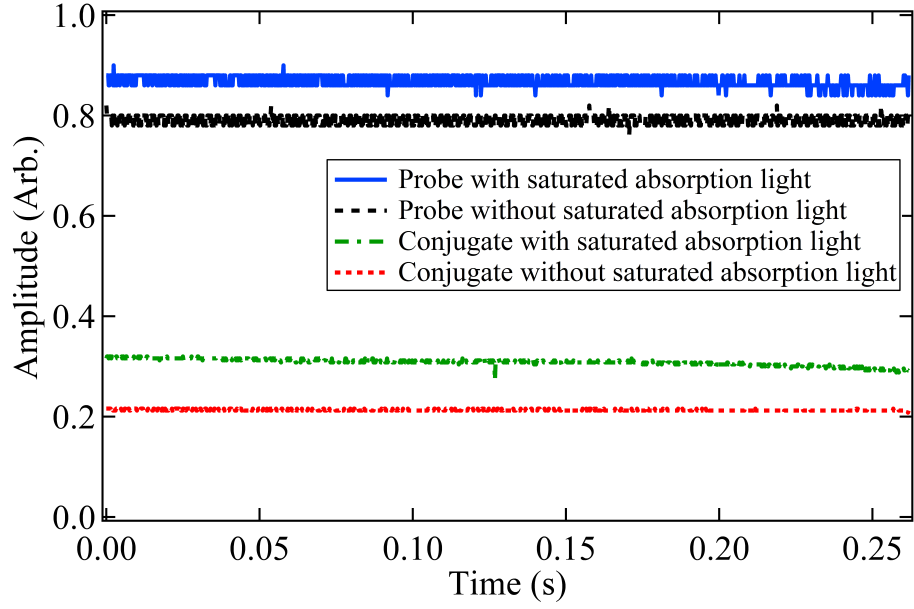


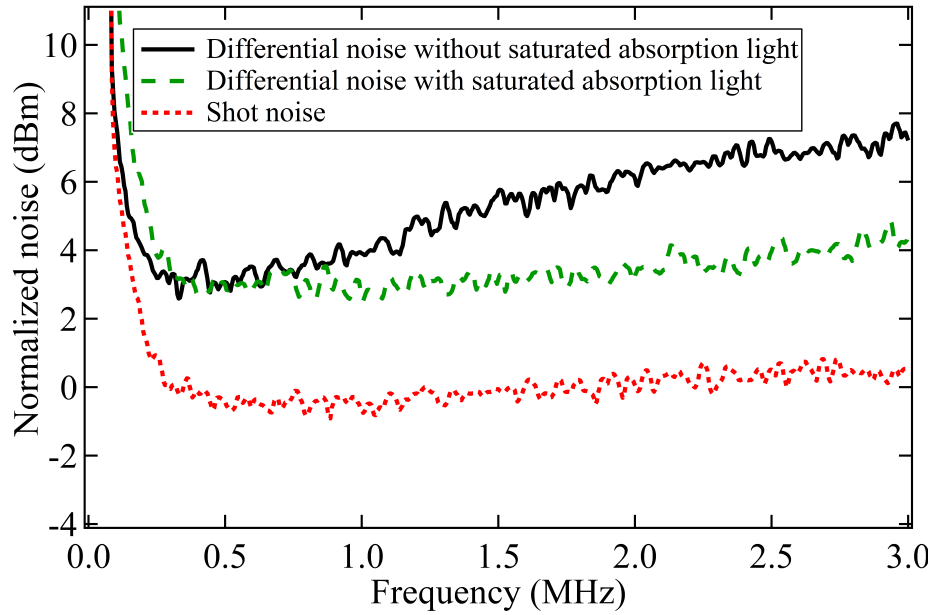
Figure 5.7: Experimental setup with an on-resonance saturating beam. The saturating beam is counter-propagating with the conjugate beam at the same frequency, to saturate the atomic absorption and reduce conjugate absorption loss.

Fig. 5.8 shows the intensities of the probe and conjugate beams vs. time, and the relative intensity noise before and after applying saturated absorption light. We observed a signal enhancement by at least 50% for the conjugate beam, 10% for the probe beam, and a relative intensity noise reduction, especially at higher frequencies, as an effect of our saturated absorption beam. The noise increase at high frequencies when the saturated absorption beam is absent is probably due to the fluctuations from the intensity and frequency noise in our diode laser: the second-harmonic generation (SHG) system converts frequency noise to additional intensity noise. This noise is not daily consistent and we sometime observe increased levels of noise, especially

at higher frequencies of the spectrum. Meanwhile, we see from Fig. 5.8 that the saturated absorption beam introduces some time-dependent noise drifts on the probe and conjugate signal, due to the fact that the saturating light from our old dye laser is somewhat unstable and drifts in amplitude and frequency. The instability of the saturating beam comes from sources such as bubbles in the dye jet and pressure fluctuation of the jet. It adds additional noise to the probe/conjugate beam, which also contributes to the 4WM relative noise as the noise added to the probe and conjugate are not equal and cannot be fully cancelled. Our results suggest that the saturated absorption method is beneficial in reducing the probe/conjugate loss due to absorption inside the vapor cell and that the relative noise can be reduced by this method. However, a stronger and more stable saturating light, possibly from a solid state laser source, instead of a dye laser, would be needed.



(a)



(b)

Figure 5.8: 4WM signals and noise with saturated absorption light. (a) Probe and conjugate intensities with and without saturated absorption light vs. time. (b) Saturated absorption light reduces the relative noise. The results suggest that by applying saturated absorption light, the gain of the probe and conjugate beams can be enhanced, and their relative noise can be reduced.

5.5 A New Vapor Cell Design

As shown in Fig. 5.4, increasing pump power and cell temperature could increase the gain. The pump power, however, is limited by the total output power of our main laser. Increasing the cell temperature actually increases the vapor pressure in the cell, thus increasing the atomic density. The vapor pressure in Na is about three magnitudes lower compared to that in Rb, as shown in Fig. 5.9. So in order to obtain the same vapor pressure, a much higher temperature is required. On the other hand, cell temperature is limited because sodium starts reacting with the Pyrex glass of our cell at temperatures higher than 120 °C. To solve this, we are designing a stainless steel vapor cell that can heat up to 400 °C. Fig. 5.10 shows the design of our new cell. The main part of the system is made of stainless steel and can heat up to a higher temperature without reacting with sodium. The sodium, when it is solid, is contained in a stainless steel cup, which can be filled with extra sodium so that it lasts longer and it's also easy to refill.

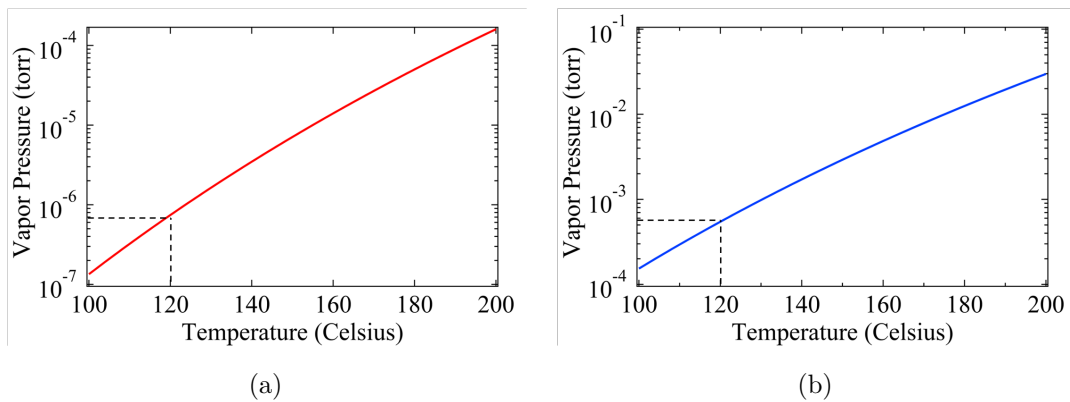


Figure 5.9: Vapor pressure of (a) Na and (b) Rb. The dashed lines are the corresponding vapor pressure at temperature $T = 120$ °C. Models are Eq. (1) in Ref. [45, 48].

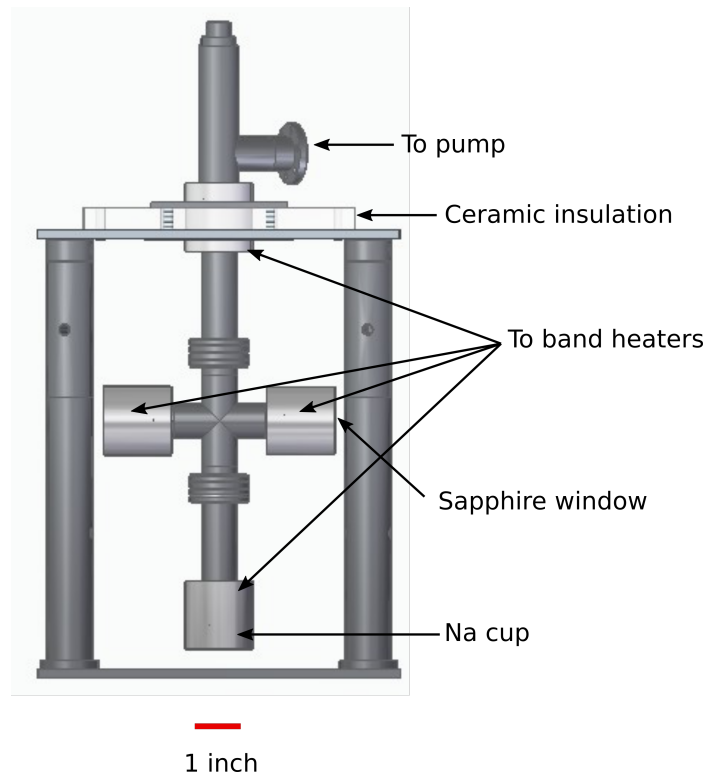


Figure 5.10: The new stainless steel cell design. The main part of the system is made of stainless steel so it can work at much higher temperatures than a glass vapor cell. The removable sodium cup can contain more sodium material so that it lasts longer, and refills easily. The two anti-reflected coated sapphire windows can work at high temperatures with little reflection and without destructible reactions with hot Na vapor.

5.6 Summary and Outlook

To generate twin beams of yellow light at 589 nm, we set up an experimental system that can realize the four-wave mixing on sodium with a double- Λ configuration. The conjugate beam was observed at the output of the hot sodium vapor cell with input seeding probe light, which nearly co-propagates with the pump beam. Gains ranging from 1-5 were observed depending on the pump power and the cell temperature. There was a reduction of about 2 dB on the relative intensity noise of the probe and conjugate light from their individual noises, showing that correlated photons were

created. There is a significant level of absorption loss due to the Doppler broadened sodium D_1 line. The lower atomic density in our Na experiments compared to that in Rb, due to the vapor pressure being about three magnitudes lower than that of Rb, also limits the gain in our experiments.

We tested a saturated absorption method which increased the gain of the probe and conjugate beam by $\sim 10\%$ and $\sim 50\%$ respectively, even with our comparatively noisy and weak dye laser. The results suggest that with a more stable and powerful light source for the saturated absorption setup, the absorption and the relative noise can be further reduced.

We are currently working on building a new stainless steel cell to overcome the temperature limitation of the current glass vapor cell. The new cell will allow us to dramatically increase the temperature and thus lead to higher gain. Combined with the improved saturated absorption setup, it is very promising that we will achieve quantum squeezing in the near future.

Once squeezing is observed, we plan to apply the squeezed states of light in our Na spinor BEC experiments, to enhance the signal-to-noise ratio in atom number measurements and explore the interfacing of quantum squeezed states of light with entangled spin-states of matter waves in the BEC.

In the next chapters, I will switch from photons to atoms and describe our experiments on matter-wave quantum optics with our Na spinor BECs.

Chapter 6

Theory of Spin-Mixing in Na Spinor BECs

In Chapter 6, and the following three chapters, we will discuss the theory and experimental results of creating an atomic interferometer with quantum-enhanced sensitivity based on spin-exchange collisions in $F = 1$ spinor Bose-Einstein condensates. Spin-exchange collisions in $F = 1$ spinor Bose-Einstein condensates, where two atoms with magnetic quantum number $m_F = 0$ collide and change into a pair with $m_F = \pm 1$, are useful to implement matter-wave quantum optics in spin space, such as quantum-enhanced interferometry, because the collisions generate entanglement and they can be precisely controlled using microwave dressing. We are interested in atomic interferometry in spinor BECs because it has applications in quantum-enhanced sensing. The control of collisions via microwave dressing explained in this chapter, together with our versatile experimental platform I helped to design and construct, allow us to study quantum engineering of matter waves for a new generation of quantum technologies based on matter-wave quantum optics. Examples of such quantum technologies are quantum-enhanced sensors for external fields with high spatial resolution [49], quantum-enhanced probes of ultracold atomic samples to measure spin populations with reduced noise [50], and quantum-enhanced matter-wave devices such as phase-sensitive amplifiers [51], similar to those known from quantum optics with light.

In this chapter, the theory of spin-exchange collisions in spinor BEC is described in detail. This starts with an introduction to BEC and the spin-mixing Hamiltonian. The techniques to create and manipulate BEC, including laser cooling and trapping, microwave dressing, and the sequence to realize atomic interferometry are also presented in detail.

6.1 Introduction to BEC

A Bose-Einstein condensate (BEC) is an exotic phase of matter predicted by Bose and Einstein in 1924 where identical bosonic particles macroscopically occupy the same quantum state (ground state) of an external potential and act as a single quantum entity [22, 23]. It typically occurs when the temperature falls below a critical temperature T_c . For dilute atomic gases, T_c is typically in the regime of nanoKelvin [52]. Bose-Einstein condensation is caused by the quantum statistics of Bosons, in contrast to other phase transitions such as melting and evaporating, which depend on inter-atomic interactions. However, experimental realization of a BEC was difficult because the critical temperature T_c was too low to realize under the technical conditions at that time. Until 1995, 71 years after the prediction, with the help of new techniques, especially laser cooling and trapping, and evaporative cooling, Bose-Einstein condensation was first observed in dilute rubidium gases by Eric Cornell and Carl Wieman [24]. Since then BECs of sodium, lithium and many other alkali atoms have also been realized [25, 53]. Subsequently, Steven Chu, Claude N. Cohen-Tannoudji and William D. Phillips were awarded the Nobel Prize in physics in 1997 for their contributions of laser cooling, which made BEC possible [54, 55, 56]. In 2001, Eric Cornell, Wolfgang Ketterle and Carl Wieman were awarded the Nobel Prize in physics for the experimental achievement of Bose-Einstein condensation in dilute atomic gases [57, 58].

The phase transition to a BEC can be related to particle's thermal de Broglie wavelength λ_{dB} ,

$$\lambda_{dB} = \sqrt{\frac{2\pi\hbar^2}{mk_B T}}, \quad (6.1)$$

where m is the mass of the particle, \hbar is the reduced Planck's constant ($\hbar = h/2\pi$), and k_B is the Boltzmann constant. At high temperatures, λ_{dB} is small compared to

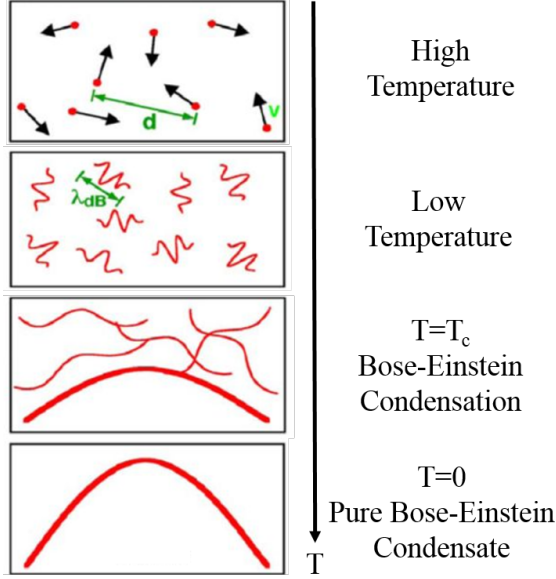


Figure 6.1: Cartoon of the phase transition to a BEC. At high temperatures, the inter-atomic distance is much larger than their wavelength, and atoms can be treated as classical particles. As the gas is cooled down, the wave nature becomes more dominant. At a critical temperature T_c , the atomic wavefunctions overlap and start to form a BEC. At zero temperature, the atoms form a pure BEC. Figure inspired by Ref. [60].

the spacing between atoms and the gas behaves classically, like point particles. As the temperature decreases, quantum effects become more apparent and the atoms behave more like waves. When the temperature is so low that λ_{dB} is comparable to the average inter-particle distance, approximately $(\frac{V}{N})^{1/3}$, with V and N the volume and the total number of particles of the gas, respectively, the individual atomic wavefunctions will overlap, and a condensate forms [59], as shown in Fig. 6.1.

The transition to a BEC occurs below a critical temperature T_c , which satisfies [61]

$$n\lambda_{dB}^3 \approx 2.612, \quad (6.2)$$

where $n = N/V$ is the particle density, and $n\lambda_{dB}^3 = D$ is the phase-space density.

Substituting λ_{dB} with Eq. (6.1), the critical temperature can be expressed as

$$T_c \approx 3.3125 \frac{\hbar^2 n^{2/3}}{m k_B}. \quad (6.3)$$

For trapped alkali atoms with typical densities of $10^{13} - 10^{15} \text{ cm}^{-3}$, the critical temperature T_c is in the order of ten nK to a few μK .

6.2 Spin-Mixing Hamiltonian

Because the particles in the BEC are all in a single quantum state, thousands or even millions of atoms in the BEC can behave like a single quantum particle. A single-component atomic BEC is typically described by a scalar order parameter (macroscopic wavefunction) $\psi(\mathbf{r}, \mathbf{t})$ whose dynamics are governed by the Gross-Pitaevskii equation [52],

$$i\hbar \frac{\partial \psi}{\partial t} = \left(-\frac{\hbar^2}{2m} \nabla^2 + V_t + g|\psi|^2 \right) \psi, \quad (6.4)$$

where V_t is the external trapping potential, g is the two-body mean-field interaction coefficient, and $|\psi|^2 = n$ is the particle density.

Atomic Bose-Einstein condensates with internal spin degrees of freedom are called spinor condensates [62]. For each hyperfine state with total angular momentum F , there are $2F + 1$ Zeeman sublevels. Thus the wavefunction of spinor condensates is extended to a vector order parameter $\boldsymbol{\psi} = [\psi_F, \psi_{F-1}, \dots, \psi_{-F}]^T$, which includes $2F + 1$ components.

The atomic interactions inside spinor condensates are dominated by two-body s-wave collisions. The sodium $F = 1$ spinor condensates are composed of three spin components, corresponding to three Zeeman sublevels, labeled as $m_F = -1, 0, +1$ respectively, where m_F is the magnetic quantum number. The microscopic picture of spin-exchange collisions is shown in Fig. 6.2, where two $m_F = 0$ atoms approach each other and their spins will couple together via the spin-exchange interaction. After

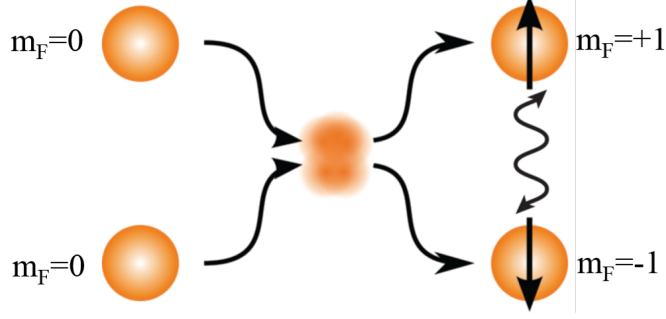


Figure 6.2: Cartoon of a spin-exchange collision. Two $m_F = 0$ atoms collide and change into a pair of entangled $m_F = \pm 1$ atoms.

the collision, their spins decouple, having changed into a pair of entangled $m_F = \pm 1$ atoms. During the process, the total spin and magnetization of the two atoms are conserved. The generation of entangled pairs is similar to four-wave mixing in optics with photons.

The total hyperfine angular momentum of two colliding atoms is given by $\mathbf{f} = \mathbf{F}_1 + \mathbf{F}_2$. For two identical spin-1 atoms, f can only take two values of $f = 0, 2$ [63]. So in a $F = 1$ spinor system, the inter-atomic interactions are described by two atomic parameters, i.e., the scattering lengths a_0 and a_2 for two allowed collision channels of total spin 0 and 2. The interaction potential is [64]

$$V_{\text{int}}(\mathbf{r}_1 - \mathbf{r}_2) = (c_0 + c_2 \hat{\mathbf{F}}_1 \cdot \hat{\mathbf{F}}_2) \delta(\mathbf{r}_1 - \mathbf{r}_2), \quad (6.5)$$

where $\hat{\mathbf{F}}_1$ and $\hat{\mathbf{F}}_2$ are the spin operators of the two particles, c_0 and c_2 are interaction parameters defined as [65]

$$c_0 = \frac{g_0 + 2g_2}{3} = \frac{4\pi\hbar^2}{m} \frac{2a_2 + a_0}{3} = \frac{4\pi\hbar^2}{m} \bar{a}, \quad (6.6)$$

$$c_2 = \frac{-g_0 + g_2}{3} = \frac{4\pi\hbar^2}{m} \frac{a_2 - a_0}{3} = \frac{4\pi\hbar^2}{m} \Delta a, \quad (6.7)$$

where $g_F = \frac{4\pi\hbar^2}{m} a_F$ is the coupling strength, $\bar{a} = (2a_2 + a_0)/3$ is the mean s-wave scattering length, and $\Delta a = (a_2 - a_0)/3$ is the scattering length difference.

The total Hamiltonian of the spinor condensates can be written as [65]

$$H = \sum_{i=1}^N \frac{p_i^2}{2m} + U(r_i) + \sum_{i<j} V(\mathbf{r}_i - \mathbf{r}_j) \quad (6.8)$$

$$= \sum_{i=1}^N \frac{p_i^2}{2m} + U(r_i) + \sum_{i<j} (c_0 + c_2 \hat{\mathbf{F}}_i \cdot \hat{\mathbf{F}}_j) \delta(\mathbf{r}_i - \mathbf{r}_j), \quad (6.9)$$

where $U(r_i)$ is the total external potential including the trapping potential and external magnetic fields, and N is the total number of atoms in the condensate.

$F = 1$ spinor BECs can be divided into two categories depending on the sign of the spin-dependent interaction parameter c_2 :

- $c_2 < 0$: the collisional coupling is ferromagnetic because the condensate maximizes $\hat{\mathbf{F}}_1 \cdot \hat{\mathbf{F}}_2$ and consequently minimizes its energy by aligning all the spins to be polarized in the same direction. An example of a ferromagnetic spinor condensate is a rubidium condensate [64].
- $c_2 > 0$: the collisional coupling is anti-ferromagnetic because the condensate minimizes $\hat{\mathbf{F}}_1 \cdot \hat{\mathbf{F}}_2$ and consequently minimizes its energy by aligning all the spins to be polarized in opposite directions. A sodium condensate is anti-ferromagnetic [64, 66].

In addition to atom-atom interactions, there are also interactions between a spinor condensate and external magnetic fields. For example, a homogeneous static magnetic field can change the total Zeeman energy of a spinor condensate. The linear Zeeman energy and the quadratic Zeeman energy of a spinor in a homogeneous magnetic field of magnitude B_0 are

$$E_{\text{linear}} = -g_J \mu_B m_F B_0, \quad (6.10)$$

$$E_{\text{quad}} = E_{\text{quad}}^0 B_0^2 + \gamma m_F^2 B_0^2, \quad (6.11)$$

where g_J is the Landé g-factor, μ_B is the Bohr magneton, $g_J \mu_B \approx h \times 702$ kHz/G, $\gamma \approx h \times 277$ Hz/G² and $E_{\text{quad}}^0 \approx -h \times 1.109$ kHz/G² for sodium atoms in the $3^2S_{1/2}, F = 1$ ground state [45].

In a $F = 1$ spin-exchange collision where the total spin is conserved,

$$|m_F = 0\rangle + |m_F = 0\rangle \leftrightarrow |m_F = +1\rangle + |m_F = -1\rangle, \quad (6.12)$$

according to Eq. (6.10), the total linear Zeeman effect and the offset energy term $\propto E_{\text{quad}}^0$ of the collisional atomic pair are exactly canceled. This is important as it allows us to observe weak spin-dependent interactions in experiments even at large background magnetic fields on the order of hundreds of mG where the spin-exchange collisional energy scale is orders of magnitude smaller than the energy due to the linear Zeeman shift. The total quadratic Zeeman energy on the right side of Eq. (6.12) is larger than that on the left side and therefore energetically favors this process going to the left for non-zero applied B-field, as shown in Fig. 6.3 (left). This quadratic Zeeman energy difference is denoted by q , which is controllable via microwave dressing, see Sec. 6.4 for more details. In experiments, we first prepare all the atoms in the $m_F = 0$ state in the presence of a constant background magnetic field. If the $m_F = 0$ energy level is far below the $m_F = \pm 1$ states, spin population oscillation does not happen at this point, because it is energetically not allowed. We then start the spin population oscillation process by quickly (within 1 ms) turning on a blue-detuned microwave dressing field that selectively shifts the $m_F = 0$ state to higher energies, that is, q becomes negative. Now the atoms in $m_F = 0$ states start converting into pairs of atoms in $m_F = \pm 1$ states, as shown in Fig. 6.3 (right). This step represents a quench of the system. The details of tuning q are discussed in Sec. 6.4.

The spin-exchange collisions cause characteristic population oscillations between the $m_F = 0$ and the $m_F = \pm 1$ states. They amplify vacuum fluctuations in the initial states [67], and create exotic quantum many-body spin states such as spin-nematic squeezed states [68], two-mode spin squeezing [69] and the even more exotic non-Gaussian spin-squeezed states [70, 71]. The study of spin-exchange collisions is an active research frontier because the collisions generate quantum correlated

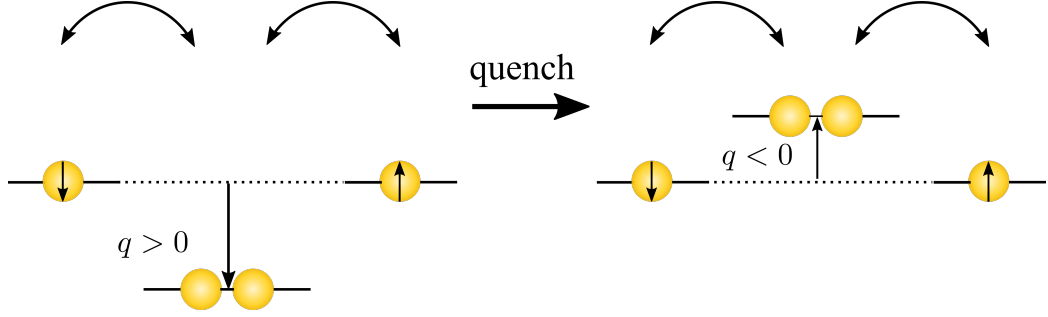


Figure 6.3: Schematic of a quench process illustrated with pair-energy diagrams. Left: Effective quadratic Zeeman shift of $F=1$ spinors in the presence of a constant background magnetic field. The effective quadratic Zeeman shift $q > 0$, $q \approx h \times 277 \text{ Hz/G}^2$. Right: The system is quenched by a microwave field such that it is switched to $q < 0$. The curves with arrows means that spin-exchange collisions cause reversible population transfer between the $m_F = 0$ and the $m_F = \pm 1$ states.

states including squeezed and entangled states, which have a wide range of important applications in matter-wave quantum optics, because they can be controlled precisely by microwave dressing. In addition to giving a new tool to study fundamental principles of many-body quantum mechanics [72], spinor BECs have applications in quantum metrology, quantum information processing and many other fields [62]. For example, high-resolution magnetometry and interferometry have been realized with sensitivities close to or below the standard quantum limit (SQL) that fundamentally limits the precision of measurements for uncorrelated atoms [73, 74]. In analogy to four-wave mixing in optics, the generation of quantum correlated states in a BEC represents four-wave mixing with matter waves and opens a way for experiments in nonlinear atomic optics [75, 76]. Our sequences to realize a novel atomic interferometer based on $F = 1$ sodium spinor BECs in the limit of long evolution times with seeded initial states will be introduced in Sec. 6.5.

6.3 Laser Cooling and Trapping

The observation and manipulation of an atomic BEC requires cooling an atomic gas to ultracold temperatures. In addition, an ultra-high vacuum environment is needed to reduce losses due to background gas collisions and increase the lifetime of a BEC. This is a technically demanding task, and it was not accessible until the idea of laser cooling was proposed [77] and demonstrated [78] in the 1970s. In the 1980s, laser cooling and trapping experienced a quick development, including the realizations of the Zeeman slower [79], optical molasses [80] and magneto-optical trap [81], making it possible to further cool down atoms close to critical temperatures of creating a BEC. In this section, I will review the cooling and trapping techniques we use when creating our BEC, including Doppler cooling, magneto-optical trap, far-off resonance dipole trap and evaporative cooling.

6.3.1 Doppler Cooling

Slowing down an atomic beam is the first step to allow capturing and cooling the atoms further. The idea of laser cooling is to use the transfer of momentum when an atom absorbs a photon. Fig. 6.4 shows the basic process of the light scattering force exerted on an atom. For a two-level system, if the laser frequency is close to the atomic resonance, the absorption of a photon causes the atom to transition to the excited state. Absorption also results in a momentum transfer between an atom and a photon, as illustrated in Fig. 6.4a. An atom in the excited state will return to the ground state by spontaneous emission. The emissions also have momentum kicks associated with them, but in random directions, so their contributions to the atom's momentum average to zero. The spontaneous emission is equivalent to a heating process, and will be discussed later.

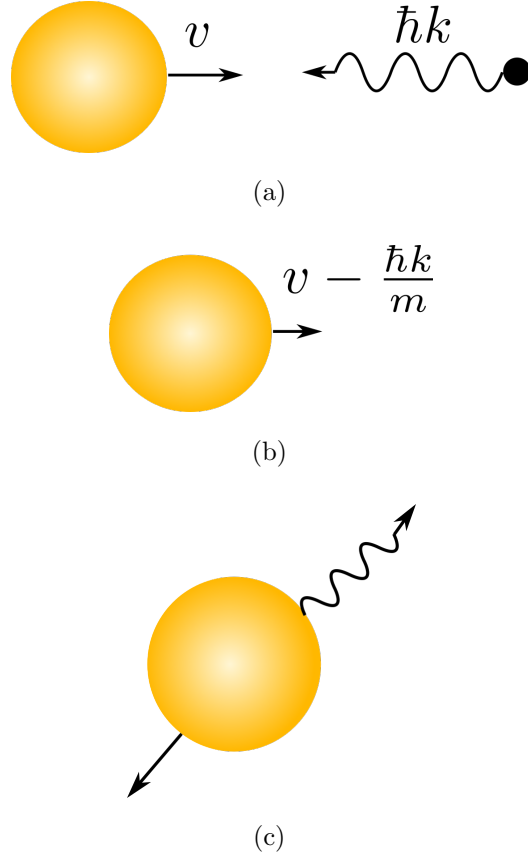


Figure 6.4: Cartoon of scattering force: (a) an atom encounters a resonant photon with momentum $\hbar k = \hbar/\lambda$; (b) the atom absorbs the photon, and is slowed by $\hbar k/m$; (c) the atom re-radiates a photon in a random direction. During many cycles, the average momentum change by this radiation is zero, so on average the atom slows down.

The radiation pressure force for a plane wave with wave vector \mathbf{k} is

$$\mathbf{F} = d\mathbf{p}/dt = \hbar\mathbf{k}\gamma_a, \quad (6.13)$$

where \mathbf{p} is the momentum of a photon, and γ_a is the absorption rate, which can be expressed as [82]

$$\gamma_a = \frac{s_0\Gamma/2}{1 + s_0 + (\frac{\delta + \omega_D}{\Gamma/2})^2}. \quad (6.14)$$

Here $s_0 = I/I_{\text{sat}}$ is the saturation parameter, Γ is the natural linewidth of the atomic transition, $\omega_D = -\mathbf{k} \cdot \mathbf{v}$ is the Doppler shift, and δ is the detuning of the laser frequency

from the atomic resonance.

In order to slow down atoms, the radiation force exerted on the atoms has to be always opposite to the direction of motion of the atoms and act like a friction force. Consider a pair of counter-propagating laser beams irradiating an atom with their frequencies detuned below the atomic resonance (red-detuned). Because of the Doppler shift, atoms moving towards either laser beam will see an upward shift in frequency and thus will be more likely to absorb photons from this head-on beam since the frequency of this beam is closer to the resonance. On the other hand, because the atom is moving away from the other beam, there will be a downward frequency shift and thus it is less likely to absorb the photons since it is further from resonance. As a result, the atom absorbs more photons from the laser beam opposite to its traveling direction, and therefore experiences a force in the opposite direction that only slows it down and never speeds it up.

Using Eq. (6.13), the total force from the two counter-propagating laser beams can be described as

$$\mathbf{F}_{\text{total}} = \mathbf{F}_+ + \mathbf{F}_- = \frac{\hbar\mathbf{k}\Gamma s_0}{2} \frac{1}{1 + s_0 + (\frac{\delta - kv}{\Gamma/2})^2} - \frac{\hbar\mathbf{k}\Gamma s_0}{2} \frac{1}{1 + s_0 + (\frac{\delta + kv}{\Gamma/2})^2}. \quad (6.15)$$

In the low velocity limit, terms in v^2 or higher can be neglected and Eq. (6.15) can be simplified as

$$\mathbf{F}_{\text{total}} \approx \frac{8\hbar k^2 \delta s_0 \Gamma}{(1 + s_0 + (2\delta/\Gamma)^2)^2} \mathbf{v} = -\alpha \mathbf{v}. \quad (6.16)$$

This force is linear in the atomic velocity, and it's a friction force, opposite to the direction of \mathbf{v} when $\alpha > 0$, that is, for $\delta < 0$ (red-detuned). The laser cooling technique takes advantage of the Doppler shift to apply a friction force to slow down atoms. Therefore, it is also called Doppler cooling. This cooling configuration can be generalized to three dimension by using a pair of counter-propagating red-detuned laser beams along each of the \mathbf{e}_x , \mathbf{e}_y , \mathbf{e}_z directions in space.

As we know from above, in the Doppler cooling process, atoms continuously absorb and radiate photons. The absorption process slows down atoms while the spontaneous emission process causes diffusion that heats the atoms. As a result, the cooling and heating process reach equilibrium at a certain temperature, known as the Doppler cooling temperature [47]

$$k_B T = \frac{\hbar\Gamma}{4} \left(\frac{\Gamma}{2\delta} + \frac{2\delta}{\Gamma} \right), \quad (6.17)$$

where δ is the laser detuning from the atomic resonance. The temperature has a minimum for $\delta = -\Gamma/2$, this minimum value is called Doppler limit, reads as

$$T_D = \frac{\hbar\Gamma}{2k_B}. \quad (6.18)$$

This temperature is about 240 μK for sodium, and 140 μK for rubidium.

6.3.2 Magneto-Optical Trap

As described above, laser cooling is a powerful tool to cool atoms. However, Eq. (6.16) shows that the radiative force depends on the velocity but not on position. So atoms are only cooled but not trapped, and may leave the laser beams and get lost. In order to confine the atoms within the cooling volume, a spatially dependent radiative force is required. A position-dependent force is created by applying a pair of quadrupole magnetic fields and appropriately polarized laser beams. Such a configuration is called magneto-optical trap (MOT). Since it was invented in 1987 [81], various types of MOT have been developed, such as a two-dimensional MOT [83], a surface MOT [84], and a pyramid MOT [85, 86]. In our lab, we use a three-dimensional (3D) MOT.

For simplicity, we explain the operation of a MOT in one dimension and for the case of an $F = 0$ to $F = 1$ transition. Consider a two-level system, with atomic transition from $F = 0 \rightarrow F' = 1$ in the presence of an external magnetic field gradient which is zero at trap center ($z = 0$), as shown in Fig. 6.5. The magnetic field is directed along the cooling laser beams (along z direction) and defines the

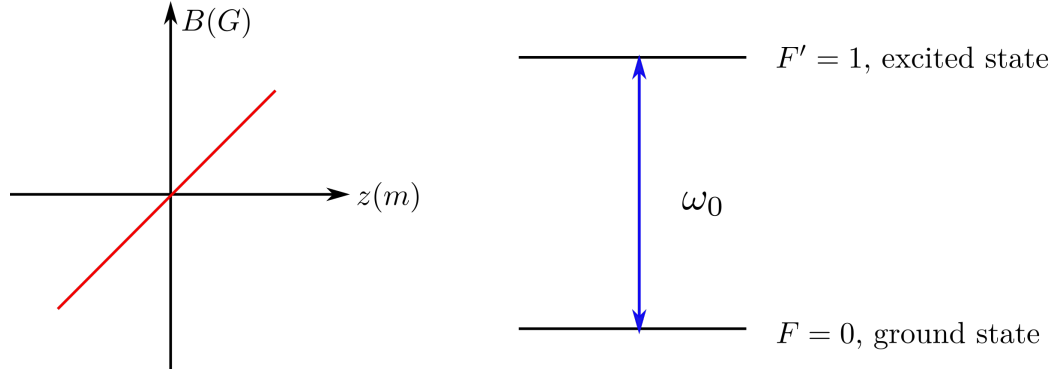


Figure 6.5: Schematic of magnetic field gradient along z direction, and two-level energy diagram.

quantization axis. The excited state has three magnetic sublevels $|F = 1, m_F = -1\rangle$, $|F = 1, m_F = 0\rangle$ and $|F = 1, m_F = +1\rangle$ in the presence of magnetic field, due to the Zeeman effect. Fig. 6.6 illustrates the operation of a MOT in one dimension. Two counter-propagating laser beams with opposite circular polarizations (σ_+ and σ_-) are red-detuned ($\delta < 0$). The σ_- polarization beam only drives the $\Delta m = -1$ transition while the σ_+ polarization beam only drives the $\Delta m = +1$ transition according to the selection rules. With a constant magnetic field gradient along the z direction, the substate of $|F' = 1, m_F = +1\rangle$ is shifted down for $B < 0$, while $|F = 1, m_F = -1\rangle$ is shifted up. In the region of $z < 0$, the $|F = 1, m_F = +1\rangle$ state is shifted down and the $\Delta m = +1$ transition is closer to the resonance. Atoms in the $z < 0$ region are therefore more likely to absorb σ_+ photons and feel a force toward the positive z direction. Conversely, for atoms in the $z > 0$ region there is a higher possibility to absorb σ_- photons and produce a net force toward the negative z direction. As a result, atoms displaced from the center will be pushed towards the center. Meanwhile, the laser beams are still red-detuned so that Doppler cooling is also happening. Compression and cooling is simultaneously obtained in a MOT. With three pairs of counter-propagating orthogonal laser beams as cooling light, and a pair of anti-Helmholtz coils providing

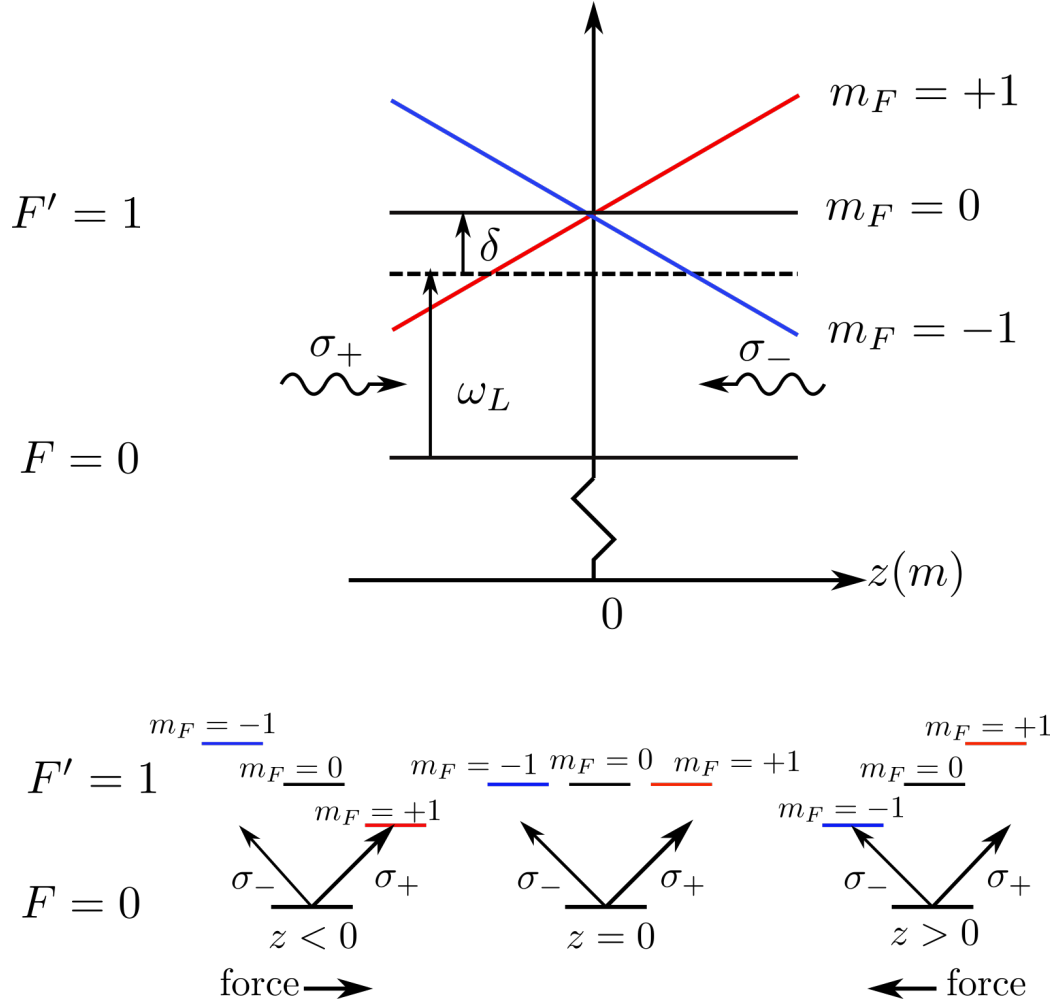


Figure 6.6: Schematic of one-dimensional MOT. A magnetic field gradient that has a value of zero at the trap center shifts excited state energy levels up or down depending on the position of the atoms. Counter-propagating laser beams with opposite circular polarizations are red-detuned. The selection rule for transitions between substates due to the Zeeman shift leads to an imbalanced radiative force. The force depends on position in such a way that it pushes atoms towards the center of the trap ($z = 0$).

the required magnetic field gradient, a 3D MOT is realized, as illustrated in Fig. 6.7.

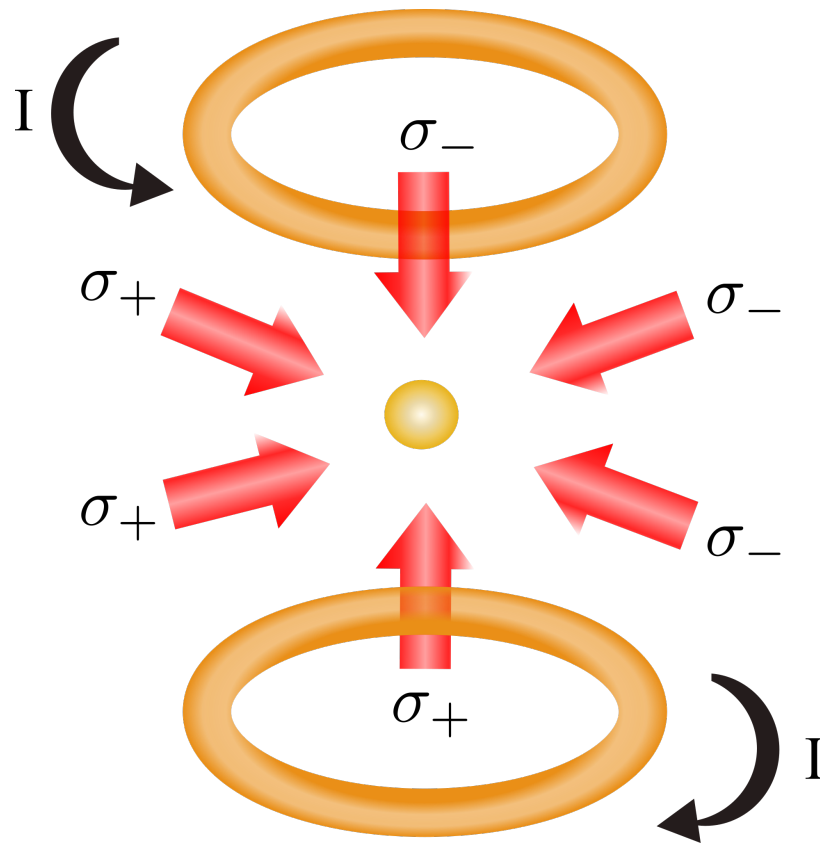


Figure 6.7: Schematic of the MOT. Three pairs of circularly polarized laser beams come from three orthogonal directions. Two anti-Helmholtz coils provide an inhomogeneous magnetic field gradient.

6.3.3 Optical Dipole Trap and Evaporative Cooling

Apart from the MOT mentioned in Sec. 6.3.2, which represents a radiation-pressure trap, there are other traps based on different interactions, such as the magnetic trap [87] and the optical dipole trap (ODT) [88]. For the magnetic trap, the trapping mechanism relies on the magnetic dipole moment of the internal atomic state, so only one spin state can be trapped, limiting its use to scalar BEC experiments. The optical dipole trap is based on the electric dipole interaction with a far-detuned light field. The interaction is independent of the atomic sublevels, so all spin states can be trapped simultaneously, allowing experiments with spinor BECs. Moreover, an optical dipole trap has a lower trapping depth, usually below mK, compared to a MOT which has a typical trapping depth of a few K. Therefore, for our experiment's purpose, an optical dipole trap is used to further trap and cool the atoms after the MOT.

When an atom is placed into laser light, an atomic dipole moment \mathbf{p} is induced by the electric field \mathbf{E} of the light and oscillates at the driving frequency ω . Two main quantities of interest for dipole traps are the trap potential U_{dip} resulting from the induced dipole moment \mathbf{p} interacting with the driving field \mathbf{E} , and the scattering rate Γ_{sc} which induces heating. The expressions for U_{dip} and Γ_{sc} are derived in Ref. [88]:

$$U_{\text{dip}}(\mathbf{r}) = \frac{3\pi c^2}{2\omega_0^3} \frac{\Gamma}{\Delta} I(\mathbf{r}), \quad (6.19)$$

$$\Gamma_{\text{sc}}(\mathbf{r}) = \frac{3\pi c^2}{2\hbar\omega_0^3} \left(\frac{\Gamma}{\Delta}\right)^2 I(\mathbf{r}). \quad (6.20)$$

Here ω_0 is the atomic resonance, Γ is the decay rate of the excited state ($2\pi \times 9.8$ MHz for sodium atoms), and $I(\mathbf{r})$ is the laser beam intensity. $\Delta = \omega - \omega_0$ is defined as the laser frequency detuning.

The expressions of U_{dip} and Γ_{sc} show two essential properties of the optical dipole trap. First, the sign of the potential is determined by the sign of the detuning Δ . For a red-detuned ($\Delta < 0$) trap, the potential is negative and the trap attracts atoms

towards higher laser intensities. On the other hand, a blue-detuned ($\Delta > 0$) trap potential is positive and thus repels atoms from its higher intensities. Second, U_{dip} scales with I/Δ while Γ_{sc} scales with I/Δ^2 . As a result, a far-detuned (large Δ) and high-intensity laser beam for a dipole trap to provide a tight confinement while also reduce the scattering rate is desirable to minimize any heating due to scattering. A simple dipole trap for cold atoms could be generated by a far-detuned ($\Delta < 0$), tightly-focused Gaussian laser beam. This ODT offers tight confinement in the radial direction while it has a weaker confinement in the axial direction. By using two crossed laser beams, an optical dipole trap with tight confinement in all directions is achieved.

Evaporative cooling is usually the last step to achieve a BEC. It can be performed by slowly lowering the dipole trap potential U_{dip} over several seconds, i.e., lowering the dipole trap laser intensity I . Similar to cooling a cup of coffee, lowering the dipole trap potential allows energetic atoms to escape from the trap. The rest of the atoms at lower energies remain in the trap and rethermalize. The average temperature of the atomic cloud is decreased in this way. As we continuously lower the dipole trap potential, the atomic cloud temperature finally reaches the critical temperature and a BEC is achieved [89].

6.4 Microwave Dressing

Eq. (6.11) shows that the quadratic Zeeman energy is due to the applied magnetic field, but it can also effectively be obtained by other methods, for example, a microwave dressing field [90, 62, 91]. In contrast to a magnetic field induced quadratic Zeeman energy which can only be positive, a microwave dressing field gives the ability to shift towards positive or negative effective quadratic Zeeman energy. It provides access to both positive and negative values of the effective quadratic Zeeman shift q .

The $F = 1$ and $F = 2$ of sodium ground state split into sublevels in the presence

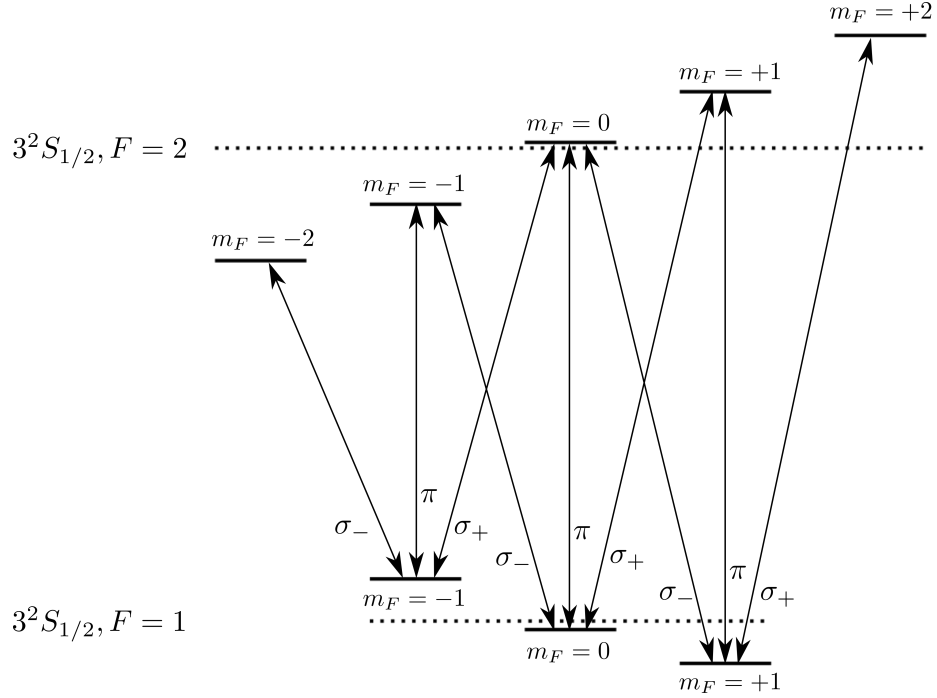


Figure 6.8: Hyperfine structure of sodium ground state manifold in the presence of a constant external magnetic field. Lines with arrows represent the nine allowed transitions between $F = 1$ and $F = 2$ states due to the selection rules. The corresponding polarizations are also labeled. The dashed lines are the degenerate energy levels without Zeeman shift. The resonant frequency between $F = 1$ and $F = 2$ is around 1.7 GHz.

of a constant magnetic field, as shown in Fig. 6.8. There are nine possible transitions between $F = 1$ and $F = 2$ states, according to the selection rules. When a microwave field at a frequency near resonance is applied in the case of Na at frequencies around 1.77 GHz, the energy of these states are shifted. The shift results from the microwave induced AC Zeeman effect. To prevent atoms from populating to $F = 2$ states, the microwave field is detuned from all transition resonances. One important point is that by applying a microwave field that is detuned with respect to each transition, the energy shifts will be spin-dependent. So we can control the energy shift of each state this way.

The calculation of the microwave induced energy shift is derived in Ref. [90] and

Ref. [91]. Here we express the value as

$$\Delta E_{m_F} \approx \frac{\hbar \Omega_\pi^2}{4\Delta} f_{m_F} \left(\frac{\mu_B B}{\hbar \Delta} \right), \quad (6.21)$$

where Δ denotes the microwave field detuning from the $|F = 1, m_F = 0\rangle \leftrightarrow |F = 2, m_F = 0\rangle$ clock transition, Ω_π is the Rabi frequency of the π -polarized transition, and μ_B is the Bohr magneton. Function $f_{m_F}(x)$ accounts for different microwave polarizations and the multiple transitions. $f_{m_F}(x)$ is defined as

$$f_{m_F}(x) = \sum_{k=0,\pm 1} \frac{3C_{m_F,k} I_k}{4} \frac{1}{I_\pi 1 - (m_F + \frac{k}{2})x}, \quad (6.22)$$

here $C_{m_F,k} = |\langle F = 1, m_F; 1, k | F = 2, m_F + k \rangle|^2$ are the square module of the Clebsch-Gordan coefficients, and I_k is the intensity of the k -polarized microwave component. The total effective quadratic Zeeman shift q consists of two terms: the DC magnetic field induced quadratic Zeeman shift q_B and the microwave field induced quadratic Zeeman shift q_μ . So q can be expressed as

$$\begin{aligned} q &= q_B + q_\mu \\ &= \gamma B^2 + \frac{\Delta E_{m_F=+1} + \Delta E_{m_F=-1} - 2\Delta E_{m_F=0}}{2}, \end{aligned} \quad (6.23)$$

where $\gamma \approx 277 \text{ Hz/G}^2$ for Na atoms. In experiments, we choose the microwave field detuning Δ to be far from the $|F = 1, m_F = 0\rangle \leftrightarrow |F = 2, m_F = 0\rangle$ transition to avoid populating the $|F = 2, m_F = 0\rangle$ state. We also apply a DC magnetic field that sufficiently separates different m_F levels to avoid other resonances. For example, we sometimes choose $\Delta = 2\pi \times 50 \text{ kHz}$ and a linear Zeeman shift $E_{\text{linear}} = -g_J \mu_B m_F B_0 = 2\pi \times 300 \text{ kHz}$. Under these conditions, the energy shifts of $|F = 1, m_F = \pm 1\rangle$ states due to microwave dressing are negligible compared to the $|F = 1, m_F = 0\rangle$ state. Also, the coupling to $|F = 2, m_F = \pm 1\rangle$ states is suppressed. Under this approximation, the microwave induced quadratic Zeeman shift can be simplified as

$$q_\mu = -\frac{\hbar \Omega^2}{4 \Delta}, \quad (6.24)$$

where Ω is the Rabi frequency on resonance, and Δ is the microwave frequency detuning.

6.5 Interferometry Sequence

As introduced in previous sections, we cool and trap Na atoms via the MOT technique, and then further cool the gas by evaporative cooling in an optical dipole trap down to the critical temperature to form a BEC. Spin-exchange collisions can be initialized via quenching in our $F = 1$ spinor BEC, causing atomic population transfer between $m_F = 0$ and $m_F = \pm 1$ states and creation of quantum entanglement. A microwave dressing field is used to tune the effective quadratic Zeeman shift q and thus control the spin evolution. With these tools, we realize an atomic interferometer with spinor BECs.

We realize a spin-mixing interferometer sequence in four steps, similar to recent experiments and theoretical proposals [74, 92], but in our case in the long evolution time limit and with seeded initial states, as shown in Fig. 6.9. The first step is state preparation. Initially, we prepare N atoms with certain classical seeds in the $m_F = +1$ and/or the $m_F = -1$ state by using microwave or rf pulses, as shown in Fig. 6.10. The second step is labeled “split”, during which a specific effective quadratic Zeeman energy q is applied via an appropriate microwave-dressing field and the system is allowed to evolve for time τ , after which there is a certain number of atoms $N_{\text{inside}} = N_{+1} + N_{-1}$ in the $m_F = \pm 1$ states. Thirdly, at time τ , we apply a detuned microwave-dressing pulse with short duration, $t_{\text{rev}} \ll \frac{\hbar}{c}$, and large amplitude, $q_{\text{rev}} \gg c$, $q_{\text{rev}} \gg q$, to shift the $m_F = 0$ state and add a phase shift $\varphi \approx 2q_{\text{rev}}t_{\text{rev}}$ to the spinor phase θ . After turning off the short microwave pulse that added a phase shift, we let the system evolve for another time τ , this is labeled “recombine” process because some of the atoms in $m_F = \pm 1$ state may oscillate back to the $m_F = 0$ state. Finally, we evaluate

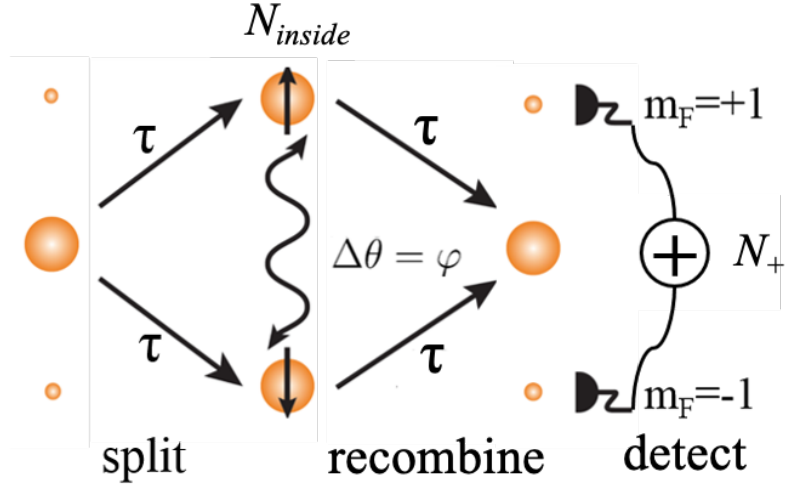
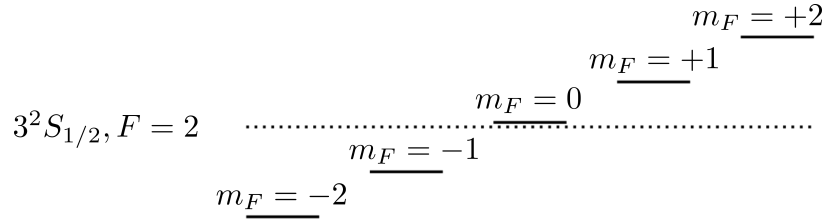


Figure 6.9: Spin-mixing interferometry sequence in a $F = 1$ spinor BEC. The first step is to prepare the initial state, with most of the atoms in $m_F = 0$ state and some initial seeds in $m_F = \pm 1$ states. The second step, “split”, is to quench to a specific q and let the system evolve. The third step is to apply a quick phase shift φ at time τ and let the system evolve for another time interval τ . The last step is to detect the total number of atoms in $m_F = +1$ and $m_F = -1$ state.

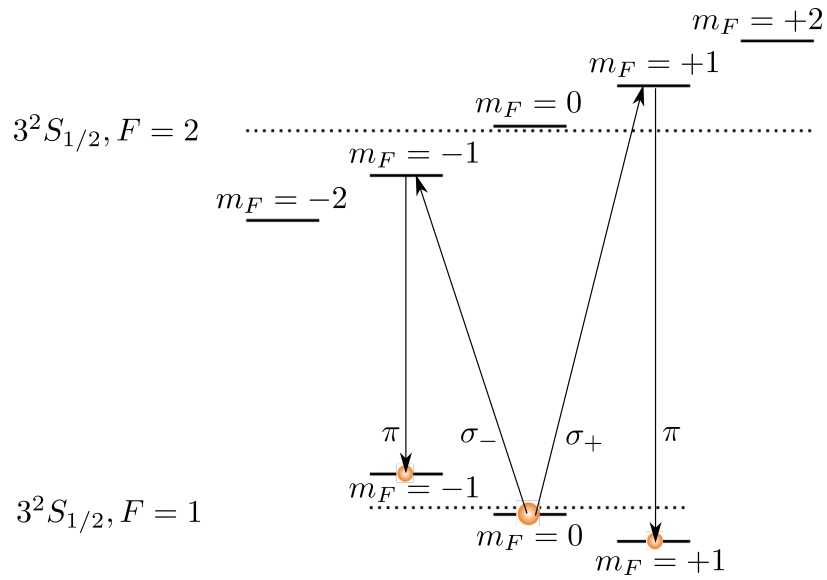
the final number of atoms in the $m_F = \pm 1$ states, $N_+ = N_{+1} + N_{-1}$, with mean $\langle N_+ \rangle$ and standard deviation σ_{N_+} at time $t = \tau + t_{\text{rev}} + \tau$. Detection can be done via Stern-Gerlach separation followed by time-of-flight absorption imaging.

To characterize the phase sensitivity of such an interferometer, we analyze $\langle N_+ \rangle$ and σ_{N_+} as a function of φ to find regions that maximize the sensitivity. φ is changed by adjusting q_{rev} and t_{rev} within realistic ranges of $q_{\text{rev}}/h = -2,000 \dots 0$ Hz and $t_{\text{rev}} = 0 \dots 1$ ms that are accessible by experiments. The interferometry phase sensitivity is given by $(\Delta\varphi)^2 = \frac{(\sigma_{N_+})^2}{|d\langle N_+ \rangle/d\varphi|^2}$ from error propagation [74]. Using this definition, lower sensitivity $(\Delta\varphi)^2$ means better signal-to-noise ratio and thus better performance. The standard quantum limit (SQL) to be compared to $(\Delta\varphi)^2$ is defined as $SQL = 1/\langle N_{\text{inside}} \rangle$. We use this SQL definition from Ref. [74] to compare the

performance of our interferometer with initial seeds and long time evolution, with the standard interferometer in Ref. [74]. Both sensitivity $(\Delta\varphi)^2$ and the SQL are determined by measuring the mean total population $\langle N_+ \rangle$ in the $m_F = \pm 1$ states and its standard deviation σ_{N_+} at the end of the sequence. In the next chapter the outlined interferometry sequence is analyzed in detail numerically.



(a) rf seeding



(b) microwave seeding

Figure 6.10: Seeding atoms via rf or microwave pulses. (a) Seeding atoms from the $m_F = 0$ state to the $m_F = \pm 1$ states using a resonant rf pulse. An rf pulse can seed equal number of atoms into $m_F = \pm 1$ states. (b) Seeding atoms from the $m_F = 0$ state to the $m_F = \pm 1$ states using resonant microwave pulses via intermediate states. Microwave pulses can seed $m_F = \pm 1$ states individually.

Chapter 7

Quantum Interferometry with Microwave-Dressed $F=1$ Spinor Bose-Einstein Condensates: Role of Initial States and Long Time Evolution

In this chapter, we numerically investigate atomic interferometry based on spin-exchange collisions in $F = 1$ spinor Bose-Einstein condensates in the regime of long evolution times $t \gg h/c$, where c is the spin-dependent interaction energy. We show that the sensitivity of spin-mixing interferometry can be enhanced by using classically seeded initial states with a small population prepared in the $m_F = \pm 1$ states.

This chapter was published as Ref. [93], where I was the first author. The content of the publication was slightly adapted to the context of this thesis.

7.1 Introduction

In a spinor Bose-Einstein condensate (BEC), the atomic hyperfine spin degree of freedom becomes accessible and displays fascinating quantum dynamics driven by collisions that can be controlled via external fields. Spin-exchange collisions in $F = 1$ microwave-dressed spinor BECs, where two atoms in $m_F = 0$ Zeeman substate collide with each other and change into a pair of entangled atoms in $m_F = \pm 1$ states, create a rich dynamical system with analogies to four-wave mixing in atomic vapors [11], the bosonic Josephson effect [94], the quantum non-rigid pendulum [95], and with quantum phase transitions that can lead to creation of massive entanglement [5]. The spin-exchange collisions conserve total spin and magnetization [32]. The collisions cause characteristic population oscillations between the $m_F = 0$ and the $m_F = \pm 1$ states [96, 97, 98] and can generate squeezing [99, 100, 76]. Surprising phenomena that have been observed in spinor BECs driven by spin-exchange include spin textures and

spin waves in elongated spinor BECs [101, 102], spin dynamics in lattices [103, 104] and spin-nematic squeezing [68].

It was demonstrated that spin dynamics can be precisely controlled using microwave dressing [91] and, recently, a phase-sensitive amplifier was implemented using this control [51]. This opens up the field of matter-wave quantum optics in spin space. In particular, quantum interferometry with sensitivities beyond the standard quantum limit (SQL), based on spin-exchange collisions, is possible. So far, experiments on quantum interferometry in this system started with all atoms in $m_F = 0$ and allowed only a few atoms to populate the arms of the interferometer during the evolution [74]. Here, we are interested in quantum interferometry starting with initial states where some atoms are seeded in $m_F = \pm 1$. In addition, we investigate the effect of long evolution times with more than a few atoms in the arms of the interferometer, beyond the regimes of validity of the Bogoliubov, truncated Wigner, and undepleted pump approximations. Long evolution times can be sustained in practice because of the long coherence time of spin dynamics in Bose-Einstein condensates, which has been demonstrated experimentally to be on the order of seconds in one setup and to be larger than 80 ms in another setup [105, 106]. These coherence times are sufficient to reach the long evolution time limit, because they allow for several oscillation periods and large evolved populations. The experiments proposed here could be performed in such setups.

The investigations in this chapter focus on numerical simulations of the collisional evolution of spin populations in a $F = 1$ sodium BEC. We simulate a nonlinear spin-exchange based interferometer that measures the relative phase between $m_F = 0$ and $m_F = \pm 1$ pairs. The phase measurement exhibits uncertainties that improve upon the SQL. We focus on quantum-enhanced interferometry where there are macroscopic numbers of atoms in the arms of the interferometer. This is desirable compared to

small populations, because it makes detection easier in experiments. This regime can be realized via long evolution times where many collisions are allowed to take place, and via populating the $m_F = \pm 1$ states initially, which can speed up the evolution. We show that there are parameter regimes in which such an interferometer can surpass the SQL. Here we use the SQL definition from Ref. [74]. In our system, a different definition of SQL could be applied due to the nonlinear nature of the phase measurement. The interferometer fringes become highly non-sinusoidal, owing to the nonlinear measurement.

7.2 Computational Method

We consider small F=1 BECs where the Thomas-Fermi radius is smaller than the spin healing length, $\xi_s = 2\pi\hbar/\sqrt{2m|c_2|\bar{n}}$ and spin domain formation is therefore energetically suppressed. Here, $c_2 = 4\pi\hbar^2(a_2 - a_0)/3m$, with a_0 and a_2 the scattering lengths for the two allowed collision channels of total spin 0 and 2 [66], m is the atomic mass, and \bar{n} is the mean number density [107]. We assume further that the spin-dependent interaction is much weaker than the density-dependent interaction. This allows us to make the single-spatial-mode approximation (SMA), which assumes that all spin components share the same spatial wavefunction [108, 107]. Numerically, the SMA was shown to be valid for atom numbers up to 1×10^4 in small spherical harmonic traps and long evolution times up to ~ 400 ms [97]. Experimentally, the SMA was shown to be valid for 4×10^4 atoms in small sodium spinor BECs [91, 51] and in a small rubidium spinor BEC [105]. In the latter experiment, long evolution times of several seconds were investigated and agreed well with the SMA predictions. To ensure the validity of the SMA in experiments, a breakdown of which can be seen as spatial structure in the images [109], the atom number can be reduced or the trap frequency can be changed. Under the SMA, the evolution is governed only by the spin

part of the Hamiltonian, H_s . In the presence of microwave-dressing and an applied magnetic field [110],

$$\hat{H}_s = \frac{c}{2N} \hat{\mathbf{F}}^2 - q \hat{a}_0^\dagger \hat{a}_0, \quad (7.1)$$

where $\hat{\mathbf{F}} = a_\alpha^\dagger \mathbf{F}_{\alpha\beta} a_\beta$ is the total spin operator, and $\mathbf{F}_{\alpha\beta}$ are spin-1 matrices. Here, $c = c_2 \bar{n}$ is the spin-dependent interaction parameter. In a typical small sodium spinor BEC in a crossed far-off resonance trap with geometric mean trap frequency of 200 Hz and $N \approx 25,000$, we have $c/h \approx 30$ Hz [111]. q is the effective quadratic Zeeman shift, $q/h \approx \gamma B^2 - \frac{\Omega^2}{\Delta_\mu}$, where γB^2 is the quadratic Zeeman shift due to the applied magnetic field B , and $\gamma \approx 277$ Hz/G² for sodium [110], Ω is the microwave Rabi frequency on resonance, and Δ_μ is the detuning from the $|F = 1, m_F = 0\rangle \rightarrow |F = 2, m_F = 0\rangle$ transition. Here, we assumed that $\Delta_\mu \gg \gamma$. q can be used to control the spin dynamics via the magnetic field or the microwave dressing. We simulate the evolution according to \hat{H}_s using two numerical methods: the full quantum evolution and the truncated Wigner approximation. These two methods are contrasted in the following sections.

7.2.1 Full Quantum Evolution

The full quantum method consists of calculating the time evolution propagator $e^{-i\hat{H}_s t}$ of the system in the basis of Fock states $|N_{-1}, N_0, N_{+1}\rangle$, where N_i is the occupation number of the i -th magnetic sublevel. We use the Chebyshev propagator to solve this quantum mechanical time evolution numerically on a supercomputer. Compared to other methods, such as the second-order difference (SOD) method [112] and the short-iterative Lanczos (SIL) method [113], the Chebyshev propagator is more accurate and efficient, and requires much less memory and CPU time [114]. For Hermitian Hamiltonians [114],

$$e^{-i\hat{H}t} = \sum_{k=0}^{\infty} (2 - \delta_{k0}) (-i)^k J_k(t) T_k(\hat{H}), \quad (7.2)$$

where J_k are Bessel functions of the first kind, $T_k(\hat{H})$ are Chebyshev polynomials, and \hat{H} is the Hamiltonian scaled to $[-1,1]$. The Chebyshev propagator can be calculated recursively and precisely because it consists of polynomials of \hat{H} that obey simple recursion relations, compared to evolution via the exponential function which is harder to compute directly. The recursion relations we use are [114]

$$T_{k+1}(\omega) = 2\omega T_k(\omega) - T_{k-1}(\omega), \text{ for } k \geq 1, \quad (7.3)$$

with

$$T_0(\omega) = 1, \quad T_1(\omega) = \omega. \quad (7.4)$$

This method can be used for arbitrary initial state, and we focus on two kinds of initial states: pure Fock states $|N_{-1}, N_0, N_{+1}\rangle$ with fixed number of atoms in each state and spin coherent states $|\alpha_{-1}, \alpha_0, \alpha_{+1}\rangle = \sum_{N_{-1}, N_0, N_{+1}=0}^N \sqrt{\frac{N!}{N_{-1}!N_0!N_{+1}!}} \alpha_{-1}^{N_{-1}} \alpha_0^{N_0} \alpha_{+1}^{N_{+1}} |N_{-1}, N_0, N_{+1}\rangle$, where $\alpha_i = \sqrt{\langle N_i \rangle} e^{i\langle \theta_i \rangle}$ with mean population $\langle N_i \rangle$ and phase $\langle \theta_i \rangle$. The magnetization $M = N_{+1} - N_{-1}$ is fixed in a Fock state but ranges from $-N$ to $+N$ in a spin coherent state. The total atom number $N = N_{-1} + N_0 + N_{+1}$ is conserved in both cases, and constrains the sum for the coherent states. Due to conservation of total atom number $N = N_{-1} + N_0 + N_{+1}$ and magnetization $M = N_{+1} - N_{-1}$, the Fock basis $|N_{-1}, N_0, N_{+1}\rangle$ can also be expressed as $|\frac{1}{2}(N - N_0 - M), N_0, \frac{1}{2}(N - N_0 + M)\rangle$. The computation for a Fock initial state is much faster than that for a coherent initial state, because of the limited subspace of allowed occupation numbers.

7.2.2 Truncated Wigner Approximation (TWA)

In some calculations, we use a semi-classical approach based on the truncated Wigner and mean-field approximations to approximate the full quantum spinor dynamics. In this method, the interactions between each atom and all other atoms during spin

collisions are treated as an average interaction. The Hamiltonian is thus simplified as

$$\hat{H}_s^{\text{TWA}} = \hbar c(\langle \hat{F}_x \rangle \hat{F}_x + i\langle \hat{F}_y \rangle \hat{F}_y + \langle \hat{F}_z \rangle \hat{F}_z) + \hbar q \hat{F}_z^2, \quad (7.5)$$

Here, \hat{F}_α are spin-1 matrices in the basis $|F, m_F\rangle$. We set the initial state to approximate a three-mode coherent spin state with standard deviations of $\sigma_{N_i} = \sqrt{\frac{1}{4} + \langle N_i \rangle}$, as

$$\Psi = \Psi_0 + \delta \frac{1}{2\sqrt{N}}, \quad (7.6)$$

where

$$\Psi_0 = \begin{pmatrix} \psi_{-1} \\ \psi_0 \\ \psi_{+1} \end{pmatrix} = \begin{pmatrix} \sqrt{\frac{\langle N_{-1} \rangle}{N}} e^{i\langle \theta_{-1} \rangle} \\ \sqrt{\frac{\langle N_0 \rangle}{N}} e^{i\langle \theta_0 \rangle} \\ \sqrt{\frac{\langle N_{+1} \rangle}{N}} e^{i\langle \theta_{+1} \rangle} \end{pmatrix}, \quad (7.7)$$

and

$$\delta = \begin{pmatrix} a + ib \\ c + id \\ f + ig \end{pmatrix}, \quad (7.8)$$

where a, b, c, d, f and g are real random numbers, drawn independently from a normal distribution with zero mean and a standard deviation of 1. $\langle \theta_i \rangle$ are the mean phases, $\langle N_{+1} \rangle$, $\langle N_{-1} \rangle$ are the initial mean seed populations, N is the total atom number, and $\langle N_0 \rangle = N - \langle N_{+1} \rangle - \langle N_{-1} \rangle$ is the initial number of $m_F = 0$ atoms (before addition of noise). We define the spinor phase $\theta = \theta_{+1} + \theta_{-1} - 2\theta_0$. Setting the initial spinor phase in ψ_0 is accomplished by letting $\langle \theta_{+1} \rangle = \langle \theta_{-1} \rangle = 0$ so that $\langle \theta_0 \rangle = -\langle \theta \rangle / 2$. In all the simulations presented here, we set $\langle \theta_0 \rangle = 0$.

The evolution is then calculated by propagating the effective single particle wavefunction via $\Psi(t + dt) = \exp(-i\hat{H}_s^{\text{TWA}} dt)\Psi(t)$ and taking an ensemble average over many realizations. We found that the TWA works well for short and intermediate evolution times compared to h/c when starting with all atoms in $m_F = 0$. The TWA fails to predict correct standard deviations when starting with some seeded atoms in $m_F = \pm 1$ and when the evolution times become longer, $t \gg h/c$.

7.2.3 Interferometer

We realize a spin-mixing interferometer sequence in three steps, similar to recent experiments and theoretical proposals [74, 92], as shown in Fig. 7.1. Initially, we prepare N atoms with certain classical seeds in $m_F = +1$ and/or $m_F = -1$. In an experiment, the seeding can be done either via short resonant microwave pulses to transfer populations through an intermediate $F = 2$ state, or via resonant rf pulses that transfer atoms directly from $m_F = 0$ to $m_F = \pm 1$. Following the initial state preparation, we let the system evolve for time τ , after which there is a certain number of atoms $\langle N_{\text{inside}} \rangle = \langle N_{+1} \rangle + \langle N_{-1} \rangle$ in the $m_F = \pm 1$ states. At time τ , we apply a detuned microwave-dressing pulse with short duration, $t_{\text{rev}} \ll h/c$, and large amplitude, $q_{\text{rev}} \gg c$ and q . This pulse shifts the $m_F = 0$ state and adds a phase shift $\varphi \approx 2\pi \times 2q_{\text{rev}}t_{\text{rev}}$ to the spinor phase θ . We then let the system evolve for another time τ , and evaluate the final number of atoms in the $m_F = \pm 1$ states, $N_+ = N_{+1} + N_{-1}$, with mean value $\langle N_+ \rangle$ and standard deviation σ_{N_+} at time $t_f = \tau + t_{\text{rev}} + \tau$. In an experiment, detection can be done via Stern-Gerlach separation followed by time-of-flight absorption imaging. To characterize the phase sensitivity of such an interferometer, we analyze $\langle N_+ \rangle$ and σ_{N_+} as a function of φ to find regions with the best sensitivity. The phase sensitivity is given by $(\Delta\varphi)^2 = \frac{(\sigma_{N_+})^2}{|d\langle N_+ \rangle/d\varphi|^2}$ from error propagation [74]. The SQL to be compared to $(\Delta\varphi)^2$ is defined as $\text{SQL} = 1/\langle N_{\text{inside}} \rangle$ to compare with the results for a standard interferometer in Ref. [74], although a different definition could be applied due to the nonlinear measurement nature of our interferometer. Both sensitivity $(\Delta\varphi)^2$ and the SQL are determined by measuring the mean total population $\langle N_+ \rangle$ in the $m_F = \pm 1$ states and its standard deviation σ_{N_+} at the end of the sequence. Our simulation codes were verified with known experimental results by reproducing Fig. 2(b) of Ref. [74] and Fig. 1 of Ref. [97].

To investigate the role of the initial state and of long evolution times, we simulate

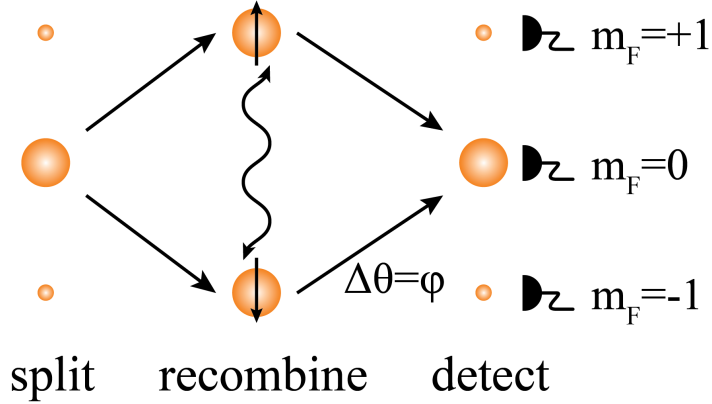


Figure 7.1: (Color online) Cartoon of the interferometer sequence with initial seeds. The phase shift $\varphi = \Delta\theta$ is applied via microwave dressing. The straight arrows denote time evolution. The wavy arrow denotes entanglement. The black detectors represent population measurements via Stern-Gerlach time-of-flight absorption imaging at the end of the sequence.

the interferometry sequence starting from coherent initial states or Fock initial states with different initial seeds and $t_f \gg h/c$. We use realistic parameters for a sodium BEC [66, 115] with $c/h = 30$ Hz, $q/h = -2$ Hz and -35 Hz, q_{rev}/h ranging between 0 Hz and $-2,000$ Hz and $t_{\text{rev}} = 0.25$ ms to achieve a phase shift of $\varphi = 0 \dots 2\pi$. The initial spinor phase is set to $\langle\theta\rangle = 0$. We choose different initial seeds to investigate the role of the initial state. An example of the effect of long evolution times is shown in Fig. 7.2. $\langle N_+ \rangle$ and σ_{N_+} vs. phase φ are sinusoidal only for short evolution times $\tau \ll h/c$ where $\langle N_{\text{inside}} \rangle \ll N$. At longer evolution times where $\langle N_{\text{inside}} \rangle$ is larger, $\langle N_+ \rangle$ and σ_{N_+} become highly non-sinusoidal. The non-sinusoidal dependence on phase can improve the interferometer sensitivity since $|d\langle N_+ \rangle/d\varphi|$ can be enhanced.

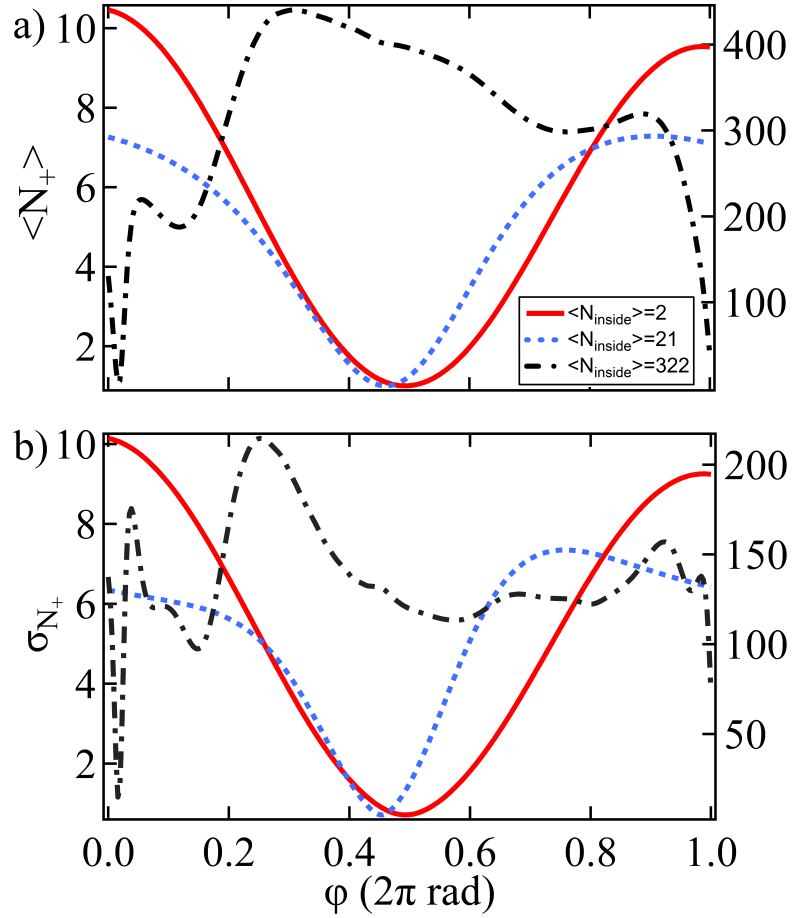


Figure 7.2: (Color online) Interferometer fringes for different evolution times. Shown is the phase dependence of (a) $\langle N_+ \rangle$ and (b) σ_{N_+} for $\langle N_{\text{inside}} \rangle = 2$ (red solid, left axis), 21 (blue dashed, left axis), 322 (black dash-dotted, right axis). Here, $c/h = 30$ Hz, $q/h = -35$ Hz, $N = 1,000$, and zero initial seed. For longer evolution times (larger $\langle N_{\text{inside}} \rangle$), interferometer fringes become highly non-sinusoidal.

7.3 Results

7.3.1 Comparison of TWA Evolution and Chebyshev Evolution

To determine the range of validity of the TWA method, we compare the results from the TWA method with the full quantum method. We find that the standard deviations σ_{N_+} predicted by the TWA method are only accurate for non-seeded evolutions. For seeded cases, they are only valid for short evolution times $t \ll h/c$, and then quickly diverge from the full quantum method. As shown in Fig. 7.3, the TWA method agrees well with the full quantum calculation for at least the first cycle of population oscillations in the unseeded case, see Fig. 7.3a. But as initial seeds are introduced into the system, the results from the TWA method no longer agree with the full quantum calculations, especially for the standard deviations σ_{N_+} , as seen in Fig. 7.3b and 7.3c. With initial seeds, the TWA method doesn't capture the quantum noise accurately anymore. Therefore, in this chapter, only the results for non-seeded evolutions were obtained using the TWA method, while all data for seeded evolutions were obtained using the full quantum method.

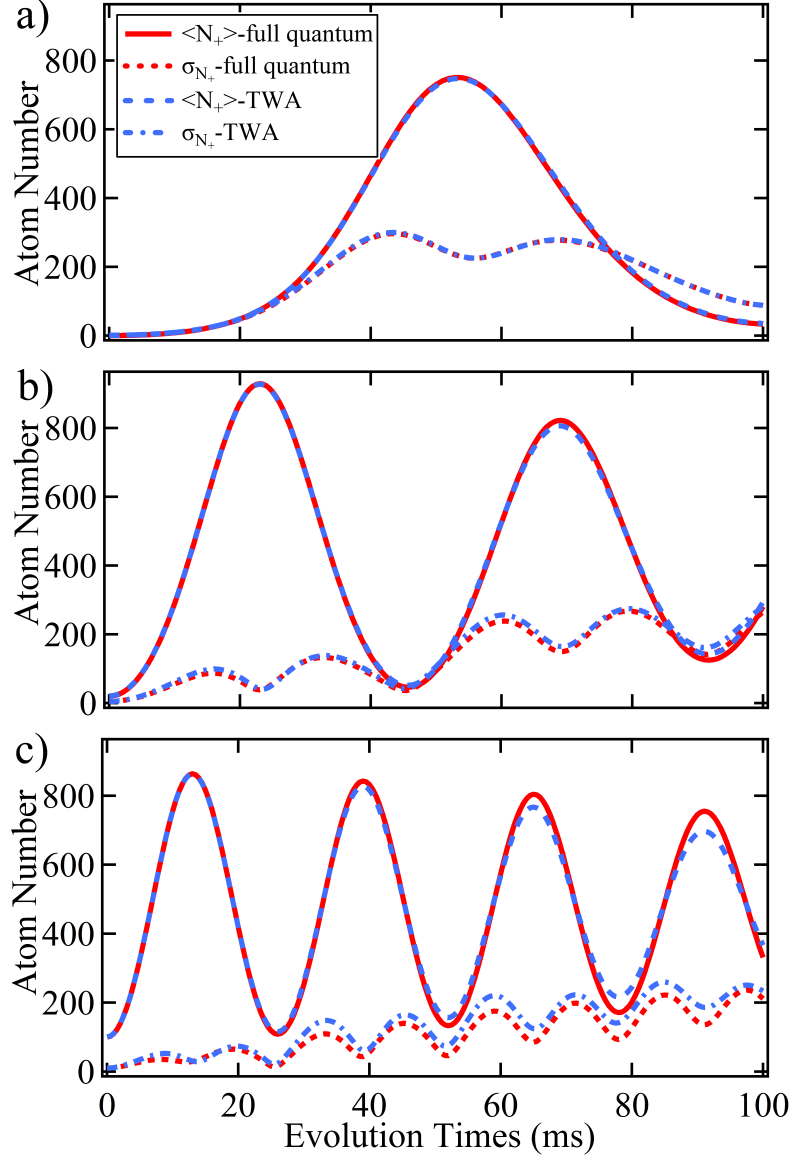


Figure 7.3: (Color online) Evolutions of $\langle N_+ \rangle$ for the full quantum method (red solid) and TWA method (blue dashed), and evolutions of σ_{N_+} for the full quantum method (red dotted) and TWA method (blue dash-dotted). Shown are evolutions for (a) 0%, (b) 2% , and (c) 10% initial seeds. Here, $N = 1,000$ and $q/h = -2$ Hz. For large initial seeds, the standard deviations predicted by the TWA method are in disagreement with the full quantum method.

7.3.2 Simulation for Non-Seeded Initial States

We first investigate the interferometer sensitivity and its dependence on the total number of atoms with a coherent initial state and zero initial seed. In order to find the best sensitivity for a given set of parameters, the best operating point of the interferometer is first determined. The best operating point is the phase shift φ that minimizes $(\Delta\varphi)^2$. In Fig. 7.4, we plot the best sensitivities (lowest $(\Delta\varphi)^2$), normalized to the SQL, for different N as a function of number fraction inside the arms of the interferometer $\langle\rho_{\text{inside}}\rangle = \frac{\langle N_{\text{inside}}\rangle}{N}$. From $N = 1,000$ to $N = 50,000$, the sensitivity/SQL ratio is similar and there are regions where the sensitivity beats the SQL (sensitivity/SQL < 1) even for $N = 50,000$.

To summarize, for a non-seeded spin-mixing interferometer, by going to long evolution times, we find sensitivities better than the SQL even with large total atom number $N = 50,000$ and large numbers of atoms inside the arms of the interferometer $\langle N_{\text{inside}}\rangle > 2,150$.

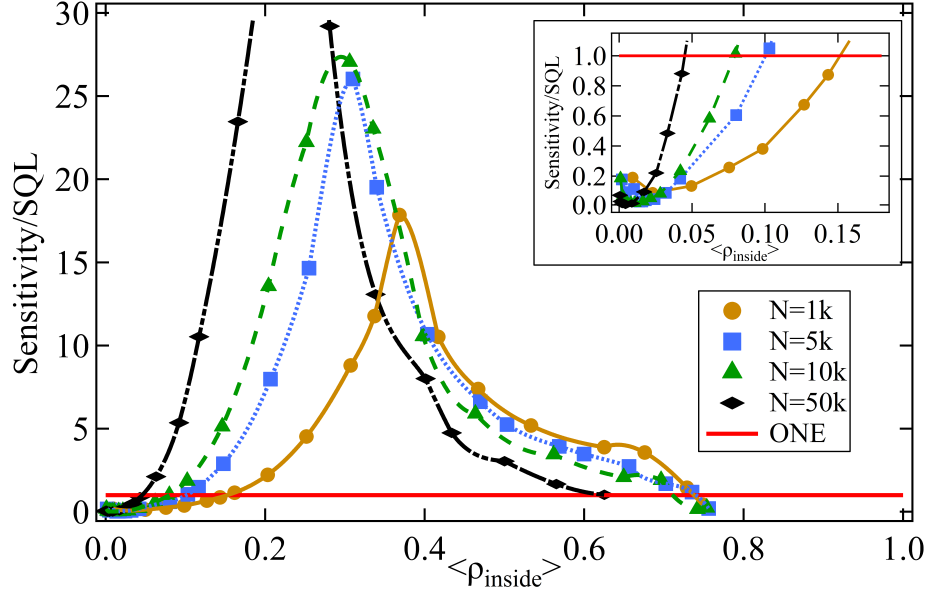


Figure 7.4: (Color online) Phase sensitivities for different N with zero initial seed. Shown are $N = 1,000$ (yellow circles), $N = 5,000$ (blue squares), $N = 10,000$ (green triangles), $N = 50,000$ (black diamonds). Here, $q/h = -2$ Hz. The red line depicts sensitivity/SQL = 1. Points below the red line correspond to quantum-enhanced sensitivity. The inset shows a zoomed-in region where enhanced sensitivities are found. The lines are intended as guide to the eye.

7.3.3 Simulation for Seeded Initial States

For evolutions with initial seeds, the initial seeds can be dual or single. For dual seeding, equal numbers of atoms are prepared in $m_F = +1$ and $m_F = -1$ states. For single seeding, all seeded atoms are prepared either in the $m_F = +1$ or in the $m_F = -1$ state. The effect of single and dual seeding on the phase sensitivity is shown in Fig. 7.5. We observe quantum-enhancement for both types of seeds.

The type of the initial state, either a coherent state or a Fock state, also makes a difference to the interferometer sensitivities. In Fig. 7.6 we compare the sensitivities for a coherent initial state with those for a Fock initial state, for different $\langle \rho_{\text{inside}} \rangle$. Here, we set $N = 1,000$ and used 2% dual initial seeds. The interferometer with a

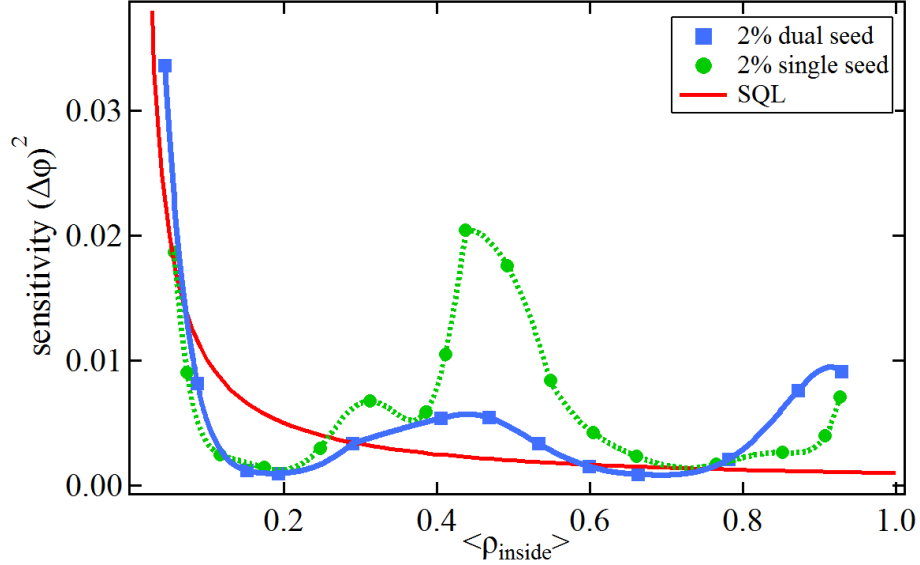


Figure 7.5: (Color online) Phase sensitivities for dual initial seeds (blue squares) and single initial seeds (green circles) with $N = 1,000$, coherent initial state and 2% initial seeds. Here, $q/h = -2$ Hz. The red line depicts the SQL. Points below the red line correspond to quantum-enhanced sensitivities. The lines are intended as guide to the eye.

coherent initial state has much better sensitivities than that with a Fock initial state. In the remainder of this thesis, all initial seeds are dual seeds, and all initial states are coherent states unless otherwise specified.

We now turn to compare the interferometry sensitivities for different initial seeds of 0%, 2%, 5%, 10%, and 20% of a fixed total atom number $N = 1,000$, shown in Fig. 7.7. We find sensitivities better than the SQL with up to 10% initial seeds and $\langle \rho_{\text{inside}} \rangle$ up to 0.34. We obtain quantum-enhanced sensitivities for much larger numbers of atoms in the arms of the interferometer compared to the unseeded cases.

In Fig. 7.8, we investigate the effects of total number $N = 100$, $N = 1,000$ and $N = 10,000$, on phase sensitivity with different initial seeds. We observe a strong dependence of sensitivity on N . Quantum-enhancement is present for all atom numbers

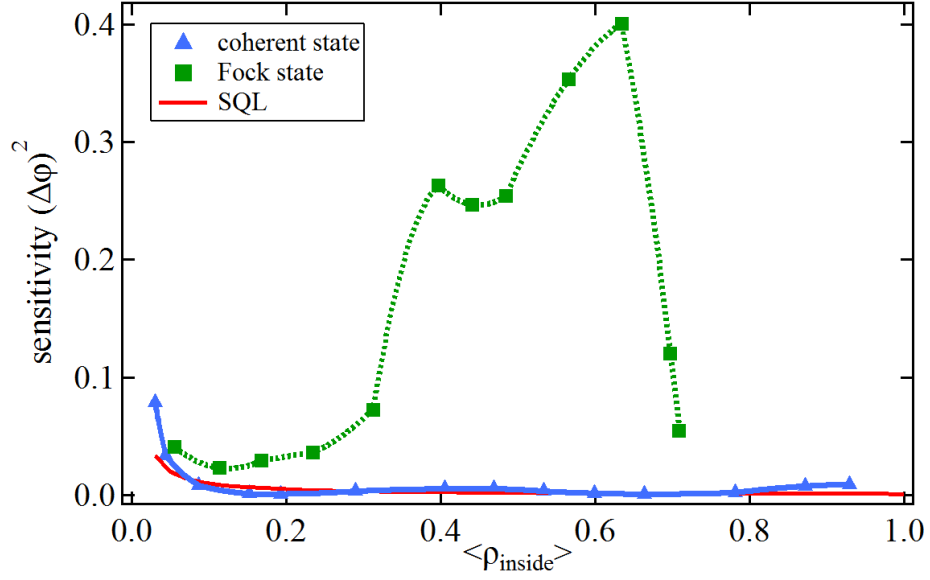


Figure 7.6: (Color online) Phase sensitivities for coherent initial state (blue triangles) and Fock initial state (green squares) with $N = 1,000$ and 2% dual initial seeds. $q/h = -2$ Hz. The red line depicts the standard quantum limit. Points below the red line correspond to quantum-enhancement. The coherent initial state performs better than the Fock initial state for all values of $\langle \rho_{\text{inside}} \rangle$. The lines are intended as guide to the eye.

that we studied. With larger seeds, the optimum sensitivity is obtained at larger values of $\langle \rho_{\text{inside}} \rangle$.

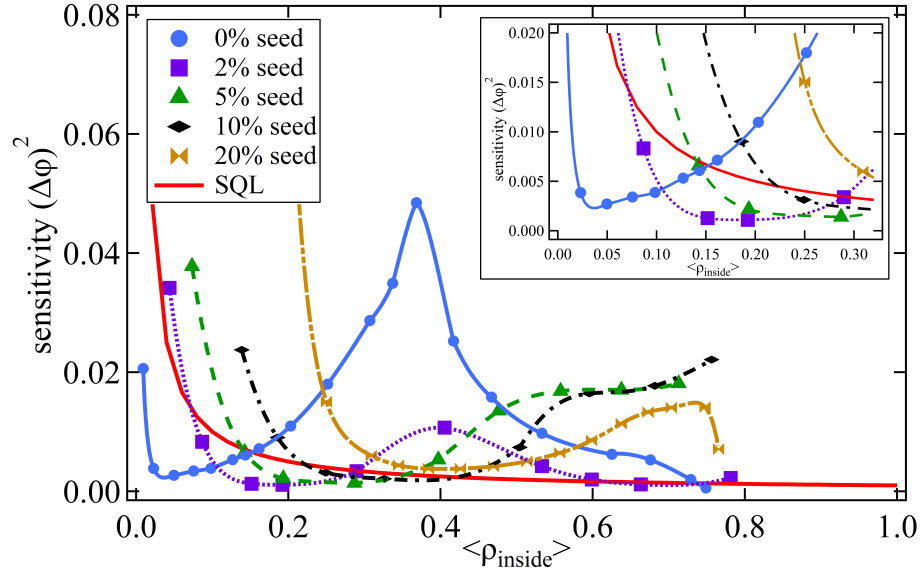


Figure 7.7: (Color online) Phase sensitivities for different initial seeds of 0% (blue circles), 2% (purple squares), 5% (green triangles), 10% (black diamonds), and 20% (yellow crosses). Here, $N = 1,000$ and $q/h = -2$ Hz. The inset shows a zoomed-in region where enhanced sensitivities are found. The SQL is shown as red solid line. Points below the red line correspond to quantum-enhanced sensitivities. The lines are intended as guide to the eye.

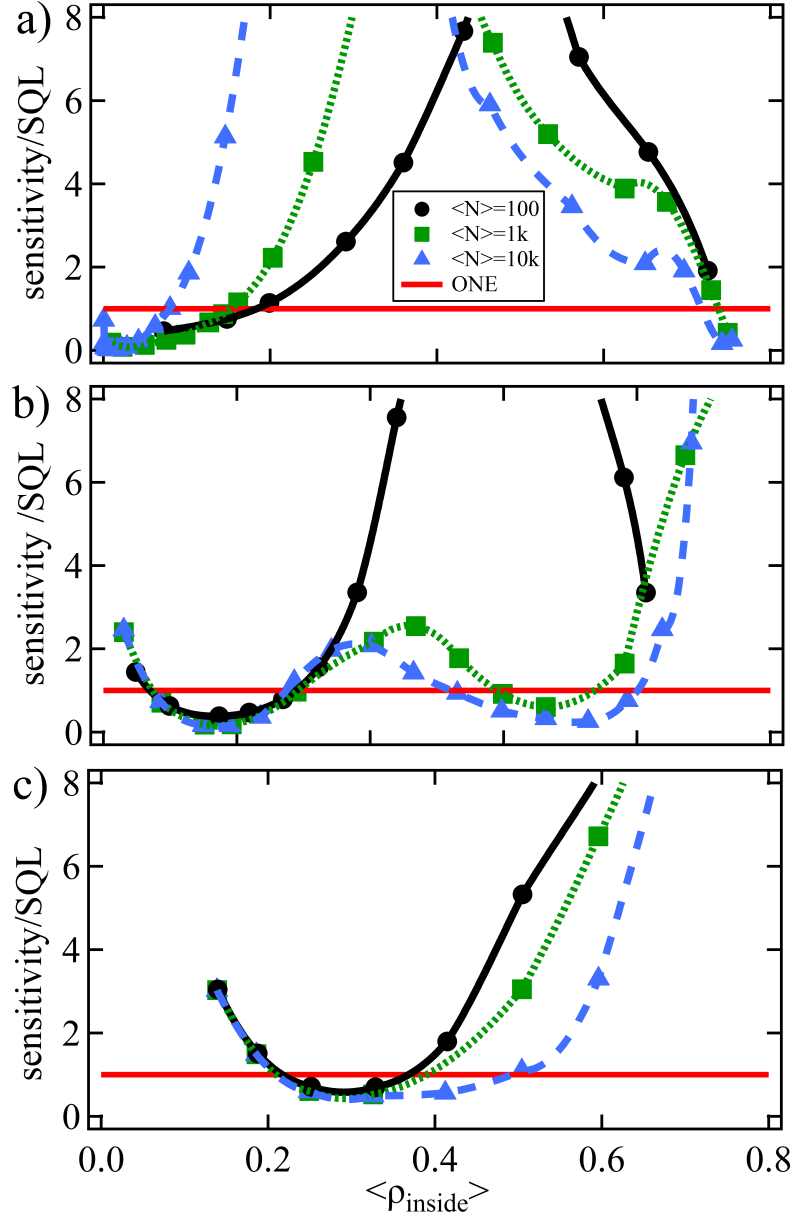


Figure 7.8: (Color online) Phase sensitivities as a function of $\langle \rho_{\text{inside}} \rangle$ for different total atom numbers $N = 100$ (black circles), $N = 1,000$ (green squares), and $N = 10,000$ (blue triangles), and initial seeds of (a) 0%, (b) 2%, and (c) 10%. Here, $q/h = -2$ Hz. The red line depicts the ratio of sensitivity/SQL = 1. Points below the red line correspond to quantum-enhancement. Even for large atom numbers of $N = 10,000$, quantum-enhancement is still predicted at longer evolution times. The lines are intended as guide to the eye.

7.4 Discussion

Our results show that there are parameter regimes where the interferometric sensitivity can be enhanced. The enhancement is due to a combination of factors, including the entanglement generation via spin-exchange collisions, the nonlinear measurement in the long time regime, and the seeding of the initial state. The entanglement generation causes reduced number uncertainties in the output. The nonlinear measurement in the long time regime causes enhanced slopes in the interferometer fringes. The seeding increases the speed of the evolution and the number of atoms in the arms of the interferometer. As a result of the interplay of these factors, the interferometer fringes and their uncertainties change shape in such a way that sensitivity can be enhanced for certain sets of parameters. Our results demonstrate that enhanced sensitivity can be obtained for any total atom numbers we considered and populations of up to several tens of percent in the arms of the interferometer, as long as the seeding is kept low, on the order of a few percent, and the BEC is small enough so that the single-mode approximation is valid.

We note that the BEC system is quite different from an analogous optical interferometer. For example, in the optical implementation with photons, a phase shift $\varphi = \pi$ applied to the pump beam always causes a time-reversal of the evolution, yielding a dark fringe [116]. However, in the spinor BEC, the phase shift that leads to a dark fringe is only equal to π in the limit of $t \ll h/c$, as shown in Fig. 7.9. This exemplifies the high nonlinearity of this atom interferometer in spin space, and is a result of the breakdown of the undepleted pump approximation.

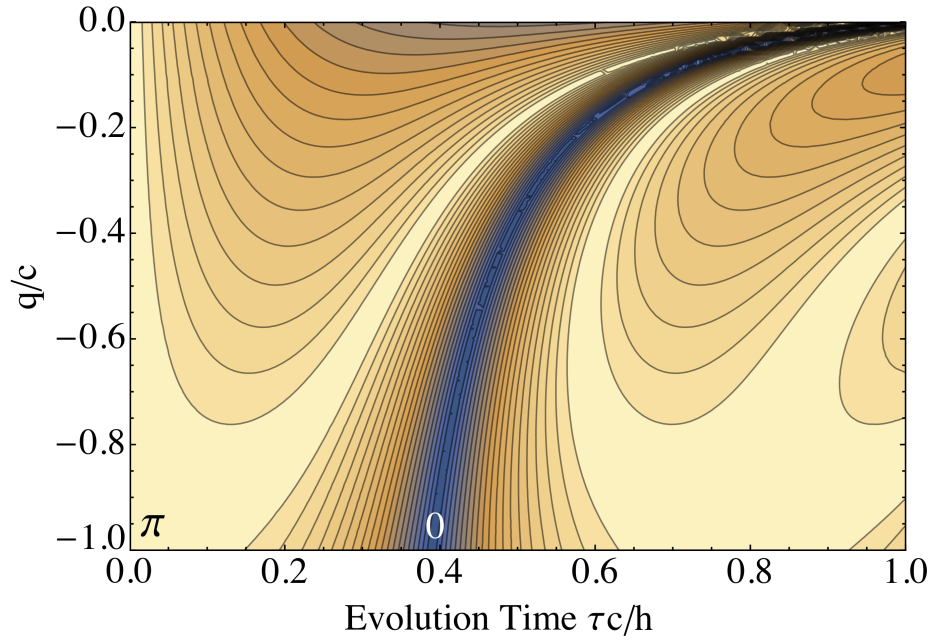


Figure 7.9: (Color online) Interferometer phase shift needed to cause an approximate reversal of spinor dynamics as a function of effective quadratic Zeeman shift q and evolution time τ . Here, we assume a 3% single sided seed. The brightest color means a phase shift of π , and darkest means zero phase shift. The calculation represents an estimate using a semi-classical model following Ref. [107].

7.5 Conclusion and Outlook

In conclusion, we numerically studied spin-mixing interferometry in microwave-dressed $F = 1$ Bose-Einstein condensates using realistic parameters that are accessible in experiments. We investigated the role of long evolution times and seeded initial states. By starting with coherent initial states with dual classical seeds from 0% to 10% in $m_F = \pm 1$, combined with long evolution times $t \gg h/c$, larger total atom numbers become accessible to realize interferometers with quantum-enhanced sensitivities. These interferometers rely on highly non-sinusoidal interferometer fringes.

We are using the simulation results presented here as guidance in our current experiments. We anticipate these results to be useful for future quantum technologies in matter-wave quantum optics, such as quantum-enhanced sensors based on spinor BECs.

A sensor based on quantum interferometry is versatile. It is sensitive to any effect that causes a spinor phase shift, for example, a relative energy shift between the $m = 0$ and $m = \pm 1$ levels. It could therefore act as a narrow-band microwave sensor, a B-field sensor, or a light shift sensor. One benefit of such a sensor compared to a thermal gas or classical antenna is the high spatial resolution. Because the BEC is only a few micrometers in size, one can for example map microwave fields in space by either moving the BEC around or by using an array of BECs.

Although current experimental BEC setups in laboratories require large optical tables and laser systems, progress has been made in developing more compact, ruggedized, and easy-to-use systems. For example, a BEC machine with the size of a few feet was installed and used successfully on a rocket [117], and latest efforts by the Bose-Einstein Condensate and Cold Atom Laboratory (BECCAL), a NASA-DLR collaboration, have resulted in a turnkey BEC system that was installed on the international space station. Laser-cooling systems, which are an integral part of any BEC

setup, have already been miniaturized to the chip scale of a few centimeters [118]. One can therefore envision that complete chip-scale BEC setups will become available in the future, which could be used as practical sensors in devices. Our findings could improve the sensitivity and the proposed seeding of the initial state could reduce the response time of such sensors.

Chapter 8

Experimental Setup for Spinor BECs

When I started my Ph.D. research in the group, the laboratory was newly renovated and empty (with only four empty optical tables). My early time in the group was working on the complete design and building of the custom BEC apparatus, from scratch up to the first successful generation of a BEC years later. The apparatus was a team effort of a group of four graduate students working on it continuously and over 10 undergraduate students who worked on the apparatus for senior research projects or summer research projects. I was involved in building all the parts of the apparatus described here. The parts of the apparatus I designed, built, and tested completely by myself are the MOT coils with the water cooling and control system, the microwave and rf antennas inside the chamber, the PID power supply for the sodium oven, the bipolar current supply for the bias coil, the hardware (PulseBlaster PCI cards and National Instruments DAQ cards) and software (LabVIEW) of the control system for our BEC experiment. My other major contributions to the experiment were simulation and testing of the bias coils, building a current buffer for the microwave source, making rf switches for the AOMs and many more. After the first BEC was demonstrated, I was involved daily in the optimization of the apparatus and data collecting of the experiments, such as increasing the BEC atom number, stabilizing the magnetic field, taking the spin evolution and matter-wave interferometer data. Meanwhile, I was working on numerical simulations to verify and optimize our experimental parameters.

In this chapter I introduce our experimental apparatus to achieve ultracold sodium spinor BECs. This includes the ultra-high vacuum system, optical setup for laser cooling and trapping, bias coil system, microwave and rf system, and a control system to implement experimental sequences. An atomic beam of sodium generated from the

sodium oven chamber is first slowed by a Zeeman slower, then atoms are captured and cooled in a 3D MOT in the main experimental chamber. Once the MOT is loaded, atoms are transferred to an optical dipole trap and evaporatively cooled to form a BEC. A bias coil system is used to compensate the earth's background magnetic fields and apply desired magnetic fields. Detection is done via Stern-Gerlach absorption imaging. To control spin-mixing dynamics and implement atomic interferometry in spin space, we use an rf and microwave system.

8.1 Vacuum System

An ultra-high vacuum (UHV) system is essential in generating BECs because any background gas atoms could collide with the trapped cold atoms and result in significant atom losses. Since evaporative cooling to the critical temperature takes several seconds, long trap lifetimes are needed. In order to obtain a long lifetime of trapped atoms of several seconds or more, it is crucial to keep the pressure in the vacuum system as low as possible. We designed and assembled an UHV system with pressure maintained at or below 10^{-11} Torr in the main experimental chamber. Our vacuum system is divided into three sections with decreasing pressures: the sodium oven chamber, the differential pumping chamber, and the main chamber, as shown in Fig. 8.1.

The sodium oven chamber contains a sodium reservoir, which consists of a stainless steel cup filled with a glass sodium ampoule containing 5 grams of 99.95% pure sodium. The pre-sealed glass ampoule is opened in air and quickly inserted, followed by pumping on the system to minimize reaction of Na with air. The apparatus can run about 2 years before the oven needs to be refilled. A custom copper nozzle inside the oven connects the reservoir to the oven chamber. The nozzle is 11.4 cm long with a center hole of 2.3 mm diameter. The nozzle has a ring that functions as a CF133 copper gasket with which it connects to the oven chamber. Due to the direct contact

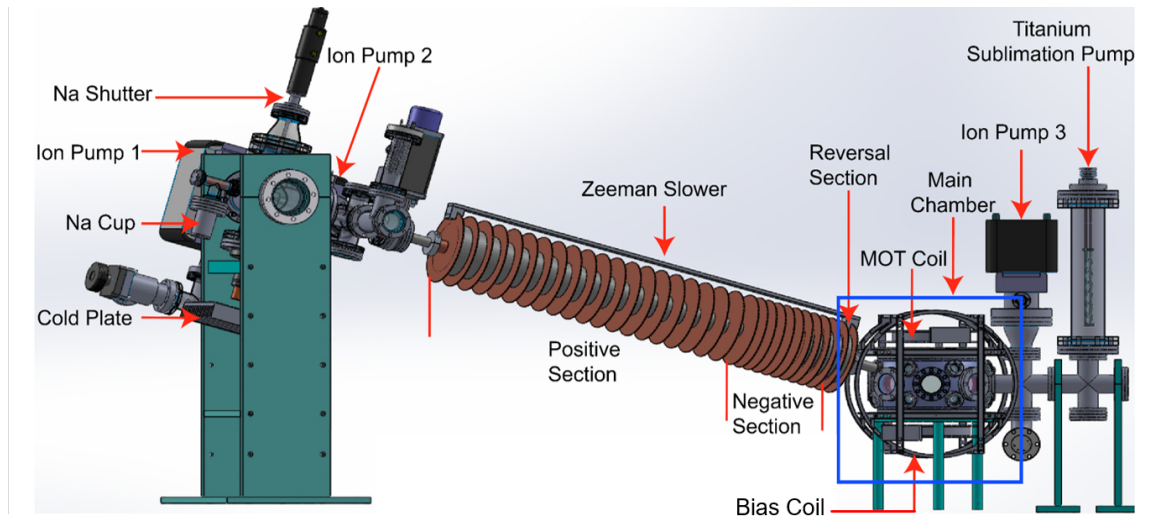


Figure 8.1: CAD drawing of our vacuum system. Following the atomic beam direction (left to right), there are the sodium cup, the sodium oven, the differential pumping chamber, the Zeeman slower, and the main chamber. Ion pumps, titanium sublimation pump and turbo pump (not shown in figure) are attached to the system to maintain UHV pressure. The blue square show the main chamber, with MOT coils and bias coils surrounding it.

of the nozzle with the CF133 flange, it can be efficiently heated from the outside via band heaters. We use two band heaters as flange heater to heat the front and back of the nozzle to $400\text{ }^{\circ}\text{C}$, to prevent sodium from condensing and clogging the nozzle. The sodium reservoir is heated by a band heater to $300\text{ }^{\circ}\text{C}$. All three band heaters are controlled by PID controllers to precisely control the temperature. After some experience with the system, we switched from CF copper gaskets to silver plated gaskets for all flanges exposed to high temperature, because the copper reacted with Na. The sodium reservoir and nozzle provide a continuous and stable sodium atomic flux. In front of the nozzle, a home-built copper cold plate with a hole at the center, cooled to $-12\text{ }^{\circ}\text{C}$ by six water-cooled arrays of TEC elements, is placed along the atomic beam path to collect hot sodium atoms not entering the main chamber and

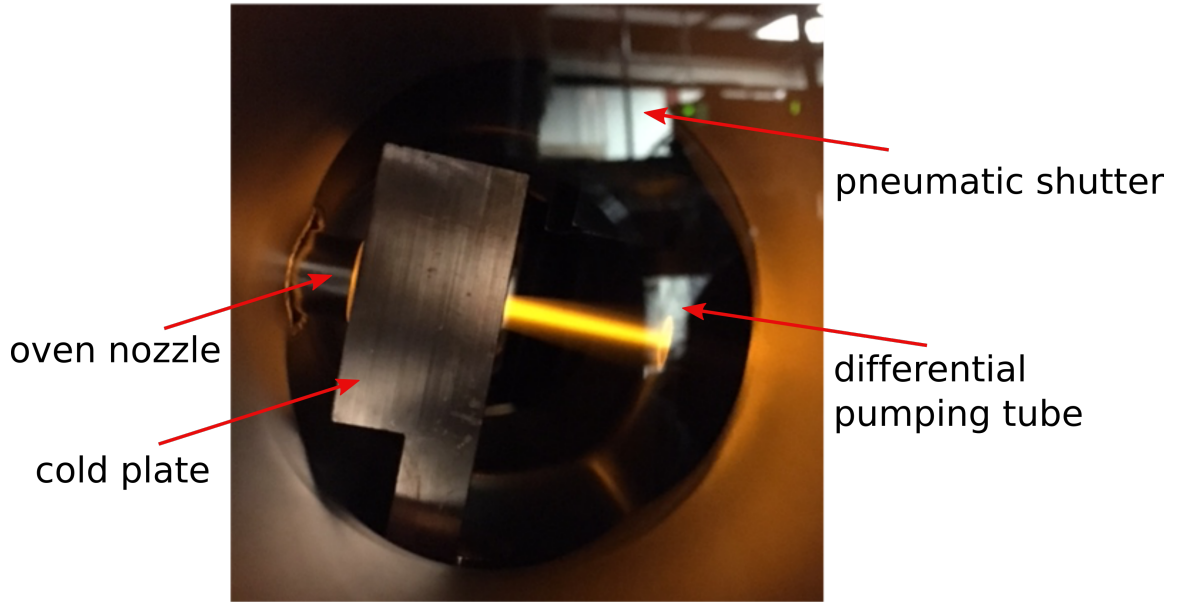


Figure 8.2: Photo of oven chamber taken from the side window. The cold plate has a centered hole which is aligned with the nozzle, and a mechanical shutter in between can shut on/off the atomic flux. The yellow light is the fluorescence of the sodium beam.

prevent the background pressure increasing. In order to collimate the atomic flux, the nozzle is aimed at the center hole of the cold plate. Fig. 8.2 shows a photo of the cold plate and nozzle, and the yellow fluorescing sodium beam. A mechanical shutter is placed between the cold plate and the nozzle to turn on/off the atomic flux entering the main chamber during experiments. After rough pumping with a turbo pumping station, a 50 L/s ion pump (Ion Pump 1 in Fig. 8.1) is used to pump the oven chamber to a pressure around 10^{-8} Torr.

A differential pumping chamber is connected between the oven chamber and the main chamber. An ion pump (Ion Pump 2 in Fig. 8.1) is attached to the differential pumping chamber to pump it to a pressure of around 10^{-9} Torr. At the end of the differential pumping chamber, a pneumatic gate valve is installed between the differential pumping chamber and the Zeeman slower to protect the vacuum in the main chamber when work on the oven is performed, or sodium is refilled, and to seal

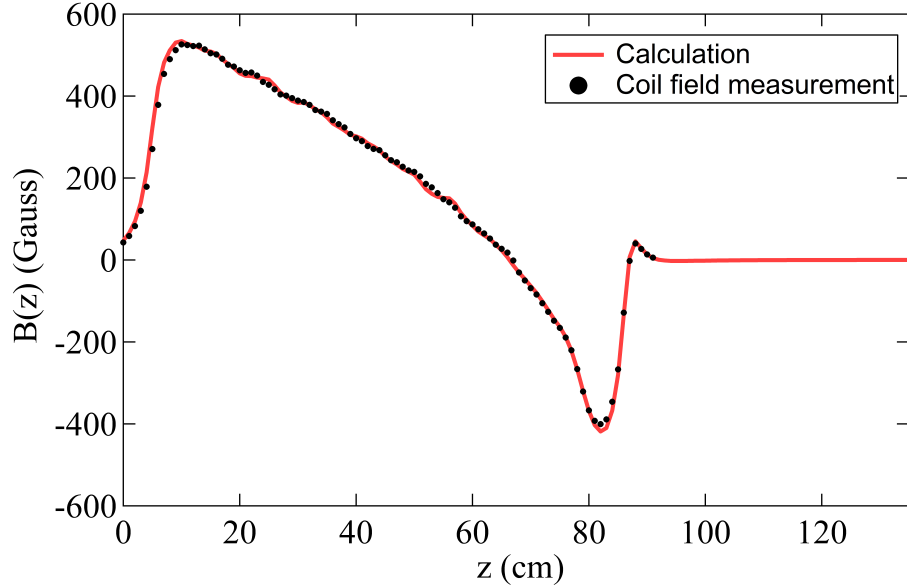


Figure 8.3: Measured magnetic field generated by Zeeman slower coils (black dots) compared to the simulated field (red line).

off the main chamber in case of any unexpected pressure rise. After running the experiment for about 2 years, enough sodium deposited on the cold plate so it had to be cleaned.

A Zeeman slower is connected after the differential pumping chamber to slow down atoms before entering the MOT in the main chamber. A MOT can only capture atoms below a certain velocity called capture velocity, usually on the order of 10 m/s, while the atoms leaving the reservoir move at velocities around 800 m/s. In order to improve the MOT capture efficiency, we use a Zeeman slower to slow down the atomic beam to velocities that can be captured by the MOT. A Zeeman slower uses the Doppler cooling technique to slow atoms. In a Zeeman slower, the atoms are irradiated by a counter-propagating laser beam with a frequency ω that is appropriately red-detuned. The fast moving atoms can absorb the photons due to the Doppler shift and therefore be slowed down. However, once the atoms are slowed to a point where they are no longer resonant with the laser frequency ω and they would be lost from the slowing

process. The idea behind a Zeeman slower is, instead of chirping ω , to tune the atomic transition by applying a spatially varying magnetic field to counteract the changing Doppler shift and continuously keep slowing down atoms on their way to the chamber [119, 120]. In our system, we use a segmented Zeeman slower design, which consists of modular, multi-layered coils of magnetic wire. Using small diameter wire wound around a small diameter tube with multiple horizontal and vertical loops, we can generate a spatially dependent large magnetic field with a low current. One advantage of our design, where segments are interspaced with copper discs that serve as passive heat sinks, is that the heat generation is low, so water-cooling is not necessary, as shown in Fig. 8.1. Based on numerical simulation, we designed a Zeeman slower that consists of 31 segments, where the first 20 segments produce a positive field and the last 10 segments produce a negative field with a running current of 4 A. An additional coil with positive current was added to the end to control the minimum of the field at the end of the slower. It is needed to precisely tune the final velocity and prevent atoms from being pushed back into the slower after they exit. Fig. 8.3 compares the measured magnetic field generated by the Zeeman slower, measured with a Hall-effect based Gauss meter, with the simulation result, showing that our Zeeman slower meets our design. We chose to orient the Zeeman slower diagonally upwards so it is not in the way of other components, so we could keep the optical access provided by the bigger windows. The window opposite to the Zeeman slower is periodically cleaned by shining UV light on it from the outside for several hours. This method of cleaning the window by light induced atomic desorption is convenient, because the main chamber doesn't have to be opened.

The last section of our vacuum system is the main chamber, in which our sodium BECs are created. The main chamber is a spherical octagon UHV chamber from Kimball Physics with 26 CF ports (with three kinds of OD diameters: 8", 2.75" and

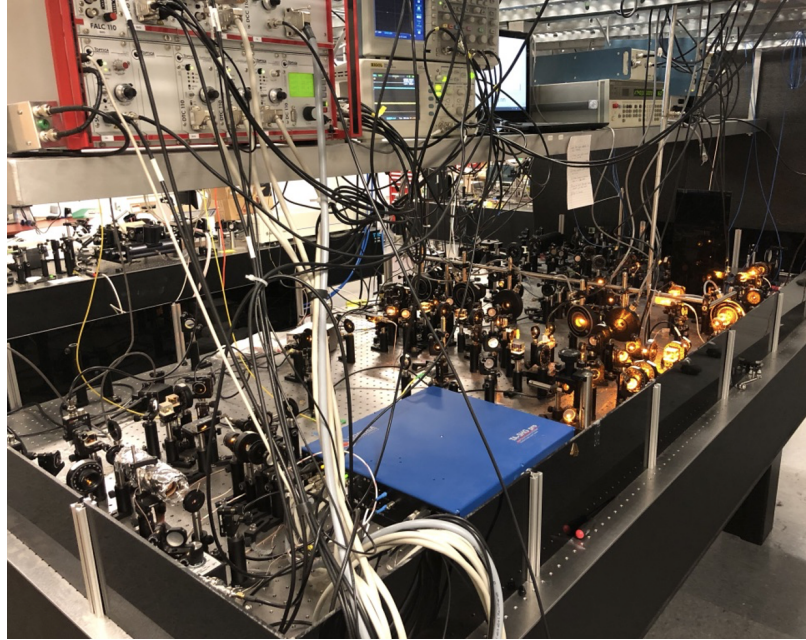
1.33") in different directions, which provides sufficient access for optical, vacuum and electric setups. An ion pump (Ion Pump 3 in Fig. 8.1) and a titanium sublimation pump are connected to the main chamber to further reduce the pressure. Finally, the pressure in the main chamber is kept below 10^{-11} Torr, monitored continuously via ion pump current. Initially it was also measured by turning on an ion gauge. The ion gauge is usually turned off because it increases the pressure due to outgassing.

8.2 Optical Setup

8.2.1 Optics Layout

The optical system in our apparatus is critical for laser cooling and trapping, as well as imaging. The main optical system fits on one $5'' \times 10''$ optical table, separated from the $4'' \times 10''$ optical table that holds the vacuum system, as shown in Fig. 8.4. In our setup, the main light source is a Toptica TA-SHG Pro diode laser, designed to operate at wavelength $\lambda \approx 589$ nm with a continuous output power of 1 Watt. To prevent long-term frequency shift, a small portion (~ 11 mW) of the laser output is sent to a home-built saturated absorption spectroscopy system to lock the laser frequency, as described in Sec. 4.1. The output laser light wavelength is coarse tunable within a range of 4 nm, which is wide enough for BEC experiments, and even for switching between the sodium D_1 and D_2 line.

Fig. 8.5 shows the optical layout to generate different laser beams for cooling, repumping and imaging. Polarizing beamsplitter (PBS) cubes, half-wave ($\lambda/2$) plates and quarter-wave ($\lambda/4$) plates are used to split the laser beam and adjust the polarization. We use acousto-optic modulators (AOMs) to shift the laser frequency for different beams, the frequencies of the beams are shown in Fig. 8.6. Laser beams with proper frequencies are then aligned to polarization maintaining (PM) optical fibers and delivered to a separate optical table with the vacuum system. A fast



(a)



(b)

Figure 8.4: (a) The $5' \times 10'$ optical table that holds the main optical system. (b) The $4' \times 10'$ optical table that holds the vacuum system. The laser beams derived from the main optical system are delivered to the vacuum system via optical fibers.

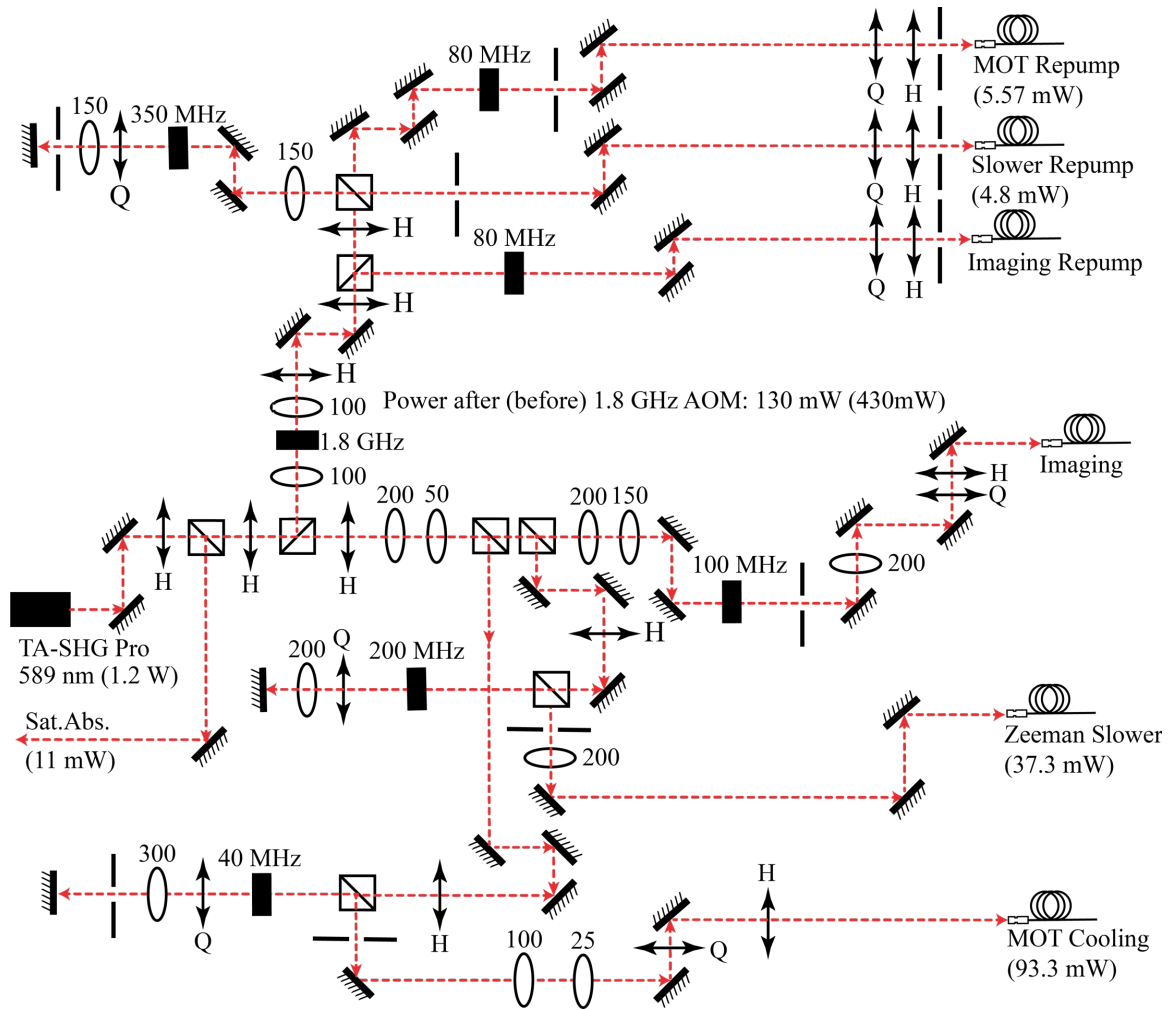


Figure 8.5: Optical layout for generating cooling, repumping and imaging beams. The abbreviations are AOM: acousto-optic modulator, Q: quarter wave plate, Sat. Abs: Saturated Absorption Spectroscopy, H: half-wave plate, numbers: focal length in mm. All cubes are polarizing beamsplitter cubes. The apertures shown before fibers and in the paths denote mechanical shutters.

mechanical shutter is placed along each beam path to quickly switch on/off the specific beam during an experimental sequence. All the shutters and AOMs are automatically controlled by a control system, see Sec. 8.5.

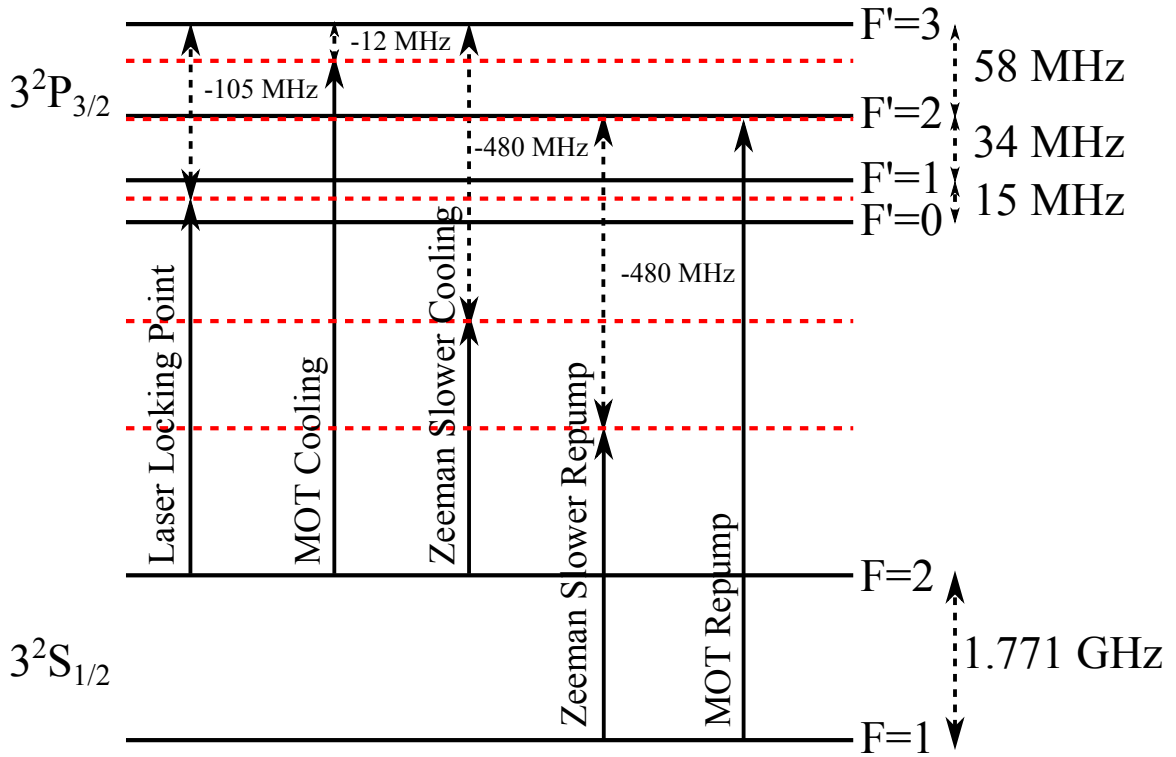


Figure 8.6: Diagram of different laser beam frequencies compared to sodium D_2 line hyperfine structure. Frequencies are not drawn to scale.

8.2.2 MOT Setup

Sodium atoms from the hot oven will first be pre-slowed and slightly cooled by the Zeeman slower, with the velocities reduced from ~ 700 m/s to ~ 20 m/s. The Zeeman slower beam is red-detuned by 480 MHz and counter-propagates inside the tube toward the atomic beam. Leaving the Zeeman slower, atoms enter the main chamber and are captured by a 3D MOT. The 3D MOT beams are three pairs of counter-propagating laser beams with different polarizations intersecting at the center. The MOT cooling beams are red-detuned by $\delta = -12$ MHz from $F = 2$ to $F' = 3$ transition with a power of ~ 5 mW each, as shown in Fig. 8.6. With small probability, the MOT cooling beams can excite the atoms to $F' = 2$ excited state, from which atoms can decay to the $F = 1$ ground state via spontaneous emission. Such $F = 1$ atoms would be lost from the

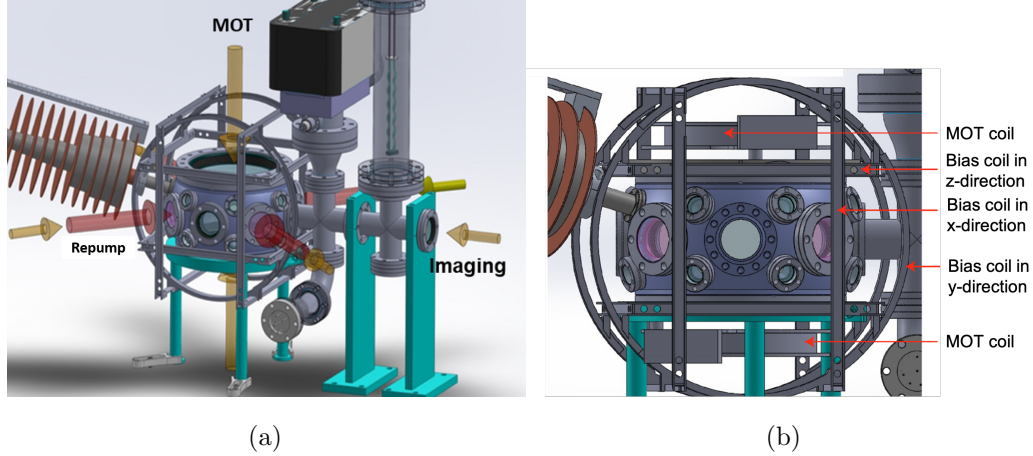


Figure 8.7: Zoom-in of MOT CAD drawing. (a) The MOT cooling and repumping beams shine into the main chamber via four 2.77" outer diameter viewports on the sides and two 8" outer diameter viewports on top and bottom. (b) The two anti-Helmholtz coils for the MOT are mounted on the top and bottom viewports. The three pairs of Helmholtz bias coils surrounding the main chamber generate a uniform background magnetic field.

cooling cycle, because, due to the large ground state hyperfine splitting (~ 1.7 GHz between $F = 1$ and $F = 2$), they cannot be re-excited by the MOT cooling beams. In order to keep all atoms in the cooling cycle, two pairs of ~ 3.5 mW repumping beams, overlapping with cooling beams, are turned on at the same time to optically pump atoms from the $F = 1$ state to the $F' = 2$ excited state. The MOT cooling and repumping beam configuration is shown in Fig. 8.7a.

In addition to the cooling and repumping laser beams, a MOT also requires a magnetic field gradient. In addition to the use for the MOT, the magnetic field gradient is also used in Stern-Garlach absorption imaging to quickly separate the spin states of atoms, as discussed in Sec. 8.3. In order to capture more atoms (and separate different spinor states quickly during imaging), a strong, quickly-changeable, and stable magnetic gradient is required.

Table 8.1: Parameters of anti-Helmholtz coils.

Quantity	Value
Inner diameter	13.9 cm
Coil distance	17.8 cm
Radial turns	4
Axial layers	5
Field gradient	12.13 G/cm
Total wire length	20.09 m
Total resistance	0.06 Ω
Current	82 A
Total voltage	5.23 V
Joule heating	403 W
Total power	429 W

I designed a pair of anti-Helmholtz coils that is able to generate a magnetic field gradient of about 12 Gauss/cm. An anti-Helmholtz coil pair is a configuration where a pair of current loops have opposite current directions and generate the most linear gradient at the center. It is a convenient setup for generating a magnetic field gradient when geometric constraints limit the length of the coils. A numerical simulation was first done in Mathematica to optimize the coil design. First, the geometry of the coils is defined as circular loop. Then, the magnetic field generated by current-carrying wire is derived from the Biot-Savart law:

$$\mathbf{B} = \frac{\mu_0 I}{4\pi} \int \frac{d\mathbf{L} \times \hat{\mathbf{r}}}{r^2}, \quad (8.1)$$

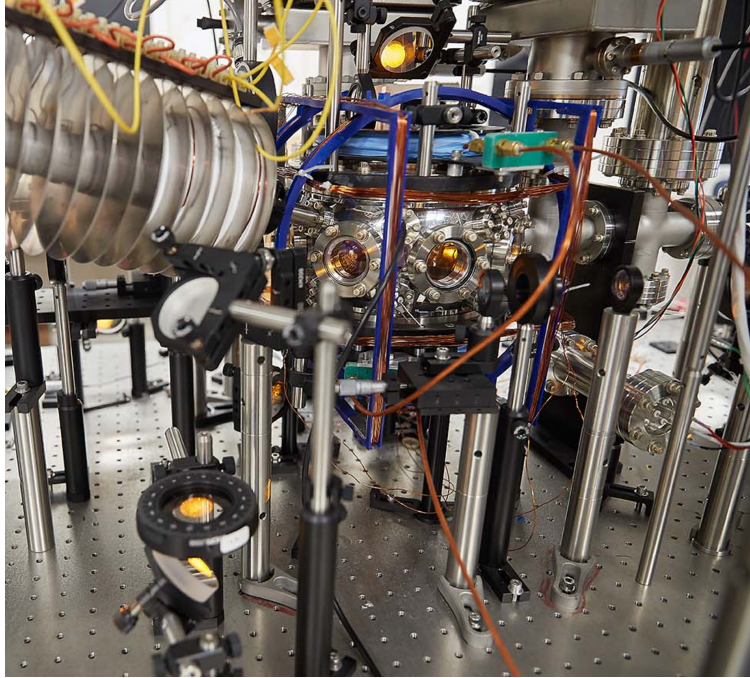
where dL is the infinitesimal length of conductor carrying electric current I . Next, the constraints on the coils are defined. The current I carried by the wire cannot be too high as the heat generation grows quadratically with I . In addition, high-current DC

power supplies are expensive and limited. The heat dissipation on the high-current wire requires water cooling, so we decided to use Kapton insulated hollow core copper tube to carry the current. The large diameter (3.2 mm) of the hollow core tube limits the number of loops on each coil. After numerical optimization, each coil was chosen to have 5 layers with 4 turns in each layer and the inner diameter of the coils is 14 cm. The parameters of the coils are shown in Table. 8.1. The anti-Helmholtz coils are wound on home-built frames and installed on top and below our main chamber, as shown in Fig. 8.8. From Table. 8.1, we see that the coils generate Joule heating at the power of 403 Watts, which is dissipated by cooling water running through the center of the hollow core copper tube. The cooling water is circulated via a heat exchanger (Neslab System I water-to-water heat exchanger). We use a high power programmable DC power supply (Sorensen DCR 16-310T), and an IGBT switch to quickly control the coil current. The two coils are installed on custom-built aluminum frames mounted above and below the main chamber, as shown in Fig. 8.7b.

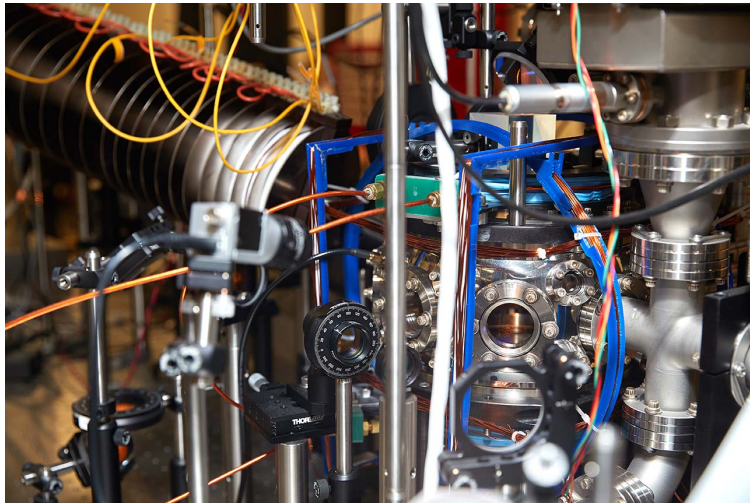
Fig. 8.9 is a photo of atoms trapped in our MOT. After optimizing the parameters, we typically collect $\sim 3 \times 10^8$ atoms in the MOT. The number of atoms is measured via absorption imaging method, which is described in detail in Sec. 8.3.

8.2.3 Bias Coils

Besides the anti-Helmholtz coils for the MOT, we also place three pairs of bias coils around the main chamber, as illustrated in Fig. 8.7b and Fig. 8.8. The bias coils are in Helmholtz configuration and hence generate a uniform magnetic field at the region of MOT, which can be used to set the background magnetic field. The bias coils usually run at a current magnitude below 4 A and the heat generation is low, so we use copper wires wound around 3D-printed plastic frames for an efficient setup. It turns out that the current fluctuation on the bias coils, which leads to magnetic field



(a)



(b)

Figure 8.8: Photos of experimental chamber. A pair of anti-Helmholtz coils for the MOT are mounted on the top and bottom viewports and are wound around black-anodized aluminum frames. Three pairs of Helmholtz bias coils, mounted on blue plastic frames surrounding the main chamber, generate a uniform background magnetic field.

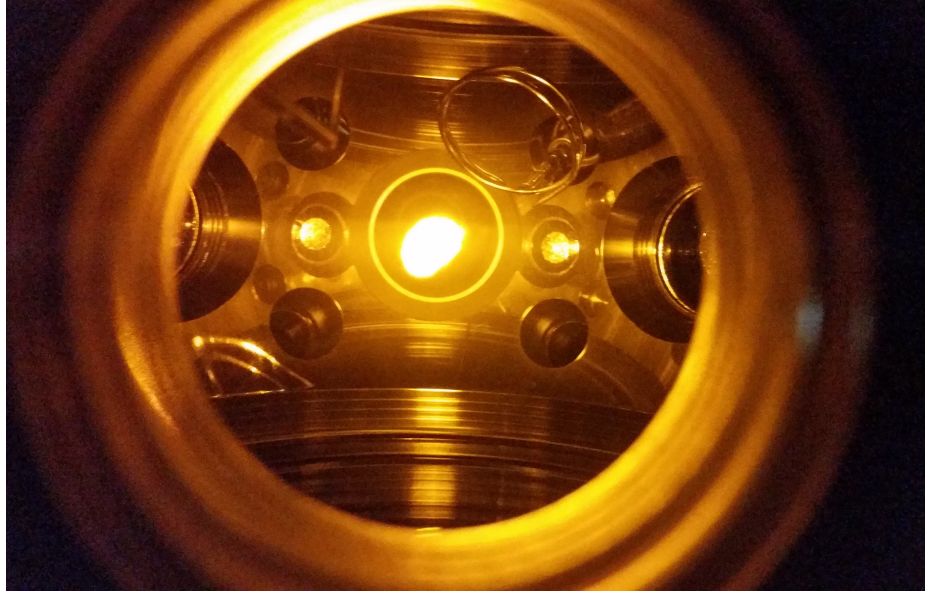


Figure 8.9: A photo of the trapped atomic cloud in the MOT at the center of the chamber. We use a large MOT cooling beam diameter of 0.8 inches to trap more atoms. Above the cloud, there is the half-dipole antenna for microwave-dressing and a loop antenna for rf radiation. See Sec. 8.4 for more details.

fluctuation, has a significant impact on the microwave-dressed spin-mixing dynamics in the BEC which are our focus of study. Therefore, a stable current is important for the bias coils. In addition, the magnetic field generated by the bias coils must be quickly adjustable, not only in amplitude, but also in direction during the experiment, as necessary. To satisfy these requirements, we drive the bias coils with a highly stable home-built, bipolar DC current supply, which has six individual channels whose outputs are controlled by analog input voltages and stabilized by PID controllers. The supply is based on commercial temperature controllers (Wavelength Electronics PTC5K-CH) which we modified for faster ramp time and outfitted with analog input voltage shaping circuit to allow computer control via an analog output voltage PCI board (National Instruments DAQ board).

8.2.4 Optical Dipole Trap Setup

In our system, the MOT can cool the sodium atoms to a temperature around 1 mK. In order to form a BEC, further cooling of sodium atoms in the MOT to below critical temperature, which is in the order of tens of nK is necessary. We apply polarization gradient cooling over a short period (~ 30 ms), where the MOT cooling beam power and detuning are increased to compress the MOT, while the MOT repumping power is reduced. To pump the atoms into the $F = 1$ hyperfine state, the MOT repumping beams are switched off 1 ms before the MOT cooling beams and the magnetic field gradient is extinguished. The polarization gradient cooling reduces the atomic gas temperature to ~ 70 μK . It would be quite difficult to cool the atoms below the micro-Kelvin range using any near-resonance light, due to the recoil limit. The recoil is associated with the spontaneous emission which leads to a momentum change. The recoil limit is defined as the lowest achievable temperature with laser cooling, given by

$$T_{\text{recoil}} = \frac{(h/\lambda)^2}{2mk_B}, \quad (8.2)$$

where λ is the cooling light wavelength, m is the atom mass and k_B is the Boltzmann constant. For sodium, $T_{\text{recoil}} \approx 2\mu\text{K}$.

Our optical dipole trap (ODT) is used to cool the atoms into the nano-Kelvin regime after the MOT. Atoms at the center of the MOT are loaded into the ODT and then a forced evaporative cooling is applied to achieve a BEC. In our system, the ODT consists of two crossed far-detuned laser beams derived from an infrared (IR) fiber laser (IPG photonics YLR-50-1064-LP) with an output power of 50 W at 1064 nm. The two IR laser beams are tightly focused, with a $1/e^2$ beam waist of approximately 35 μm and overlap at the center of the chamber. Fig. 8.10 shows the schematic of our crossed ODT setup. The dipole trap beam intensity is controlled by an AOM. In order to achieve a stable number of atoms in the BEC during experiments, the intensity noise of the dipole trap light needs to be minimized. We built a noise eater

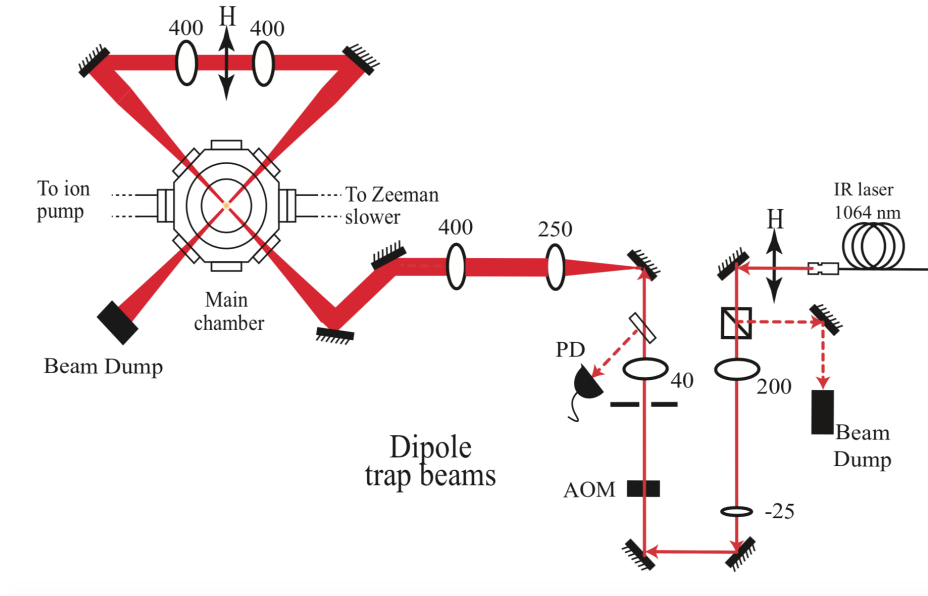


Figure 8.10: Schematic of our ODT setup. The far-detuned IR light originates from a fiber laser and is focused at the center of the MOT after passing through an AOM. The laser beam exiting the chamber is reflected and focused at the chamber again. The two beam paths crossed at the center of the MOT.

with an amplified fast photodiode that constantly samples the IR power and sends a fast signal (1 MHz bandwidth) to a commercial PI controller. The PI controller compares the photodiode signal with a setting voltage from a computer-programmed high-resolution (16-bit sampling rate) function generator (Agilent 33521A), then generates an output signal to the AOM driver's amplitude-modulation input to stabilize the dipole trap beam intensity. Our dipole trap has trap frequencies around $(\omega_x, \omega_y, \omega_z) = 2\pi \times (121, 113, 202)$ Hz. The dipole trap frequencies are re-measured after tweaking of the dipole trap beams every few days.

8.3 Imaging System

8.3.1 Absorption Imaging

Absorption imaging is used to probe the ultracold atomic clouds in situ and in time-of-flight (TOF) [60]. In a TOF, the measured atomic cloud is released from an optical or magnetic trap and allowed to expand ballistically. In our system, we use absorption imaging to quantitatively obtain information such as the size, shape, atomic density, temperature, spin populations, and so on. In order to obtain absorption images, a resonant probe laser light which couples the $3^2S_{1/2}, F = 2$ and $3^2P_{3/2}, F' = 3$ states of ^{23}Na illuminates the atomic cloud. The shadow of the cloud is imaged onto a CCD camera using a lens configuration. The intensity profile of a low intensity probe beam after the absorption follows the Lambert-Beer law

$$I(x, y) = I_0(x, y)e^{-OD(x, y)}, \quad (8.3)$$

where I_0 is the initial light intensity of the probe beam before passing the atomic cloud, and $OD(x, y)$ is the optical density profile in transverse directions x and y . $OD(x, y)$ is given by

$$OD(x, y) = \sigma n_c(x, y) = \sigma \int n(x, y, z) dz, \quad (8.4)$$

where σ is the absorption cross section, $n_c(x, y)$ is the column density, which is obtained by integrating number density $n(x, y, z)$ along the imaging light propagating direction z . σ depends on the intensity, polarization and detuning of the probe beam as

$$\sigma = \frac{\sigma_0}{1 + 4\left(\frac{\Delta}{\Gamma}\right)^2 + \frac{I}{I_{sat}}}, \quad (8.5)$$

where σ_0 is the on-resonance cross section which depends on the light polarization and atomic transition, Δ is the detuning of the imaging light from the atomic resonance, Γ is the natural linewidth of the optical transition, and I_{sat} is the saturation intensity.

From Eq. (8.3), the optical density profile of the atomic cloud can also be derived as

$$OD(x, y) = -\ln \frac{I(x, y)}{I_0(x, y)}. \quad (8.6)$$

This can be calculated by taking two absorption images, the image with atomic cloud $I(x, y)$ and the image without any atoms $I_0(x, y)$. We take an additional image without the probe light and without any atoms to extract the background noise $I_{bg}(x, y)$. So we rewrite $OD(x, y)$ as

$$OD(x, y) = -\ln \frac{I(x, y) - I_{bg}(x, y)}{I_0(x, y) - I_{bg}(x, y)}. \quad (8.7)$$

Based on the optical density profile $OD(x, y)$, the column number density $n_c(x, y)$ can be calculated using Eq. (8.4). The atom number is then obtained by integrating $n_c(x, y)$ over x and y directions, using the known pixel size and magnification of the CCD camera, and summing up all the pixels in images. Alternatively, a Gaussian, a bimodal, or other density function can be fitted to the $n_c(x, y)$ profile to obtain the atom number, position and width of the cloud.

8.3.2 Imaging System

We built top and side absorption imaging systems so that we can probe the atomic cloud from different directions. Fig. 8.11 shows the schematic of our absorption imaging setup. We use achromatic doublet lenses to minimize spherical aberration and chromatic aberration. Different magnifications can be used to detect either the large MOT or the small BEC, depending on their sizes. For example, we often use a small magnification of $M = 0.6$ to image the MOT, and a large magnification of $M = 2$ to image the BEC. This can be achieved by using different lens configurations. Two high-performance CCD cameras (PCO Pixelfly USB) for top and side imaging are installed on high-precision translation stages with micrometer screws to adjust the focus precisely. To reduce interference fringes due to etaloning, we place a quarter-wave

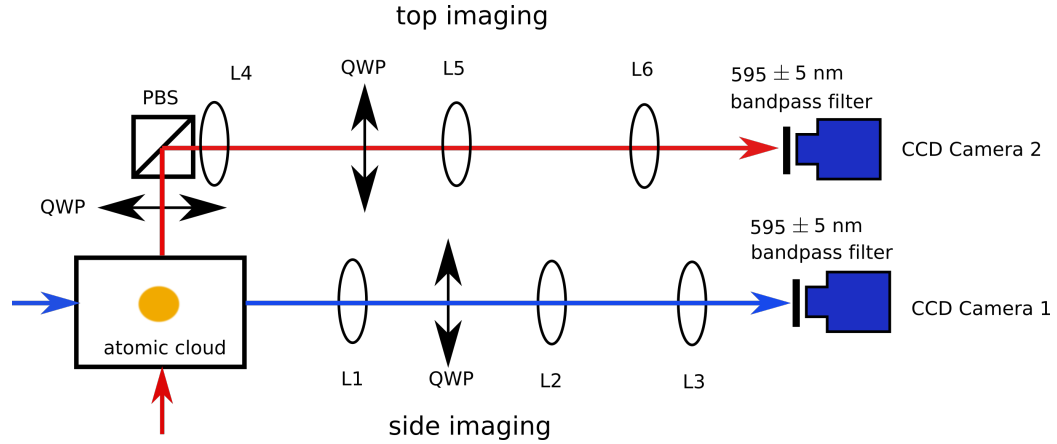


Figure 8.11: Schematic of our absorption imaging setup. Top and side imaging systems are used to obtain absorption images of the ultracold atomic cloud inside the vacuum chamber. Camera 1 along with lenses L1, L2, L3 and quarter-wave plate (QWP) make up the side imaging system. Camera 2 and associated optics comprise the top imaging system. The positions of the lenses and cameras can be adjusted to change the magnification of the imaging systems for different detection purposes. The focal length of L1, L2, L4 and L5 is $f = 150$ mm, the focal length of L3 and L6 is $f = 50$ mm.

plate (QWP) in the center of the imaging telescope to get better imaging quality with less residual interference fringe patterns. All optics are outside the vacuum chamber so that it is easy to make adjustments. Our imaging system is controlled by a computer via a LabVIEW program. Images collected by the CCD cameras are sent to the computer and analyzed automatically during the experiment on the Igor data analysis software. This automatic analysis allows us to quickly judge problems such as misalignment of the dipole trap beams as they happen.

The BEC cloud inside the trap can be imaged either in-situ, or after some time of flight (TOF) after being released. While the in-situ probe can measure the original geometric configuration of the atomic cloud inside the trap, the BEC cloud is sometimes too small to resolve, in the order of a few μm , taking only a few pixels on the CCD camera, or too dense to measure quantitatively, because the BEC shadow becomes

completely black in the images at high optical densities larger than 2. The TOF measurement has better resolution on small and dense atomic clouds by turning off the trap and allowing the atoms to expand freely for a few milliseconds, resulting in larger cloud with smaller optical density. Additionally, TOF is commonly used to measure the temperature of cold gases. In time of flight expansion, the momentum distribution of the atoms converts to a spatial distribution assuming the cloud expands ballistically, this can be used to infer the temperature. The size of the MOT cloud $\omega(\tau)$ after expansion time τ follows $\omega(\tau) = \sqrt{\omega(0)^2 + v\tau^2}$, where $\omega(0)$ is the initial size, and v is the velocity of the atoms. According to equipartition theorem, the velocity can be related to temperature by $v = \sqrt{3k_B T/m}$, where T is the temperature of the atomic cloud, k_B is the Boltzmann constant, and m is the atomic mass. So the temperature of the atomic cloud can be found by

$$\omega(\tau) = \sqrt{\omega(0)^2 + (k_B T/m)\tau^2}. \quad (8.8)$$

This method can be used to determine the temperature of thermal clouds such as the MOT. For BEC atoms, the relation is different because the BEC expansion is dominated by the repulsive interaction due to the mean-field s-wave scattering [121].

Fig. 8.12 shows false-color absorption images of our MOT and spinor BEC. The sequences for probing MOT and BECs that we use are different. For MOT imaging, we take absorption images after a few milliseconds of time-of-flight, as shown in Fig. 8.12a. Fig. 8.12b shows the time of flight expansion width measurement of the optical molasses. When fitted to Eq. (8.8) this gives a temperature of $65.5 \pm 0.1 \mu\text{K}$. To measure the atomic populations in different magnetic sub-states of a spinor BEC, a strong magnetic field gradient pulse generated by the anti-Helmholtz coils is applied to separate the three spin states during time-of-flight. This is known as Stern-Gerlach absorption imaging. Fig. 8.12c shows a typical Stern-Gerlach image of three spin components of our spinor BEC after 10 ms time of flight, from left to right are

absorption images of atoms in $m_F = -1$, $m_F = 0$ and $m_F = +1$ state. In this example, BEC atoms were initially prepared in the $m_F = 0$ state, and then transferred to the $m_F = +1$ or $m_F = -1$ states by applying radiofrequency (rf) pulses or microwave pulses, as explained in next section.

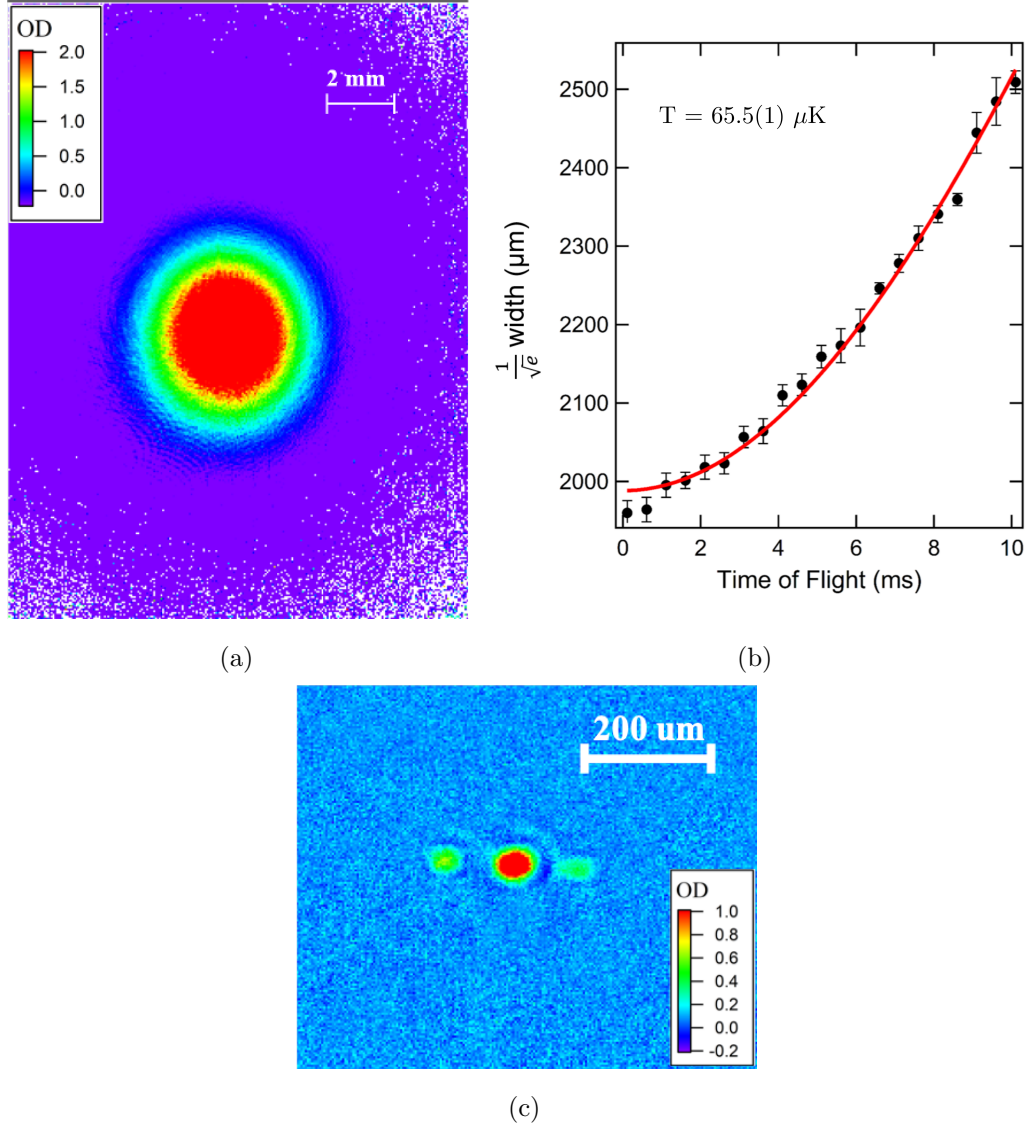


Figure 8.12: False color images from absorption imaging. (a) The MOT absorption image taken after a few milliseconds of time-of-flight. (b) Time of flight expansion of the optical molasses. The $1/\sqrt{e}$ width was obtained from Gaussian fits to absorption images. The line is a fit to Eq. (8.8). The fit gives a temperature of $65.5 \pm 0.1 \mu\text{K}$. (c) Stern-Gerlach absorption image showing atoms in different spin states after 10 ms time of flight. From left to right are absorption images of $m_F = -1$, $m_F = 0$ and $m_F = +1$ state.

8.4 Microwave and rf System

In our experiments, there are transitions between the ground state $F = 1$ and $F = 2$ sublevels that cannot be induced by electric fields because they are electric dipole forbidden. However, oscillating magnetic fields can be used to interact with the magnetic dipole moment. For the sodium atomic ground state, magnetic dipole transitions between $F = 1$ and $F = 2$ state can be induced by microwaves (red, blue and green arrows in Fig. 8.13), and transitions between Zeeman sublevels within the same F state can be connected by rf fields (black arrows in Fig. 8.13).

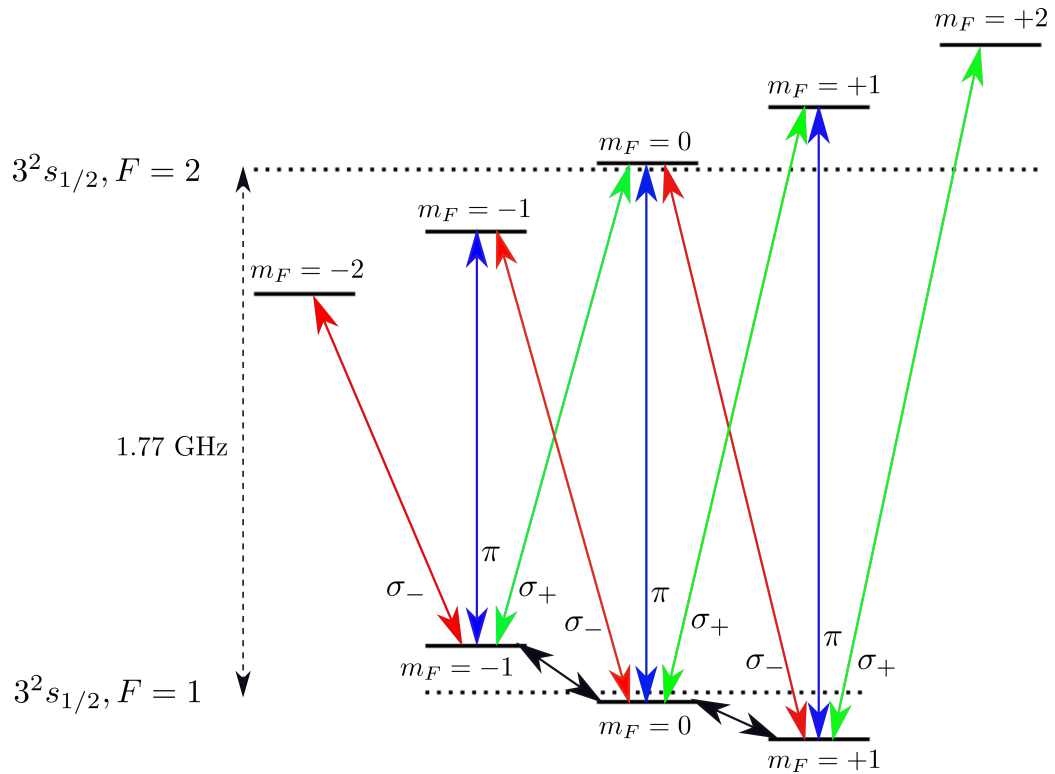


Figure 8.13: Schematic of microwave and rf transitions. Red, blue and green arrows represent microwave fields coupling to transitions between $F = 1$ and $F = 2$. Black arrows represent rf field coupling to transitions between $F = 1$ Zeeman sublevels.

In addition, the microwaves are also used for microwave-dressing to adjust the quadratic Zeeman energy, and therefore control the effective quadratic Zeeman shift

q during spin dynamics, as explained in Sec. 6.4. This requires the microwave field frequency, amplitude, and phase to be precisely controlled and changed quickly compared to the spin collisional time scale of milliseconds. We built a microwave system that meets all these requirements, with response times on the order of microseconds.

8.4.1 Signal Generation

The schematic of our home-built microwave system is shown in Fig. 8.14. The FPGA board receives control signals from a computer. As it steps through the timing sequence, it sends commands to a direct-digital synthesis chip (Diybigworld AD9954 DDS DWORLDS-2DS63) to create a sine wave with specified frequency, amplitude and phase. The frequency of this sine wave is tuned between 29 and 30 MHz in our experiments. This low-frequency sine wave from the DDS is mixed with a constant high frequency signal of about 1.7416 GHz from a stable function generator (Hewlett Packard HP8057B). The mixing is done by a single-sideband modulator (Polyphase Microwave SSB0622A) which passes the sum of the two input frequencies, resulting in the desired microwave signal which is close to the sodium ground state hyperfine splitting. The detuning, intensity and phase of the signal can be conveniently controlled by the FPGA while keeping the HP function generator at a fixed output. The desired sine wave signal is then sent to a microwave amplifier with a maximum output power of 20 W (HD Communication HD 28747) and applied to the atoms through a home-built antenna. The details of the microwave design are presented in Ref. [122], where I was the co-author.

The design of the rf generation is relatively simple in comparison to the microwave generation. The rf signal is generated by a function generator (Agilent 33220A), amplified to 25 W, and then radiated to atoms via a home-built rf coil placed inside the vacuum chamber, which is close to atoms. Fig. 8.15 shows the schematic of our rf

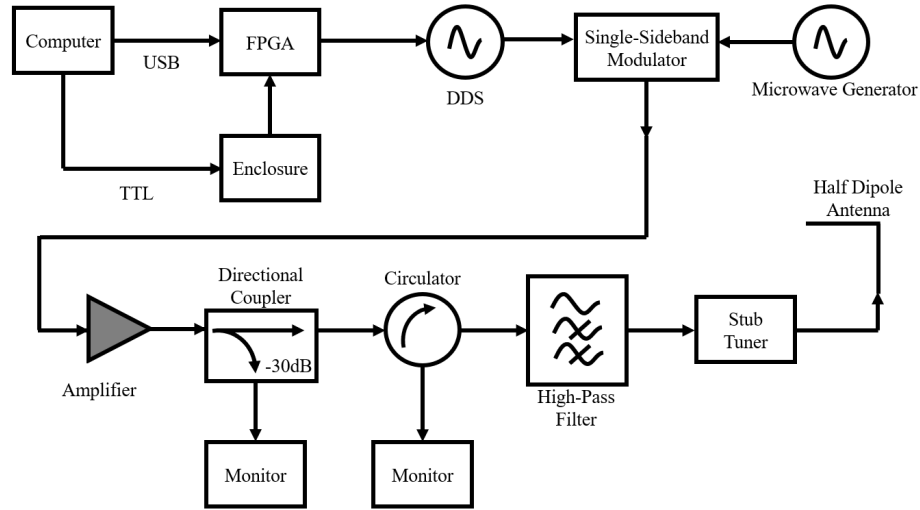


Figure 8.14: Schematic of microwave system. The output signal can be controlled remotely on a computer. The FPGA receives data packets and sends input parameters to the DDS, which generates a high-speed tunable sine wave signal at frequencies around 30 MHz. The low frequency sine wave is mixed with a stable, high frequency (~ 1.74 GHz) sine wave via a single-sideband modulator to generate the desired sum frequency (~ 1.77 GHz) sine wave, which is close to the hyperfine splitting of the sodium ground state. After amplification, filtering, and impedance matching, the signal is then emitted from a half-dipole antenna to irradiate trapped cold atoms. FPGA: field programmable gate array. DDS: direct digital synthesizer. SSB: single-sideband modulator. TTL: transistor-transistor logic.

design, built using off-the shelf parts from Mini Circuits. The required frequency for the rf transitions in our experiments depends on the magnetic field, because it has to be resonant with the linear Zeeman shift. For the typical magnetic field used in our experiments, the rf frequency is tuned to 300 kHz.

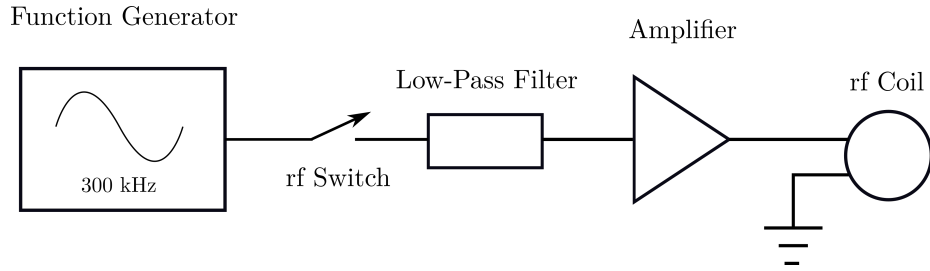


Figure 8.15: Schematic of rf system. The rf signal generated from a function generator is filtered by a low-pass filter before passing through the rf amplifier. A home-built rf coil antenna is installed inside the vacuum chamber so that it is close to the atoms and therefore can induce strong interactions.

8.4.2 Antenna

A strong microwave field is required in our spinor BEC experiments because it allows us to tune the effective quadratic Zeeman shift over a large range from about -300 kHz to +300 kHz to control the spin-mixing collisions and apply a quick phase shift for spin-mixing interferometry. In order to maximize the intensity of microwave radiation at the position of the BEC, I designed and built a half-dipole antenna that is installed inside the vacuum chamber such that it is closer to the atoms that are being radiated. In order to have a good radiation efficiency, the size of the antenna needs to match the wavelength. The microwave field is at a frequency of about 1.8 GHz, which corresponds to a wavelength of $\lambda = 1/6$ m. In addition, the antenna inside the vacuum chamber is not allowed to block any laser beams, such as the MOT beams and imaging beams. Considering the geometric constraints in the chamber, we choose a half-dipole antenna design, which has a length of a quarter of the wavelength $\lambda/4 = 4.2$ cm.

The half-dipole antenna is mounted inside the vacuum chamber, approximately 3 cm away from the atomic cloud, via an electrical feedthrough (Kurt J. Lesker IFTCG012012), as shown in Fig. 8.16. The antenna is made of UHV compatible copper wire and connected to the electrical feedthrough by UHV compatible Kapton

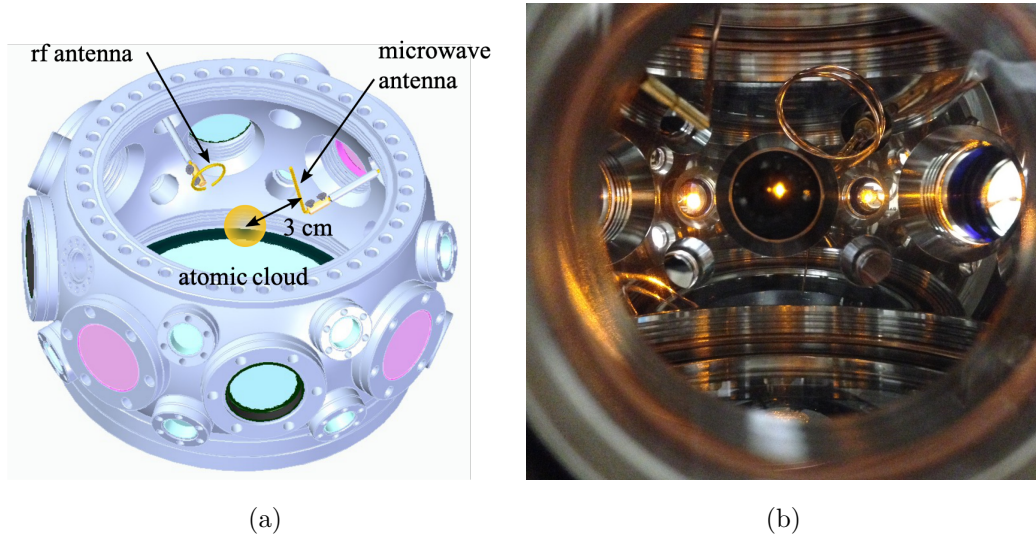


Figure 8.16: (a) CAD rendering of the microwave and rf antennas mounted inside the vacuum chamber. The microwave antenna is a half-dipole antenna and mounted about 3 cm from the center of trapped atoms inside the vacuum chamber via an electrical feedthrough. The rf antenna is a small copper loop with diameter of 25 mm, and it is also installed close to the center of the atomic cloud to improve the rf intensity at the position of the atomic cloud. (b) A photo of the chamber showing microwave and rf antennas.

coax wire (Kurt J. Lesker FTAKC060CM1). Inline barrel connectors are used to provide reliable, UHV compatible electrical connection between the copper antenna and the coax wire. The half-dipole antenna radiates the microwave field equally in all azimuthal directions. Therefore, we oriented our antenna parallel to the atoms, which is located at the center of the chamber, to maximize the effect of the radiation on the atoms.

The rf signal has a frequency on the order of hundreds of kHz, corresponding to a wavelength $\lambda \approx 1000$ m, so it is impossible to make a wavelength size antenna in the lab. The rf antenna is designed as a 25-mm diameter loop antenna built out of copper wire. It is also mounted inside the vacuum chamber via an electrical feedthrough

to be close to the atoms. The loop antenna has a lower efficiency compared to a wavelength size antenna, but the rf signal is usually applied during the initial state preparation stage, tuned onto resonance, and a strong field is therefore not required. It has been tested experimentally in our lab that the small loop antenna is able to generate an effective population transfer between Zeeman sublevels, a full population transfer between $m_F = -1$ and $m_F = +1$ can be done within $80 \mu\text{s}$.

8.5 Control System

Our experiments require computer control to provide precise control as well as analog signals for various components, such as AOMs, optical shutters, rf switches and camera triggers. Our experimental timing sequences are controlled by a LabVIEW program via a Spincore PulseBlaster PCI card which provides 24 digital channels and two National Instruments DAQ cards with 8 analog channels each. A LabVIEW program was developed to give precise, high-speed control over necessary devices during experimental sequences with a time resolution of 10 ns, owing to the excellent timing provided by the Pulseblaster card, which was originally designed for demanding nuclear-magnetic resonance experiments. We use two computers for our experiments, one computer controls timing sequences via LabVIEW. The collected data is sent to the second computer for analysis via Igor. The Igor program on the data analysis computer can receive and analyze experimental data automatically to obtain the desired information, such as atom number, atomic cloud size, and temperature. The experimental timing sequences can be loaded into our LabVIEW program and run automatically for several hours, with all the data analyzed and stored by the Igor program. Fig. 8.17 shows an example panel of our LabVIEW interface that controls all the 24 digital channels and 16 analog channels. An arbitrary amount of such panels are stacked vertically to program a timing sequence. Each panel can correspond to a

time period between $10 \mu\text{s}$ and several seconds.

A full typical sequence consisting of MOT loading, polarization gradient cooling, transferring to dipole trap, evaporative cooling to BEC, spin-mixing experiment, and imaging takes about 25 seconds. It is automatically repeated as parameter is scanned.

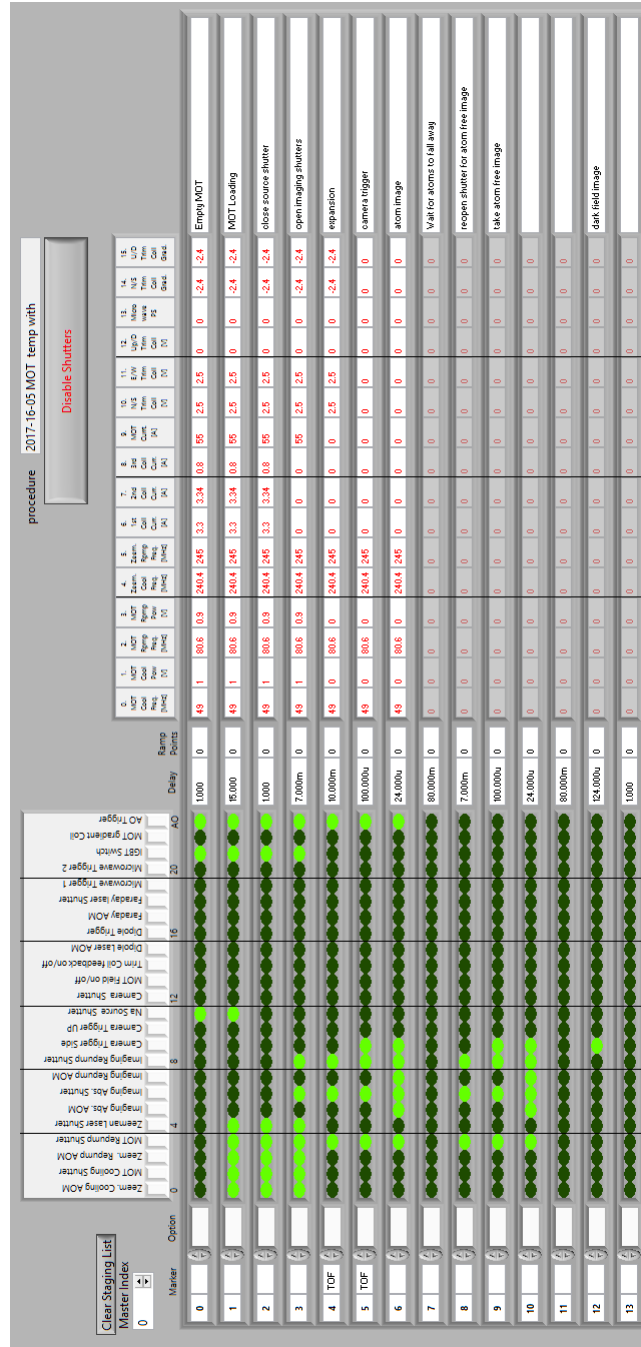


Figure 8.17: A control panel of the LabVIEW interface. There are 24 digital channels with green circles as on/off switches. Bright green represents status on while dark green represents off. There are also 16 analog channels with input boxes. These panels are stacked vertically to create any desired timing sequence, with time increasing towards the bottom.

Chapter 9

Experimental Results of Spinor BECs

In this chapter, I present our experimental results in creating a sodium spinor BEC, controlling spin dynamics and implementing matter-wave interferometry based on spinor BECs. We introduce the sequences to create sodium BECs with about 3×10^4 atoms in an all-optical system. We control the spin-exchange dynamics by rf seeding of the initial state and microwave dressing. The controllable spin dynamics could be used to implement a nonlinear interferometer with quantum-enhanced phase sensitivities in the future.

9.1 Creating BECs in an All-Optical System

The computer control of our experimental apparatus allows us to experimentally optimize the cooling sequence until a BEC is achieved. Fig. 9.1 shows a typical optimized sequence to create a sodium BEC in an all-optical system. After preliminary cooling in the MOT, an atomic cloud with about 3×10^8 trapped sodium atoms are at a temperature typically around 1 mK in the center of our chamber. We further cool the gas via polarization gradient cooling [123] in a short optical molasses phase (~ 30 ms) to a temperature of $\sim 70 \mu\text{K}$. The difference between the optical molasses and the MOT phase is the absence of the magnetic field gradient. Atoms in the center region of the optical molasses are then transferred into the optical dipole trap (ODT). In our experiment, the ODT is turned on during the MOT loading stage. After the optical molasses phase, there is a one-second free evaporation period inside the dipole trap, during which the MOT beams and magnetic field gradient are off. We then raise the ODT to its highest available power within 5 ms during the one-second free evaporation to create a deeper trap potential U_{dip} , see Eq. (6.19), which can capture more atoms

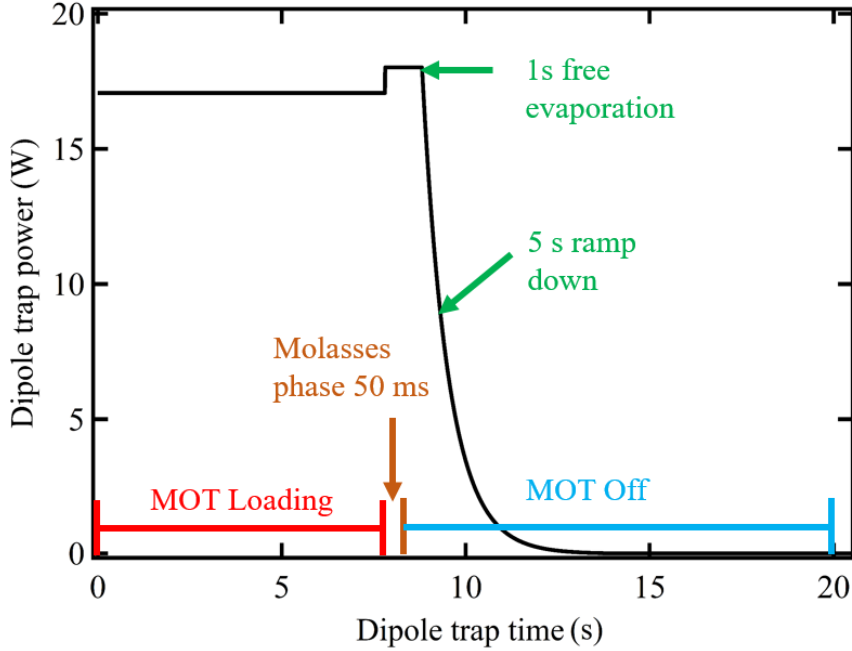


Figure 9.1: Empirically optimized experimental dipole trap ramping sequence. The ODT is kept at constant power during the loading phase. It then ramps to its maximum power for a one-second long free evaporation period. Finally, there is a forced evaporation cooling phase where the trap intensity is reduced exponentially until a BEC is formed.

because it captures atoms with larger kinetic energies. Fig. 9.2a and Fig. 9.2b are false color absorption images of our crossed dipole trap from a top-down view with 10 ms and 500 ms free evaporation, respectively. During the free evaporation, the most energetic atoms escape from the dipole trap due to the absence of MOT trapping, and the temperature of the trapped atomic gas is reduced via re-thermalization. After free evaporation, we are able to capture $\sim 3 \times 10^5$ cold sodium atoms in the ODT with $U_{\text{dip}} \approx k_B \times 980 \mu\text{K}$.

To finally achieve a BEC, forced evaporative cooling is applied. Forced evaporative cooling can be simply performed by reducing the dipole trap potential U_{dip} , e.g, lowering the dipole trap beam power [124, 125]. In this process, hot atoms are lost from the trap and the rethermalization of the remaining atoms leads to a lower temperature.

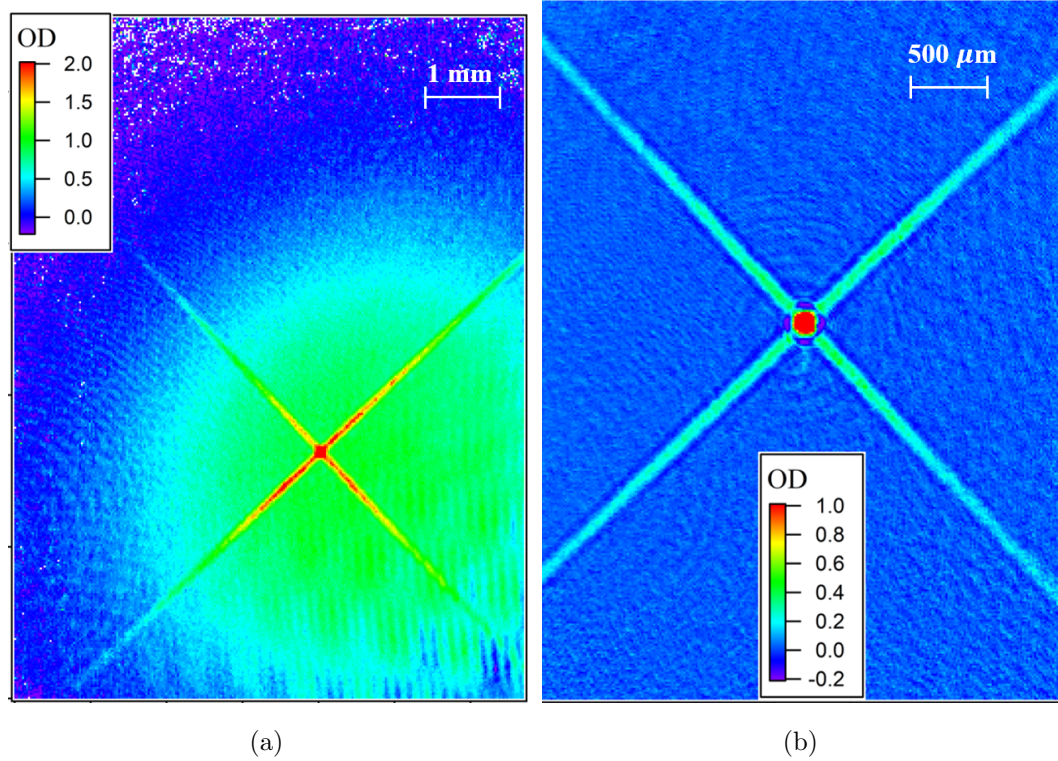


Figure 9.2: Top view absorption images of ODT. (a) A typical image of our crossed ODT in the presence of MOT atoms at the beginning of free evaporation phase. (b) A typical image of ODT after one-second free evaporation, after most MOT atoms escaped. OD: optical density.

Fig. 9.3 shows false color absorption images taken during the forced evaporation cooling period. As the ODT power ramps down successively, hot thermal atoms escape from the trap and the atomic cloud temperature reduces. Once the critical temperature is reached, a BEC appears inside the cloud, which can be determined from the absorption image by a sharp density peak. As the ODT power continuously ramp down, all the thermal atoms are gone and only the pure BEC remains in the trap. After the exponential ramping down of the ODT laser power from ~ 20 W to ~ 200 mW during the 5-second forced evaporative cooling period, a pure $F = 1$ BEC with 3×10^4 sodium atoms at a temperature around 60 nK is created.

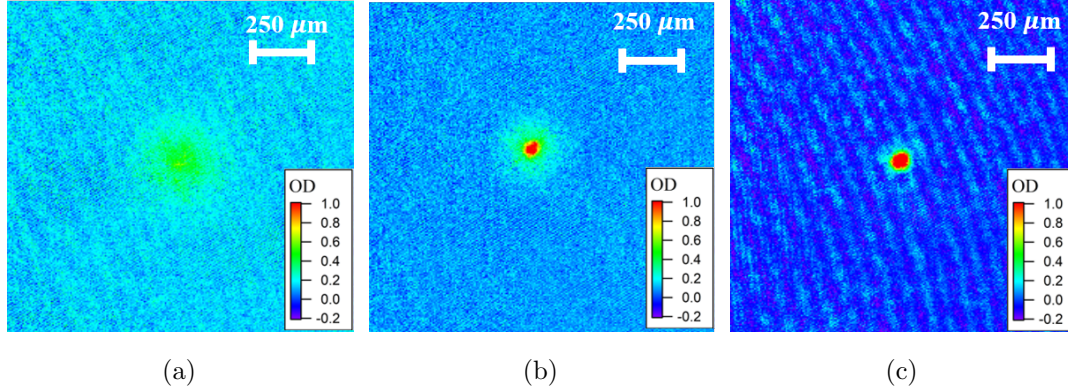


Figure 9.3: Absorption images taken during the forced evaporative cooling process. The ODT power decreases from (a) to (c). (a) Hot atoms are escaping from the trap and the atomic cloud temperature is reducing. (b) The BEC appears at the center as a sharp density peak. (c) The thermal atoms are escaping from the trap and the BEC fraction is increasing. Finally, a nearly pure BEC is achieved. OD: optical density.

9.2 Initial State Preparation

Sodium BECs produced after forced evaporative cooling are distributed in three spin states: $m_F = -1$, $m_F = 0$ and $m_F = +1$. To change the spin populations, we can apply a magnetic field gradient and magnetic bias field during the evaporative cooling. By applying appropriate fields which we determine empirically via trial and error, the BEC atoms could be nearly fully allocated into any of the spin states, for example, $|F = 1, m_F = 0\rangle$. We then use two microwave sweeps to adiabatically transfer any residual atoms in $|F = 1, m_F = \pm 1\rangle$ states to $F = 2$ state followed by 1 ms long clean-up pulses of resonant $F = 2 \rightarrow F'$ light that kick all the $F = 2$ atoms out of the trap, to get a pure $|F = 1, m_F = 0\rangle$ BEC. Atoms in $|F = 1, m_F = 0\rangle$ state can then be transferred into $|F = 1, m_F = \pm 1\rangle$ states in a controlled way by applying a resonant rf pulse. In this way, we can prepare an initial state with combination of spin states by adjusting the amplitude and duration of the rf pulse. The rf seeding pulse provides us the ability to start the spin evolution with any seeding percentage,

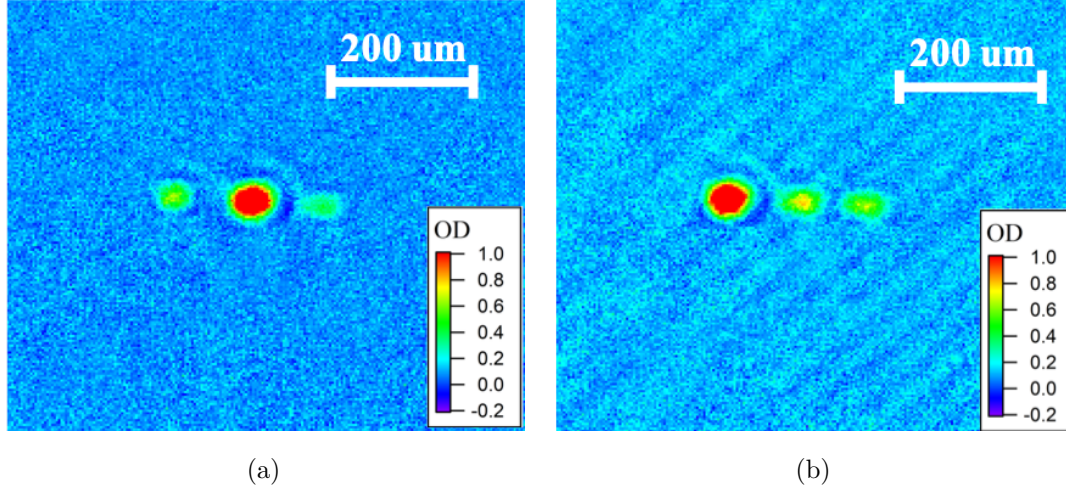


Figure 9.4: Stern-Gerlach absorption images of sodium atoms in three spin states. (a) and (b) show different spin populations in the three spin states due to different applied rf pulses. The rf pulse amplitude and duration are chosen to transfer certain number of atoms.

for example, we can prepare initial state with 90% atoms in $|F = 1, m_F = 0\rangle$ state and 10% atoms in $|F = 1, m_F = \pm 1\rangle$ states. Fig. 9.4 shows the false color Stern-Gerlach absorption images of spin populations after applying different rf pulses during initial state preparation. Moreover, the rf resonant frequency is also used as a precise calibration measurement of the magnetic field.

In addition to rf seeding, microwaves can be used to prepare initial states. In this case, a sequence of four resonant pulses is used to transfer atoms from $|F = 1, m_F = 0\rangle$ to $|F = 1, m_F = \pm 1\rangle$. Microwave-dressing is used to quench the system and control the spin dynamics. As described in Sec. 6.4, precise calibration is necessary to calculate the microwave induced energy shift and the corresponding effective quadratic Zeeman shift q . Microwave calibrations are performed by applying a resonant microwave pulse between the $F = 1$ and $F = 2$ transitions and measuring the frequencies of the resulting Rabi oscillations, as shown in Fig. 9.5. In the shown calibration, our measured Rabi frequencies are $\Omega_{\sigma-} = 2\pi \times (11.7 \pm 0.3)$ kHz, $\Omega_{\pi} = 2\pi \times (4.1 \pm 0.2)$ kHz,

$\Omega_{\sigma+} = 2\pi \times (11.6 \pm 0.4)$ kHz. These Rabi frequencies are strong enough to tune the effective quadratic Zeeman shift q in a large range for control of evolution, and apply a quick phase shift within ~ 1 ms for spin-mixing interferometry. The calibration is performed usually multiple times per week.

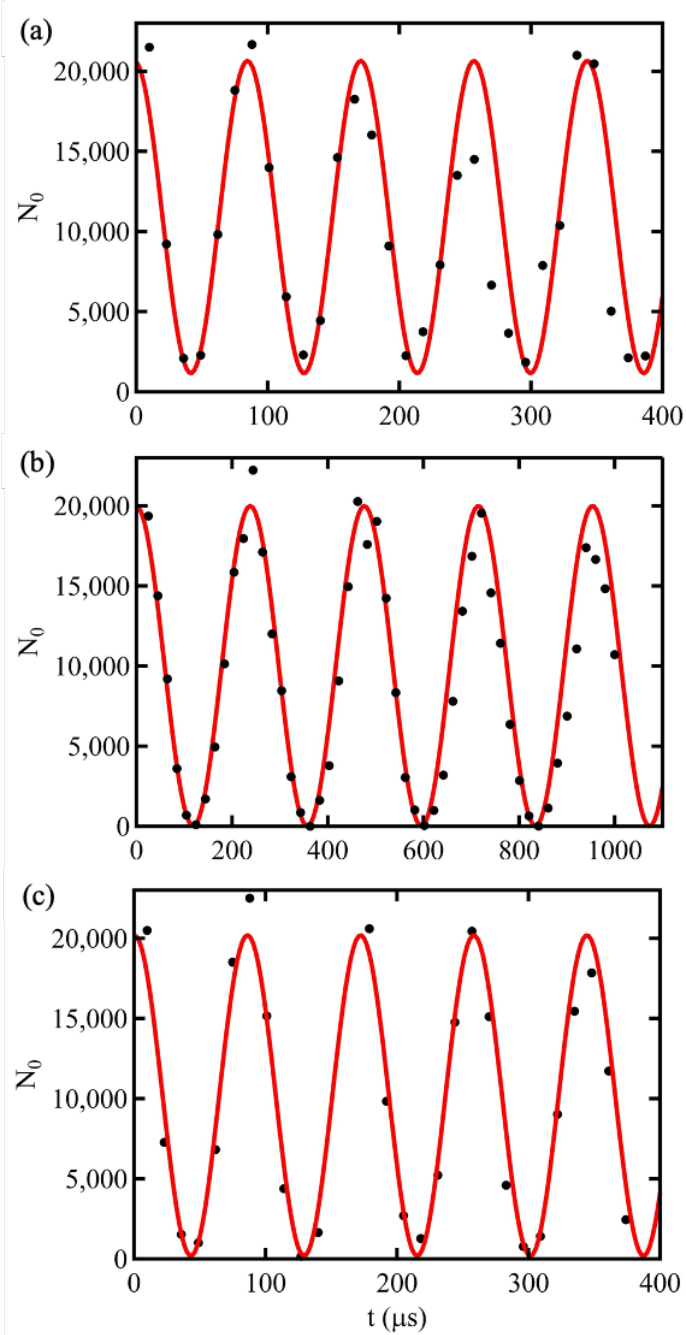


Figure 9.5: Rabi oscillations on resonance for (a) σ_- , (b) σ_π and (c) σ_+ transitions. Shown is the measured number of atoms (black circles) and a sinusoidal fit (red line) in $|F = 1, m_F = 0\rangle$ state versus microwave pulse duration. The fit is used to extract the Rabi frequency of Ω_{σ_-} , Ω_{σ_π} , Ω_{σ_+} . The measurements are done at the maximum microwave power of 20 W.

9.3 Microwave-Dressed Spin Evolutions

In order to study spin population evolutions due to spin-exchange collisions, we first prepare a pure BEC of about 20,000 atoms in a dipole trap, with all the atoms in the $m_F = 0$ state initially. We then apply a quick resonant rf pulse to transfer some atoms from the $m_F = 0$ state to the $m_F = \pm 1$ states as seeds. A constant background magnetic field B generated by the bias coils defines the quantization axis. Then an off-resonant, strong microwave field is immediately switched on within $5 \mu\text{s}$ to apply microwave dressing to apply a certain effective quadratic Zeeman shift q . The strong microwave field quenches the system, it drives the system out of equilibrium. The spin populations of the three m_F states now start to oscillate due to spin-exchange collisions. After a spin evolution time t , the microwave dressing is quickly turned off, and the populations in different spin states are then measured via Stern-Gerlach absorption imaging after 7 ms of time of flight.

We first investigate the effect of initial seeding on spin dynamics to show that we can control collisions by controlling the initial state. Fig. 9.6 shows spin oscillations starting with 2% and 8% initial seeds in $m_F = \pm 1$ states. We can see that introducing initial seeds increases the oscillation amplitude. Moreover, it also increases the oscillation frequency. Next, we also look at spin oscillations for different q values to show that we can control spin collisions by controlling q . As shown in Fig. 9.7, increasing $|q|$ from 0 to 15 Hz increases the speed of spin evolution.

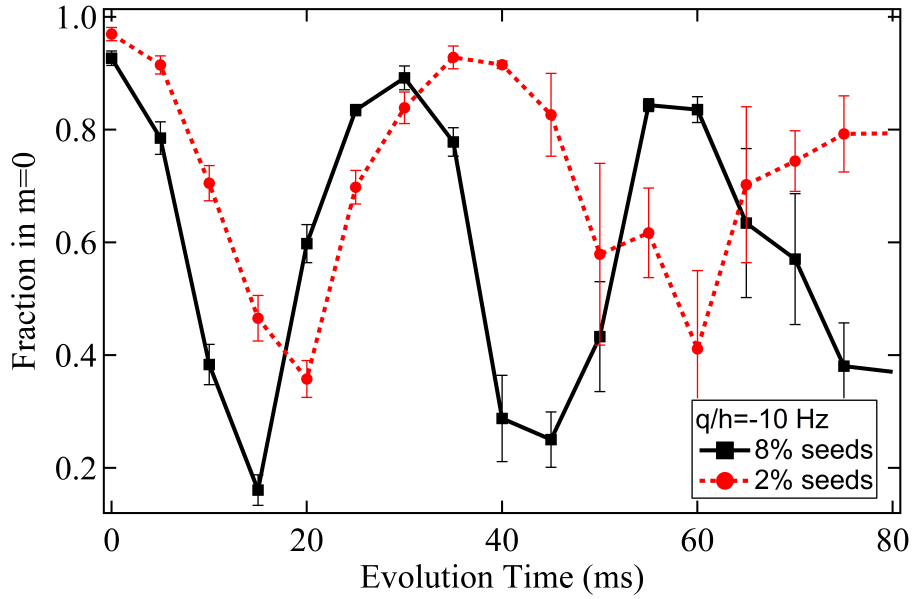


Figure 9.6: Spin oscillations at $q/h = -10$ Hz for 2% and 8% seeding in $m_F = \pm 1$ states. Each data point is an average of 5 measurements. Error bars are standard errors.

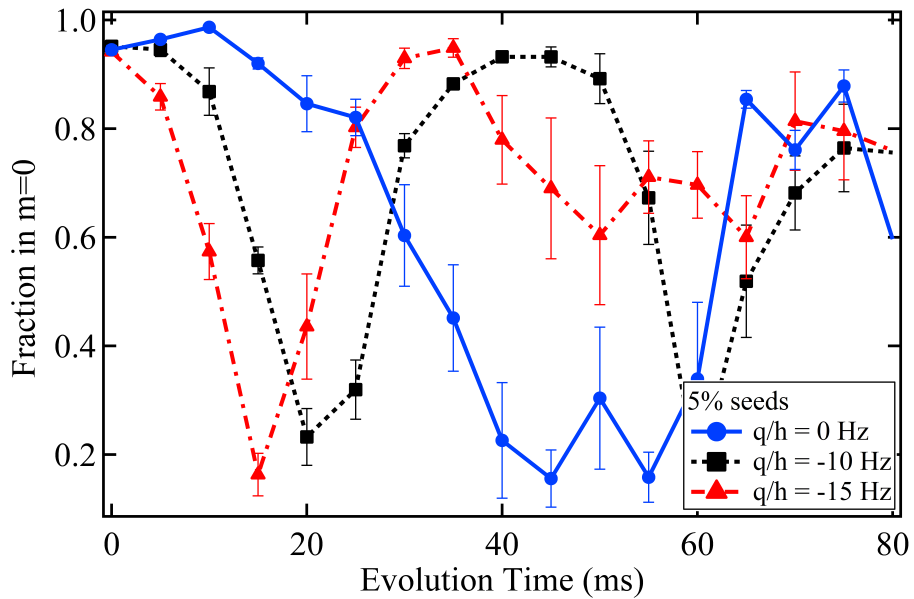


Figure 9.7: Spin oscillations at $q/h = 0$ Hz, $q/h = -10$ Hz, $q/h = -15$ Hz for 5% seeding in $m_F = \pm 1$ states. Each data point is an average of 5 measurements. Error bars are standard errors.

9.4 Matter-Wave Interferometry Based on Spinor BECs

With our initial state preparation techniques and microwave dressing, we are able to start from an initial spin state with arbitrary seeds and tune the spin-mixing dynamics. This enables us to implement a matter-wave interferometer based on spin-mixing dynamics on a $F = 1$ sodium spinor BEC in the regime of long evolution time and seeded initial states. The spin-exchange collisions in our spinor BEC can create entangled states of atoms in $|F = 1, m_F = \pm 1\rangle$, which can enhance the sensitivity of such an interferometer in spin space. We realize the interferometry with the sequences described in Sec. 6.5. We first prepare a pure $F = 1$ BEC with all atoms (about 20,000 in our experiment) in $m_F = 0$ state, then we seed a certain number of atoms into $m_F = \pm 1$ states using rf pulses. We apply microwave-dressing to tune the effective quadratic Zeeman shift q so that the spin evolution begins and quantum entangled atoms are generated. After a certain evolution time τ , we apply a strong, short ($t_{\text{rev}} \sim 1$ ms) microwave pulse to add a spinor phase shift to the system. After the phase shift, we let the system evolve for another time τ . Finally at $t = \tau + t_{\text{rev}} + \tau$, we measure the number of atoms in each spin state via Stern-Gerlach absorption imaging. Fig. 9.8 shows the simulated population evolution of $N_+ = N_{+1} + N_{-1}$ in a typical interferometry process with different microwave pulses applied at $\tau = 4$ ms with $t_{\text{rev}} = 0.25$ ms. This shows that the time evolution can be changed and even approximately reversed by applying an appropriate microwave pulse, in this case $q_{\text{rev}}/h = -625$ Hz. We measure the number of atoms at $t = \tau + t_{\text{rev}} + \tau = 8.25$ ms in each spin state as a function of applied phase shift φ , and this is called interferometer fringes. The interferometric phase sensitivity can be calculated using the measured atomic populations and the phase shift applied. We investigate spinor interferometry with various initial states, q , and evolution time τ .

Fig. 9.9 and Fig. 9.10 show our measured interferometer fringes, consisting of atomic

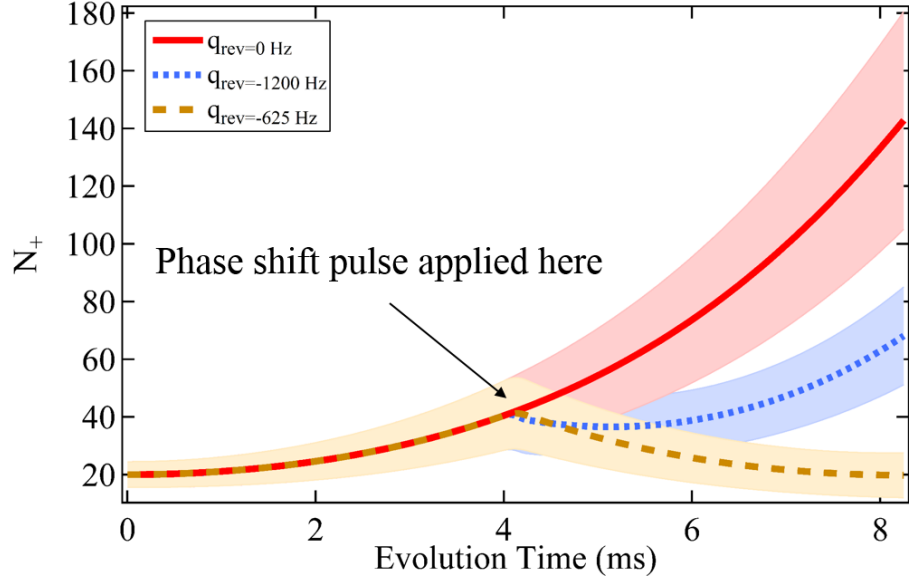


Figure 9.8: Evolution of $N_+ = N_{+1} + N_{-1}$ with microwave pulses applied at $\tau = 4$ ms, $q_{rev}/h = 0$ Hz (red, solid), $q_{rev}/h = -1,200$ Hz (blue, dotted) and $q_{rev}/h = -625$ Hz (yellow, dashed). Shaded region depicts $\pm\sigma_{N_+}$. Here $\langle N \rangle = 1,000$, 2% dual initial seeds, $c/h = 30$ Hz, and $t_{rev} = 0.25$ ms.

population fraction in the $m_F = 0$ state at $t = \tau + t_{rev} + \tau$, as a function of applied phase shift φ . For short evolution time, for example, $\tau = 3$ ms in Fig. 9.9, the interferometer fringe is sinusoidal and can be fitted by a sine wave function. But for longer evolution time, this is not the case. As seen in Fig. 9.10, for $\tau = 15$ ms, the interferometer fringe is highly non-sinusoidal. At some phase shifts φ , such as φ close to 0.5π , 1.5π and 2.5π , we observe sharp slopes which suggest a pathway towards enhanced phase sensitivities, because the fringes are highly sensitive to phase shift. The theoretical simulation (red line in Fig. 9.10), using the full quantum calculation, qualitatively agree with our measurements with some discrepancies due to extra noise in the experiments. Possible reasons for the discrepancies are: shot-to-shot atom number fluctuation, magnetic field fluctuation, temperature, humidity fluctuations and vibration in the lab, and other technical noise.

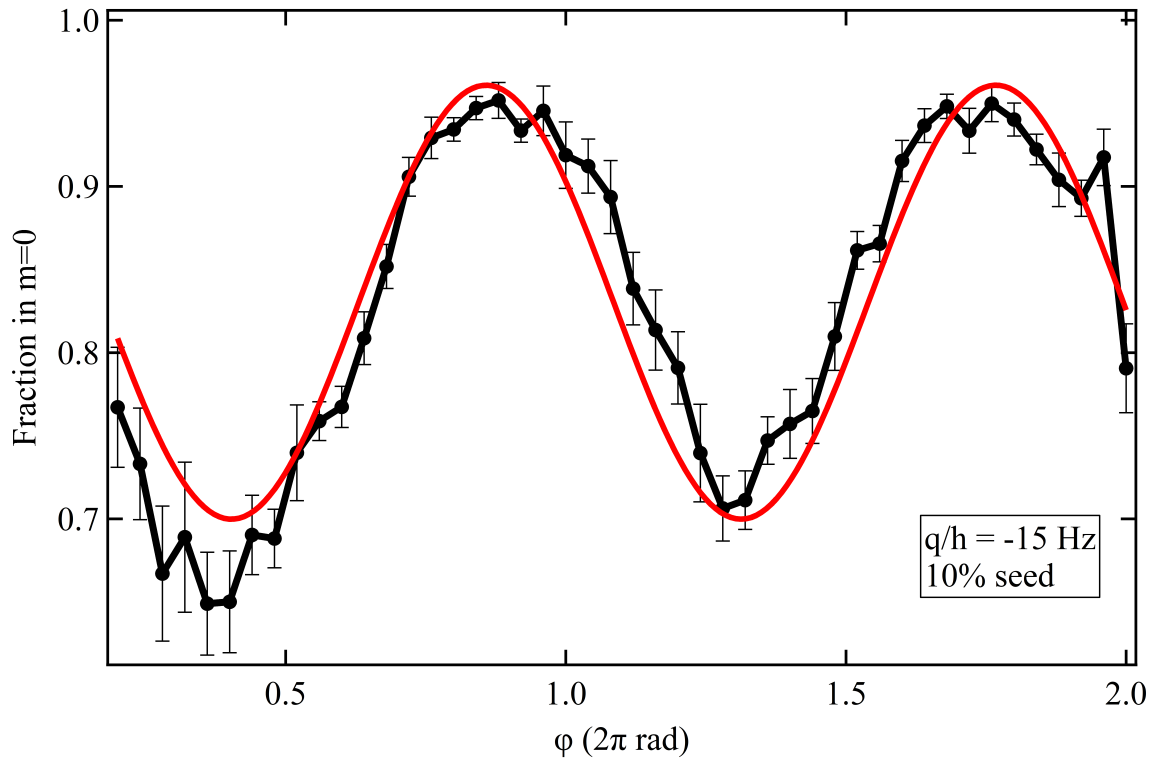


Figure 9.9: Sinusoidal interferometer fringe for evolution time $\tau = 3$ ms. Black circles are experimental data and red line is a sine wave fit. Each data point is an average of five measurements, with error bars represent standard errors. Here we use $q/h = -15$ Hz and 10% initial seeds. The total atom number is about 20,000.

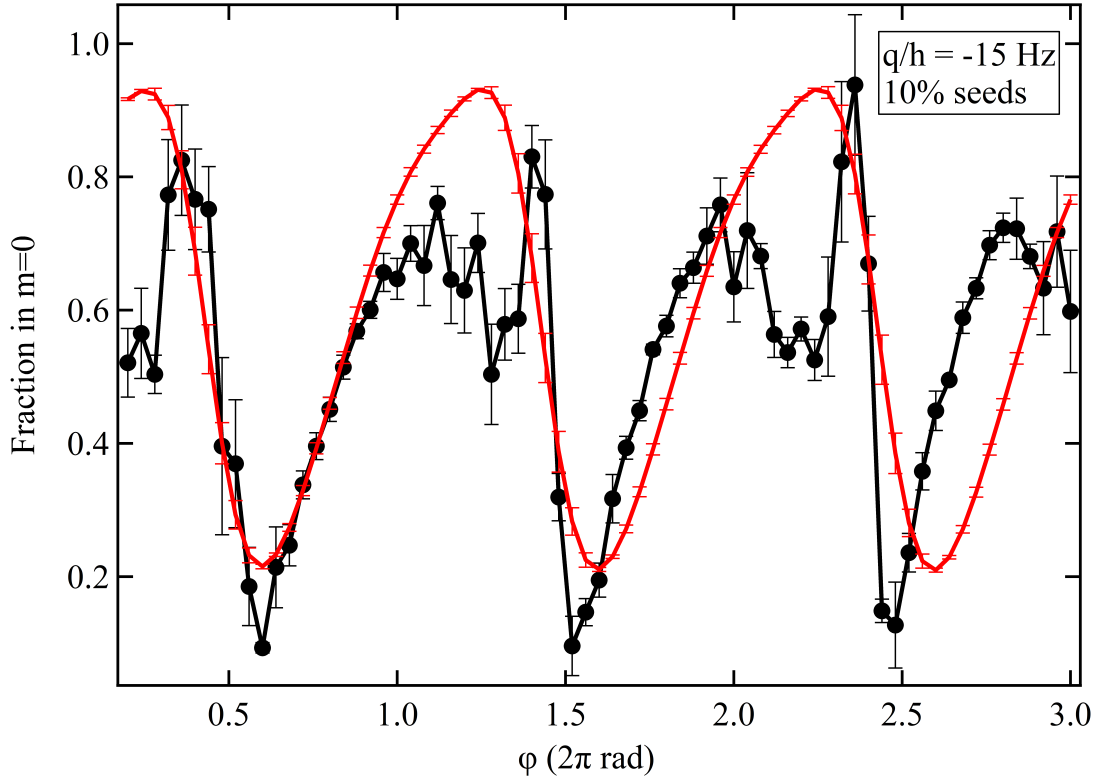


Figure 9.10: Non-sinusoidal interferometer fringe for evolution time $\tau = 15$ ms. Black circles are average data points of five measurements. The red dots are simulation results using full quantum calculation without adjustable parameters. Our measured results qualitatively agree with the simulations with some discrepancies. Error bars represent standard errors. Here we use $q/h = -15$ Hz and 10% initial seeds. The total atom number is about 20,000.

We also investigate the effect of q on the interferometer fringes. Fig. 9.11 shows our measured interferometer fringe for the same conditions as in Fig. 9.10, but with $q/h = -10$ Hz instead of $q/h = -15$ Hz. It also shows a non-sinusoidal fringe, but with different shape. Different q values change the fringe shapes, because different q lead to different spin dynamics.

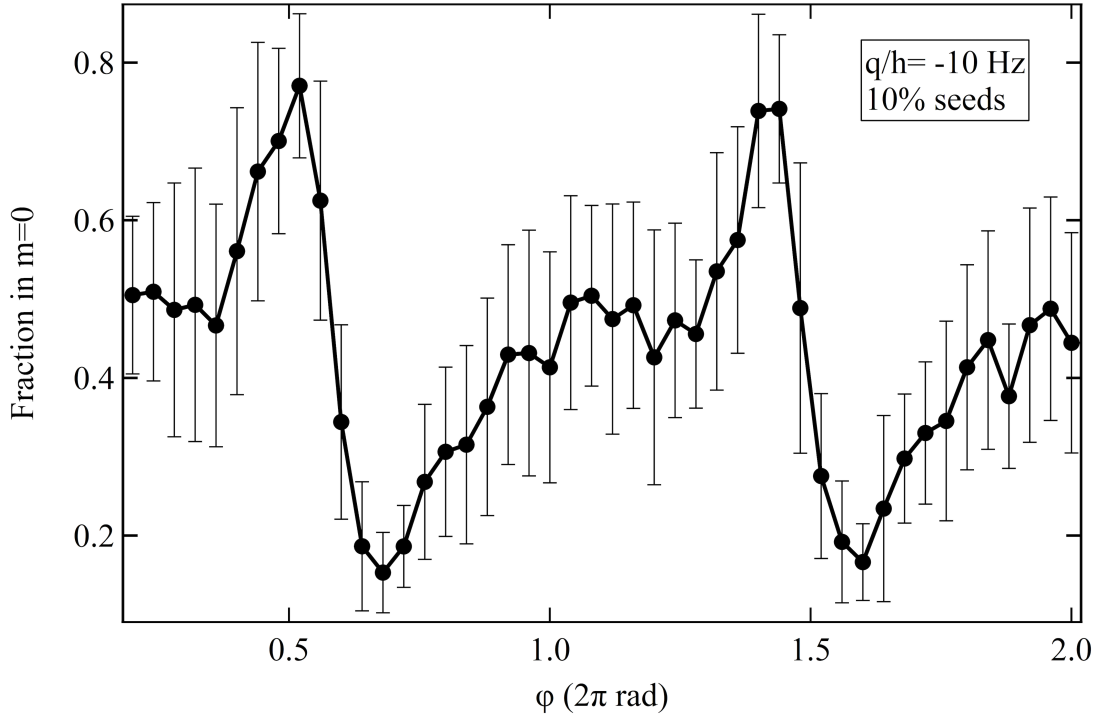


Figure 9.11: Interferometer fringe for evolution time $\tau = 15$ ms. Black circles are average data points of five measurements. Here we use $q/h = -10$ Hz, with all the other conditions the same as in Fig. 9.10.

To our knowledge, this is the first experimental investigation of the long-time evolution regime with seeded initial states for this type of interferometer.

9.5 Discussion and Outlook

We experimentally created sodium spinor BECs in an all-optical system. We are able to prepare initial states with different population distributions using magnetic fields and rf seeding. We demonstrated control over spin-exchange dynamics by microwave dressing. We implemented a quantum matter-wave interferometer based on nonlinear spin dynamics in our sodium spinor BECs. We also used our versatile home-built microwave system to apply quick phase shifts in the interferometry sequence [122]. We observed highly non-sinusoidal interference fringes which might indicate a pathway to enhanced sensitivities in the future.

Currently, our spin evolutions and interference fringes have large standard deviations, due to shot-to-shot fluctuation of atom number, vibrations, temperature fluctuations in the lab, humidity fluctuations and other technical sources of noise. We are working on reducing the number fluctuations in our BEC and dipole trap frequency fluctuations to improve the systematic uncertainties in our experimental setup. In the near future, the lab will move to a new state of the art research building next door on OU's campus, which houses the Center for Quantum Research and Technology. Many external parameters such as humidity, vibration, and temperature will be much better controlled in the new lab space, which should improve the error bars and reduce technical noise such as shot-to-shot number fluctuations. With these improvements, we expect to observe quantum-enhanced sensitivities in the near future.

Chapter 10

Conclusion and Outlook

The fundamental goal of this thesis was to generate entanglement between 589 nm photons for interfacing quantum-states of light with Na BECs and to generate entanglement between atoms in spinor Bose-Einstein condensates to investigate spin-mixing interferometry for quantum-enhanced sensing. The entangled twin-beam of light can be used in absorption imaging to detect the number of atoms in our sodium BECs with reduced noise. The entangled atoms in $m_F = \pm 1$ spinor states can be used to study matter-wave quantum optics in spin space.

We generated correlated states of light via a nonlinear optical process called four-wave mixing in hot sodium vapors. We have built an experimental system, where a strong pump beam and a weak probe beam derived from the main laser co-propagate through the sodium vapor cell with a small input angle θ . The glass sodium vapor cell is contained in a home-built oven whose temperature is controlled by band heaters and a PID controller. At the exit of the vapor cell, the seeding probe field is amplified and a new field called conjugate is generated with an angle θ respect to the pump beam. The power of the probe and conjugate, as well as their relative noise, are measured by a balanced detector. We solve the coupled differential equations under the approximation of slowly-varying amplitude and nearly co-propagating field to calculate the amplitude gains of the probe and conjugate fields. The results predict significant gain when parameters are adjusted well, without considering the residual Doppler shift, the large absorption and the spatial profile of the beams. We experimentally generated the twin beams of probe and conjugate via four-wave mixing on sodium with double- Λ configuration. We observed a probe gain of four, and a reduction of 2 dB on the relative intensity noise of the probe and conjugate field with respect to their individual

noises, suggesting that correlated photons were created. We observed twin-beam relative intensity noise very close to the shot noise limit, with only 1 dB above. We didn't observe quantum squeezing, which we attribute to the large absorption loss where entangled photons are lost, due to the Doppler broadened D_1 line and the low atomic density in Na vapor compared with Rb. We tested our home-built saturated absorption system to reduce the absorption loss and observed an average of 10% increase in the probe gain and 50% in the conjugate gain. We showed plan for a new stainless steel vapor cell to overcome the temperature limitation of the glass vapor cell. The new cell will allow us to dramatically increase the vapor temperature and thus increase the atomic density, which will lead to higher gain. With these improvements, it seems promising that quantum squeezing will be achieved.

In a second set of experiments, we studied entanglement generation via spin-mixing in Na spinor BECs. BECs with an internal spin degree of freedom, also called spinor BECs, offer rich opportunities to explore quantum dynamics since the spins can interact with each other to create entanglement, and the dynamics are controllable via external magnetic and microwave fields. We studied the spin-mixing dynamics, where quantum entanglement can be generated through spin-exchange collisions. We numerically investigate spin-mixing dynamics using quantum model and a semi-classical model (TWA). Both methods predict the atom population dynamics for non-seeded evolutions. For spin-mixing dynamics with seeded initial states, the TWA method was shown to not capture the quantum noise accurately. We numerically explored the atomic interferometry based on microwave-dressed $F = 1$ sodium spinor BECs. The simulation results predict that there are parameter regimes where the interferometry sensitivity can be enhanced. Moreover, our simulations show that quantum enhanced sensitivities can be obtained for large populations in the arms of the interferometer with seeded initial states, and long time evolution. We built

an all-optical system to create sodium Bose-Einstein condensates. We are able to prepare initial states with different population distributions, and we exert control over spin dynamics with a home-built versatile microwave source. We implemented matter-wave interferometry based on spin-mixing dynamics, and observed highly non-sinusoidal interference fringes suggesting a pathway towards quantum-enhanced sensitivities. To our knowledge, this is the first experimental investigation of seeded interferometry in spin space in the long evolution time limit. We are currently working on reducing standard deviations on the interferometer fringes, which might be due to the number fluctuations in BECs and the dipole trap frequency noise. With reduced systematic uncertainties in the experimental setup, quantum-enhanced sensitivities will be achievable via atomic interferometry.

Our next step would be applying the two-mode squeezed states of light generated via four-wave mixing in the absorption imaging to improve the atom number detection in BECs. In the future, light pulse interferometry based on $F = 1$ spinor BECs will also be studied using the versatile apparatus described in this thesis.

The versatile and reliable experimental apparatus I helped built during my Ph.D. research will allow future studies of new generation of quantum technologies based on quantum engineering of matter-waves, such as quantum-enhanced sensors for external fields with high spatial resolution, quantum-enhanced probes of ultracold atomic samples to measure spin populations with reduced noise, and quantum-enhanced matter-wave devices such as phase-sensitive amplifiers, similar to those known from quantum optics with light. The microwave-dressed spinor BEC system also has some significance for condensed matter physics, because it has analogies to the ac Josephson effect that is used in voltage standards and in superconducting quantum interference devices.

References

- [1] J. Betzwieser and et. al, “Quantum correlations between light and the kilogram-mass mirrors of LIGO,” *Nature* **583**, 43 (2020).
- [2] C. F. McCormick, A. M. Marino, V. Boyer, and P. D. Lett, “Strong low-frequency quantum correlations from a four-wave-mixing amplifier,” *Phys. Rev. A* **78**, 043816 (2008).
- [3] K. C. Cox, G. P. Greve, B. Wu, and J. K. Thompson, “Spatially homogeneous entanglement for matter-wave interferometry created with time-averaged measurements,” *Phys. Rev. A* **94**, 061601 (2016).
- [4] J. Estève, C. Gross, A. Weller, S. Giovanazzi, and M. K. Oberthaler, “Squeezing and entanglement in a Bose–Einstein condensate,” *Nature* **455**, 1216 (2008).
- [5] X.-Y. Luo, Y.-Q. Zou, L.-N. Wu, Q. Liu, M.-F. Han, M. K. Tey, and L. You, “Deterministic entanglement generation from driving through quantum phase transitions,” *Science* **355**, 620 (2017).
- [6] J. Hofmann, M. Krug, N. Ortegel, L. Gérard, M. Weber, W. Rosenfeld, and H. Weinfurter, “Heralded Entanglement Between Widely Separated Atoms,” *Science* **337**, 72 (2012).
- [7] T. van Leent, M. Bock, R. Garthoff, K. Redeker, W. Zhang, T. Bauer, W. Rosenfeld, C. Becher, and H. Weinfurter, “Long-Distance Distribution of Atom-Photon Entanglement at Telecom Wavelength,” *Phys. Rev. Lett.* **124**, 010510 (2020).
- [8] B. Hacker, S. Welte, S. Daiss, A. Shaukat, S. Ritter, L. Li, and G. Rempe, “Deterministic creation of entangled atom–light Schrödinger-cat states,” *Nat. Photonics* **13**, 110 (2019).
- [9] S. L. Braunstein and H. J. Kimble, “Teleportation of Continuous Quantum Variables,” *Phys. Rev. Lett.* **80**, 869 (1998).
- [10] R. C. Pooser and B. Lawrie, “Ultrasensitive measurement of microcantilever displacement below the shot-noise limit,” *Optica* **2**, 393 (2015).
- [11] M. Dowran, A. Kumar, B. J. Lawrie, R. C. Pooser, and A. M. Marino, “Quantum-enhanced plasmonic sensing,” *Optica* **5**, 628 (2018).
- [12] M. I. Kolobov and C. Fabre, “Quantum Limits on Optical Resolution,” *Phys. Rev. Lett.* **85**, 3789 (2000).
- [13] N. Treps, U. Andersen, B. Buchler, P. K. Lam, A. Maître, H.-A. Bachor, and C. Fabre, “Surpassing the Standard Quantum Limit for Optical Imaging Using Nonclassical Multimode Light,” *Phys. Rev. Lett.* **88**, 203601 (2002).

- [14] R. E. Slusher, L. W. Hollberg, B. Yurke, J. C. Mertz, and J. F. Valley, “Observation of Squeezed States Generated by Four-Wave Mixing in an Optical Cavity,” *Phys. Rev. Lett.* **55**, 2409 (1985).
- [15] L.-A. Wu, H. J. Kimble, J. L. Hall, and H. Wu, “Generation of Squeezed States by Parametric Down Conversion,” *Phys. Rev. Lett.* **57**, 2520 (1986).
- [16] A. Heidmann, R. J. Horowicz, S. Reynaud, E. Giacobino, C. Fabre, and G. Camy, “Observation of Quantum Noise Reduction on Twin Laser Beams,” *Phys. Rev. Lett.* **59**, 2555 (1987).
- [17] A. Dutt, K. Luke, S. Manipatruni, A. L. Gaeta, P. Nussenzveig, and M. Lipson, “On-Chip Optical Squeezing,” *Phys. Rev. Applied* **3**, 044005 (2015).
- [18] X. Guo, X. Li, N. Liu, L. Yang, and Z. Y. Ou, “An all-fiber source of pulsed twin beams for quantum communication,” *Appl. Phys. Lett.* **101**, 261111 (2012).
- [19] C. F. McCormick, V. Boyer, E. Arimondo, and P. D. Lett, “Strong relative intensity squeezing by four-wave mixing in rubidium vapor,” *Opt. Lett.* **32**, 178 (2007).
- [20] P. G. Kwiat, K. Mattle, H. Weinfurter, A. Zeilinger, A. V. Sergienko, and Y. Shih, “New High-Intensity Source of Polarization-Entangled Photon Pairs,” *Phys. Rev. Lett.* **75**, 4337 (1995).
- [21] M. H. Rubin, D. N. Klyshko, Y. H. Shih, and A. V. Sergienko, “Theory of two-photon entanglement in type-II optical parametric down-conversion,” *Phys. Rev. A* **50**, 5122 (1994).
- [22] A. Einstein, “Quantentheorie des einatomigen idealen Gases: Zweite Abhandlung,” *Preuss. Akad. Wiss.* **1**, 3 (1925).
- [23] S. N. Bose, “Plancks Gesetz und Lichtquantenhypothese,” *Z. Phys.* **26**, 178 (1924).
- [24] M. H. Anderson, J. R. Ensher, M. R. Matthews, C. E. Wieman, and E. A. Cornell, “Observation of Bose-Einstein Condensation in a Dilute Atomic Vapor,” *Science* **269**, 198 (1995).
- [25] K. B. Davis, M. O. Mewes, M. R. Andrews, N. J. van Druten, D. S. Durfee, D. M. Kurn, and W. Ketterle, “Bose-Einstein Condensation in a Gas of Sodium Atoms,” *Phys. Rev. Lett.* **75**, 3969 (1995).
- [26] C. C. Bradley, C. A. Sackett, and R. G. Hulet, “Bose-Einstein Condensation of Lithium: Observation of Limited Condensate Number,” *Phys. Rev. Lett.* **78**, 985 (1997).

- [27] D. M. Stamper-Kurn, M. R. Andrews, A. P. Chikkatur, S. Inouye, H.-J. Miesner, J. Stenger, and W. Ketterle, “Optical Confinement of a Bose-Einstein Condensate,” *Phys. Rev. Lett.* **80**, 2027 (1998).
- [28] M. R. Andrews, C. G. Townsend, H.-J. Miesner, D. S. Durfee, D. M. Kurn, and W. Ketterle, “Observation of Interference Between Two Bose Condensates,” *Science* **275**, 637 (1997).
- [29] B. P. Anderson and M. A. Kasevich, “Macroscopic Quantum Interference from Atomic Tunnel Arrays,” *Science* **282**, 1686 (1998).
- [30] M. Albiez, R. Gati, J. Fölling, S. Hunsmann, M. Cristiani, and M. K. Oberthaler, “Direct Observation of Tunneling and Nonlinear Self-Trapping in a Single Bosonic Josephson Junction,” *Phys. Rev. Lett.* **95**, 010402 (2005).
- [31] M. Greiner, O. Mandel, T. Esslinger, T. W. Hänsch, and I. Bloch, “Quantum phase transition from a superfluid to a Mott insulator in a gas of ultracold atoms,” *Nature* **415**, 39 (2002).
- [32] E. V. Goldstein and P. Meystre, “Quantum theory of atomic four-wave mixing in Bose-Einstein condensates,” *Phys. Rev. A* **59**, 3896 (1999).
- [33] Z. Zhang and L.-M. Duan, “Generation of Massive Entanglement through an Adiabatic Quantum Phase Transition in a Spinor Condensate,” *Phys. Rev. Lett.* **111**, 180401 (2013).
- [34] S. L. Braunstein and P. van Loock, “Quantum information with continuous variables,” *Rev. Mod. Phys.* **77**, 513 (2005).
- [35] P. D. Lett, N. Corzo, A. Marino, and K. Jones, “Quantum Imaging with light from Four-Wave Mixing,” *Optical Society of America T4A.3* (2013).
- [36] M. I. M. A. Khudus, F. De Lucia, C. Corbari, T. Lee, P. Horak, P. Sazio, and G. Brambilla, “Phase matched parametric amplification via four-wave mixing in optical microfibers,” *Opt. Lett.* **41**, 761 (2016).
- [37] C. Gerry and P. Knight, *Introductory Quantum Optics* (Cambridge University Press, Cambridge, England, UK, 2004).
- [38] P. Berman and V. Malinovsky, *Principles of Laser Spectroscopy and Quantum Optics* (Princeton University Press, Princeton, NJ, USA, 2010).
- [39] D. F. Walls, “Squeezed states of light,” *Nature* **306**, 141 (1983).
- [40] R. W. Boyd, *Nonlinear Optics* (Elsevier, Academic Press, Cambridge, MA, USA, 2003).

- [41] Q. Glorieux, L. Guidoni, S. Guibal, J.-P. Likforman, and T. Coudreau, “Strong quantum correlations in four wave mixing in 85Rb vapor,” *Quantum Opt.* **7727**, 772703 (2010).
- [42] C. F. McCormick, V. Boyer, E. Arimondo, and P. D. Lett, “Strong relative intensity squeezing by four-wave mixing in rubidium vapor,” *Opt. Lett.* **32**, 178 (2007).
- [43] M. D. Lukin, P. R. Hemmer, M. Löffler, and M. O. Scully, “Resonant Enhancement of Parametric Processes via Radiative Interference and Induced Coherence,” *Phys. Rev. Lett.* **81**, 2675 (1998).
- [44] M. T. Turnbull, P. G. Petrov, C. S. Embrey, A. M. Marino, and V. Boyer, “Role of the phase-matching condition in nondegenerate four-wave mixing in hot vapors for the generation of squeezed states of light,” *Phys. Rev. A* **88**, 033845 (2013).
- [45] D. A. Steck, *Sodium D Line Data*, 2019.
- [46] M. Jasperse, “Relative Intensity Squeezing by Four-Wave Mixing in Rubidium,” Ph.D. thesis, University of Melbourne, 2010.
- [47] C. Foot, *Atomic Physics, Oxford Master Series in Physics* (OUP Oxford, Oxford, 2004).
- [48] D. A. Steck, *Rubidium 85 D Line Data*, 2019.
- [49] S. Wildermuth, S. Hofferberth, I. Lesanovsky, E. Haller, L. M. Andersson, S. Groth, I. Bar-Joseph, P. Krüger, and J. Schmiedmayer, “Microscopic magnetic-field imaging,” *Nature* **435**, 440 (2005).
- [50] C. Gross, T. Zibold, E. Nicklas, J. Estève, and M. K. Oberthaler, “Nonlinear atom interferometer surpasses classical precision limit - Nature,” *Nature* **464**, 1165 (2010).
- [51] J. P. Wrubel, A. Schwettmann, D. P. Fahey, Z. Glassman, H. K. Pechkis, P. F. Griffin, R. Barnett, E. Tiesinga, and P. D. Lett, “Spinor Bose-Einstein-condensate phase-sensitive amplifier for SU(1,1) interferometry,” *Phys. Rev. A* **98**, 023620 (2018).
- [52] F. Dalfovo, S. Giorgini, L. P. Pitaevskii, and S. Stringari, “Theory of Bose-Einstein condensation in trapped gases,” *Rev. Mod. Phys.* **71**, 463 (1999).
- [53] C. C. Bradley, C. A. Sackett, J. J. Tollett, and R. G. Hulet, “Evidence of Bose-Einstein Condensation in an Atomic Gas with Attractive Interactions,” *Phys. Rev. Lett.* **75**, 1687 (1995).

- [54] S. Chu, “Nobel Lecture: The manipulation of neutral particles,” *Rev. Mod. Phys.* **70**, 685 (1998).
- [55] C. N. Cohen-Tannoudji, “Nobel Lecture: Manipulating atoms with photons,” *Rev. Mod. Phys.* **70**, 707 (1998).
- [56] W. D. Phillips, “Nobel Lecture: Laser cooling and trapping of neutral atoms,” *Rev. Mod. Phys.* **70**, 721 (1998).
- [57] E. A. Cornell and C. E. Wieman, “Nobel Lecture: Bose-Einstein condensation in a dilute gas, the first 70 years and some recent experiments,” *Rev. Mod. Phys.* **74**, 875 (2002).
- [58] W. Ketterle, “Nobel lecture: When atoms behave as waves: Bose-Einstein condensation and the atom laser,” *Rev. Mod. Phys.* **74**, 1131 (2002).
- [59] M. L. Harris, “Realisation of a cold mixture of rubidium and caesium,” Ph.D. thesis, Durham University, 2008.
- [60] W. Ketterle, D. S. Durfee, and S. D. M. Kurn, in *Making, probing and understanding Bose-Einstein condensates*, edited by M. Inguscio, S. Stringari, and C. Wieman (IOS Press, Amsterdam, 1999), Vol. 140.
- [61] K. Huang, *Statistical Mechanics* (Wiley, New York, 1963).
- [62] D. M. Stamper-Kurn and M. Ueda, “Spinor Bose gases: Symmetries, magnetism, and quantum dynamics,” *Rev. Mod. Phys.* **85**, 1191 (2013).
- [63] Y. Kawaguchi and M. Ueda, “Spinor Bose–Einstein condensates,” *Phys. Rep.* **520**, 253 (2012).
- [64] D. M. Stamper-Kurn and W. Ketterle, *Coherent atomic matter waves* (Springer, Berlin, Germany, 2001), pp. 139–217.
- [65] M.-S. Chang, “Coherent spin dynamics of a spin-1 Bose-Einstein condensate,” Ph.D. thesis, Georgia Institute of Technology, 2006.
- [66] S. Knoop, T. Schuster, R. Scelle, A. Trautmann, J. Appmeier, M. K. Oberthaler, E. Tiesinga, and E. Tiemann, “Feshbach spectroscopy and analysis of the interaction potentials of ultracold sodium,” *Phys. Rev. A* **83**, 042704 (2011).
- [67] C. Klempt, O. Topic, G. Gebreyesus, M. Scherer, T. Henninger, P. Hyllus, W. Ertmer, L. Santos, and J. J. Arlt, “Parametric Amplification of Vacuum Fluctuations in a Spinor Condensate,” *Phys. Rev. Lett.* **104**, 195303 (2010).
- [68] C. D. Hamley, C. S. Gerving, and T. e. a. T. M. Hoang, “Spin-nematic squeezed vacuum in a quantum gas,” *Nature Phys* **8**, 305 (2012).

- [69] B. Lücke, M. Scherer, J. Kruse, L. Pezzé, F. Deuretzbacher, P. Hyllus, O. Topic, J. Peise, W. Ertmer, J. Arlt, L. Santos, A. Smerzi, and C. Klempt, “Twin Matter Waves for Interferometry Beyond the Classical Limit,” *Science* **334**, 773 (2011).
- [70] H. Strobel, W. Muessel, D. Linnemann, T. Zibold, D. B. Hume, L. Pezzè, A. Smerzi, and M. K. Oberthaler, “Fisher information and entanglement of non-Gaussian spin states,” *Science* **345**, 424 (2014).
- [71] S. S. Szigeti, O. Hosten, and S. A. Haine, “Improving cold-atom sensors with quantum entanglement: Prospects and challenges,” *Appl. Phys. Lett.* **118**, 140501 (2021).
- [72] I. Bloch, J. Dalibard, and W. Zwerger, “Many-body physics with ultracold gases,” *Rev. Mod. Phys.* **80**, 885 (2008).
- [73] M. Vengalattore, J. M. Higbie, S. R. Leslie, J. Guzman, L. E. Sadler, and D. M. Stamper-Kurn, “High-Resolution Magnetometry with a Spinor Bose-Einstein Condensate,” *Phys. Rev. Lett.* **98**, 200801 (2007).
- [74] D. Linnemann, H. Strobel, W. Muessel, J. Schulz, R. J. Lewis-Swan, K. V. Kheruntsyan, and M. K. Oberthaler, “Quantum-Enhanced Sensing Based on Time Reversal of Nonlinear Dynamics,” *Phys. Rev. Lett.* **117**, 013001 (2016).
- [75] L. Deng, E. W. Hagley, J. Wen, M. Trippenbach, Y. Band, P. S. Julienne, J. E. Simsarian, K. Helmerson, S. L. Rolston, and W. D. Phillips, “Four-wave mixing with matter waves,” *Nature* **398**, 218 (1999).
- [76] J. M. Vogels, K. Xu, and W. Ketterle, “Generation of Macroscopic Pair-Correlated Atomic Beams by Four-Wave Mixing in Bose-Einstein Condensates,” *Phys. Rev. Lett.* **89**, 020401 (2002).
- [77] T. W. Hänsch and A. L. Schawlow, “Cooling of gases by laser radiation,” *Opt. Commun.* **13**, 68 (1975).
- [78] D. J. Wineland, R. E. Drullinger, and F. L. Walls, “Radiation-Pressure Cooling of Bound Resonant Absorbers,” *Phys. Rev. Lett.* **40**, 1639 (1978).
- [79] W. D. Phillips and H. Metcalf, “Laser Deceleration of an Atomic Beam,” *Phys. Rev. Lett.* **48**, 596 (1982).
- [80] S. Chu, L. Hollberg, J. E. Bjorkholm, A. Cable, and A. Ashkin, “Three-dimensional viscous confinement and cooling of atoms by resonance radiation pressure,” *Phys. Rev. Lett.* **55**, 48 (1985).
- [81] E. L. Raab, M. Prentiss, A. Cable, S. Chu, and D. E. Pritchard, “Trapping of Neutral Sodium Atoms with Radiation Pressure,” *Phys. Rev. Lett.* **59**, 2631 (1987).

- [82] H. J. Metcalf and P. van der Straten, *Laser Cooling and Trapping* (Springer, New York, NY, USA, 1999).
- [83] K. Dieckmann, R. J. C. Spreeuw, M. Weidemüller, and J. T. M. Walraven, “Two-dimensional magneto-optical trap as a source of slow atoms,” *Phys. Rev. A* **58**, 3891 (1998).
- [84] J. Reichel, W. Hänsel, and T. W. Hänsch, “Atomic Micromanipulation with Magnetic Surface Traps,” *Phys. Rev. Lett.* **83**, 3398 (1999).
- [85] J. J. Arlt, O. Maragò, S. Webster, S. Hopkins, and C. J. Foot, “A pyramidal magneto-optical trap as a source of slow atoms,” *Opt. Commun.* **157**, 303 (1998).
- [86] W. Bowden, R. Hobson, I. R. Hill, A. Vianello, M. Schioppo, A. Silva, H. S. Margolis, P. E. G. Baird, and P. Gill, “A pyramid MOT with integrated optical cavities as a cold atom platform for an optical lattice clock,” *Sci. Rep.* **9**, 1 (2019).
- [87] A. L. Migdall, J. V. Prodan, W. D. Phillips, T. H. Bergeman, and H. J. Metcalf, “First Observation of Magnetically Trapped Neutral Atoms,” *Phys. Rev. Lett.* **54**, 2596 (1985).
- [88] R. Grimm, M. Weidemüller, and Y. B. Ovchinnikov, *Advances In Atomic, Molecular, and Optical Physics* (Academic Press, Cambridge, MA, USA, 2000), Vol. 42, pp. 95–170.
- [89] K. B. Davis, M.-O. Mewes, and W. Ketterle, “An analytical model for evaporative cooling of atoms,” *Appl. Phys. B* **60**, 155 (1995).
- [90] F. Gerbier, A. Widera, S. Fölling, O. Mandel, and I. Bloch, “Resonant control of spin dynamics in ultracold quantum gases by microwave dressing,” *Phys. Rev. A* **73**, 041602 (2006).
- [91] L. Zhao, J. Jiang, T. Tang, M. Webb, and Y. Liu, “Dynamics in spinor condensates tuned by a microwave dressing field,” *Phys. Rev. A* **89**, 023608 (2014).
- [92] M. Gabbrielli, L. Pezzè, and A. Smerzi, “Spin-Mixing Interferometry with Bose-Einstein Condensates,” *Phys. Rev. Lett.* **115**, 163002 (2015).
- [93] Q. Zhang and A. Schwettmann, “Quantum interferometry with microwave-dressed $F = 1$ spinor Bose-Einstein condensates: Role of initial states and long-time evolution,” *Phys. Rev. A* **100**, 063637 (2019).
- [94] S. Levy, E. Lahoud, I. Shomroni, and J. Steinhauer, “The a.c. and d.c. Josephson effects in a Bose–Einstein condensate,” *Nature* **449**, 579 (2007).
- [95] C. K. Law, H. Pu, and N. P. Bigelow, “Quantum spins mixing in spinor Bose-Einstein condensates,” *Phys. Rev. Lett.* **81**, 5257 (1998).

- [96] D. R. Romano and E. J. V. de Passos, “Population and phase dynamics of $F=1$ spinor condensates in an external magnetic field,” *Phys. Rev. A* **70**, 043614 (2004).
- [97] H. Pu, C. K. Law, S. Raghavan, J. H. Eberly, and N. P. Bigelow, “Spin-mixing dynamics of a spinor Bose-Einstein condensate,” *Phys. Rev. A* **60**, 1463 (1999).
- [98] M.-S. Chang, Q. Qin, W. Zhang, L. You, and M. S. Chapman, “Coherent spinor dynamics in a spin-1 Bose condensate,” *Nat. Phys.* **1**, 111 (2005).
- [99] L.-M. Duan, J. I. Cirac, and P. Zoller, “Quantum entanglement in spinor Bose-Einstein condensates,” *Phys. Rev. A* **65**, 033619 (2002).
- [100] H. Pu and P. Meystre, “Creating Macroscopic Atomic Einstein-Podolsky-Rosen States from Bose-Einstein Condensates,” *Phys. Rev. Lett.* **85**, 3987 (2000).
- [101] A. Hansen, J. T. Schultz, N. P. Bigelow, and N. P. Bigelow, “Spin Textures and Topological Excitations in Spinor 87Rb Bose-Einstein Condensates,” *Optical Society of America M6.66* (2013).
- [102] Q. Gu, K. Bongs, and K. Sengstock, “Spin waves in ferromagnetically coupled spinor Bose gases,” *Phys. Rev. A* **70**, 063609 (2004).
- [103] A. Widera, F. Gerbier, S. Fölling, T. Gericke, O. Mandel, and I. Bloch, “Coherent collisional spin dynamics in optical lattices,” *Phys. Rev. Lett.* **95**, 190405 (2005).
- [104] L. Zhao, J. Jiang, T. Tang, M. Webb, and Y. Liu, “Antiferromagnetic spinor condensates in a two-dimensional optical lattice,” *Phys. Rev. Lett.* **114**, 225302 (2015).
- [105] C. Gerving, T. Hoang, B. Land, M. Anquez, C. Hamley, and M. Chapman, “Non-equilibrium dynamics of an unstable quantum pendulum explored in a spin-1 Bose-Einstein condensate,” *Nat. Commun.* **3**, 1169 (2012).
- [106] A. T. Black, E. Gomez, L. D. Turner, S. Jung, and P. D. Lett, “Spinor dynamics in an antiferromagnetic spin-1 condensate,” *Phys. Rev. Lett.* **99**, 070403 (2007).
- [107] W. Zhang, D. L. Zhou, M.-S. Chang, M. S. Chapman, and L. You, “Coherent spin mixing dynamics in a spin-1 atomic condensate,” *Phys. Rev. A* **72**, 013602 (2005).
- [108] S. Yi, Ö. E. Müstecaplıoğlu, C.-P. Sun, and L. You, “Single-mode approximation in a spinor-1 atomic condensate,” *Phys. Rev. A* **66**, 011601(R) (2002).
- [109] M. Scherer, B. Lücke, G. Gebreyesus, O. Topic, F. Deuretzbacher, W. Ertmer, L. Santos, J. J. Arlt, and C. Klempt, “Spontaneous Breaking of Spatial and Spin Symmetry in Spinor Condensates,” *Phys. Rev. Lett.* **105**, 135302 (2010).

- [110] J. Stenger, S. Inouye, D. Stamper-Kurn, H.-J. Miesner, A. Chikkatur, and W. Ketterle, “Spin domains in ground-state Bose–Einstein condensates,” *Nature* **396**, 345 (1998).
- [111] Y. Liu, E. Gomez, S. E. Maxwell, L. D. Turner, E. Tiesinga, and P. D. Lett, “Number Fluctuations and Energy Dissipation in Sodium Spinor Condensates,” *Phys. Rev. Lett.* **102**, 225301 (2009).
- [112] D. Kosloff and R. Kosloff, “A Fourier method solution for the time dependent Schrödinger equation as a tool in molecular dynamics,” *J. Comput. Phys.* **52**, 35 (1983).
- [113] T. J. Park and J. C. Light, “Unitary quantum time evolution by iterative Lanczos reduction,” *J. Chem. Phys.* **85**, 5870 (1986).
- [114] R. Chen and H. Guo, “The Chebyshev propagator for quantum systems,” *Comput. Phys. Commun.* **119**, 19 (1999).
- [115] H. K. Pechkis, J. P. Wrubel, A. Schwettmann, P. F. Griffin, R. Barnett, E. Tiesinga, and P. D. Lett, “Spinor dynamics in an antiferromagnetic spin-1 thermal Bose gas,” *Phys. Rev. Lett.* **111**, 025301 (2013).
- [116] L.-L. Guo, Y.-F. Yu, and Z.-M. Zhang, “Improving the phase sensitivity of an SU(1,1) interferometer with photon-added squeezed vacuum light,” *Opt. Express* **26**, 29099 (2018).
- [117] D. Becker, M. D. Lachmann, S. T. Seidel, H. Ahlers, A. N. Dinkelaker, J. Grosse, O. Hellmig, H. Müntinga, V. Schkolnik, T. Wendrich, A. Wenzlawski, B. Weps, R. Corgier, T. Franz, N. Gaaloul, W. Herr, D. Lüdtke, M. Popp, S. Amri, H. Duncker, M. Erbe, A. Kohfeldt, A. Kubelka-Lange, C. Braxmaier, E. Charron, W. Ertmer, M. Krutzik, C. Lämmerzahl, A. Peters, W. P. Schleich, K. Sengstock, R. Walser, A. Wicht, P. Windpassinger, and E. M. Rasel, “Spaceborne Bose-Einstein condensation for precision interferometry,” *Nature* **562**, 391 (2018).
- [118] V. Shah, R. Lutwak, R. Stoner, and M. Mescher, in *A compact and low-power cold atom clock* (IEEE, Baltimore, MD, 2012), pp. 1–6.
- [119] S. C. Bell, M. Junker, M. Jasperse, L. D. Turner, Y.-J. Lin, I. B. Spielman, and R. E. Scholten, “A slow atom source using a collimated effusive oven and a single-layer variable pitch coil Zeeman slower,” *Rev. Sci. Instrum.* **81**, 013105 (2010).
- [120] G. E. Marti, R. Olf, E. Vogt, A. Öttl, and D. M. Stamper-Kurn, “Two-element Zeeman slower for rubidium and lithium,” *Phys. Rev. A* **81**, 043424 (2010).
- [121] Y. Castin and R. Dum, “Bose-Einstein Condensates in Time Dependent Traps,” *Phys. Rev. Lett.* **77**, 5315 (1996).

- [122] I. Morgenstern, S. Zhong, Q. Zhang, L. Baker, J. Norris, B. Tran, and A. Schwettmann, “A versatile microwave source for cold atom experiments controlled by a field programmable gate array,” *Rev. Sci. Instrum.* **91**, 023202 (2020).
- [123] J. Dalibard and C. Cohen-Tannoudji, “Laser cooling below the Doppler limit by polarization gradients: simple theoretical models,” *J. Opt. Soc. Am. B, JOSAB* **6**, 2023 (1989).
- [124] R. Dumke, M. Johanning, E. Gomez, J. D. Weinstein, K. M. Jones, and P. D. Lett, “All-optical generation and photoassociative probing of sodium Bose–Einstein condensates,” *New J. Phys.* **8**, 64 (2006).
- [125] J. Jiang, L. Zhao, M. Webb, N. Jiang, H. Yang, and Y. Liu, “Simple and efficient all-optical production of spinor condensates,” *Phys. Rev. A* **88**, 033620 (2013).

Appendix A

Publications

A.1 Introduction

This Appendix contains lists of my publications and presentations.

A.2 Publications

2. I. Morgenstern, S. Zhong, Q. Zhang, L. Baker, J. Norris, B. Tran, A. Schwettmann, “A versatile microwave source for cold atom experiments controlled by a field programmable gate array,” *Rev. Sci. Instrum.* **91**, 023202 (2020).
1. Q. Zhang and A. Schwettmann, “Quantum interferometry with microwave-dressed $F = 1$ spinor Bose-Einstein condensates: Role of initial states and long-time evolution,” *Phys. Rev. A* **6**, 063637 (2019).

A.3 Presentations

Following is a list of presentations that I gave or contributed to, in reverse chronological order.

14. Q. Zhang, S. Zhong, J. Jie, Q. Guan, I. Morgenstern, H. Ooi, A. Bhagat, D. Nematollahi, H. Lee, D. Blume, A. Schwettmann, “Microwave Control of Spin Dynamics in $F=1$ Sodium Spinor Bose-Einstein Condensates,” DAMOP, Portland, OR (2020). (Poster)
13. S. Zhong, J. Jie, Q. Guan, Q. Zhang, I. Morgenstern, H. G. Ooi, A. Bhagat, D. Nematollahi, H. Lee, D. Blume, and A. Schwettmann, “Spin dynamics beyond the single mode approximation in a sodium spinor BEC,” DAMOP, Portland, OR (2020). (Talk)
12. Q. Zhang, S. Kim, M. Peters, A. M. Marino, and A. Schwettmann, “Experimental Investigation of Four-Wave Mixing in Hot Sodium Vapor Cells,” DAMOP, Milwaukee, WI (2019). (Talk)

11. S. Zhong, Q. Zhang, I. Morgenstern, H. Ooi, and A. Schwettmann, “Atomic Interferometry in Antiferromagnetic Spinor BECs in the Regime of long Evolution Time,” DAMOP, Milwaukee, WI (2019). (Talk)
10. H. Ooi, Q. Zhang, S. Kim, A. M. Marino, and A. Schwettmann, “Four-Wave Mixing in Hot Sodium Vapor Cells with Saturated Absorption,” DAMOP, Milwaukee, WI (2019). (Poster)
9. I. Morgenstern, S. Zhong, Q. Zhang, and A. Schwettmann, “Improved FPGA-Controlled Microwave source for Cold Atom Experiments,” DAMOP, Milwaukee, WI (2019). (Poster)
8. Q. Zhang, S. Kim, L. Narcomey, A. M. Marino, and A. Schwettmann, “Four-wave Mixing in Hot Sodium Vapor Cells,” DAMOP, Ft. Lauderdale, FL (2018). (Poster)
7. S. Zhong, Q. Zhang, I. Morgenstern, H. Ooi, L. Baker, J. Kittel, and A. Schwettmann, “Quantum Interferometry with Microwave-dressed Spinor Bose-Einstein Condensate in the Regime of Long Evolution Time,” DAMOP, Ft. Lauderdale, FL (2018). (Poster)
6. I. Morgenstern, S. Zhong, Q. Zhang, L. Baker, J. Norris, B. Tran, and A. Schwettmann, “FPGA-Controlled Versatile Microwave Source for Cold Atom Experiments,” DAMOP, Ft. Lauderdale, FL (2018). (Poster)
5. Q. Zhang, A. Schwettmann, and E. Tiesinga, “Quantum Interferometry with Microwave-dressed $F=1$ Spinor Bose-Einstein Condensates: Role of Initial States and Long Time Evolution,” DAMOP, Sacramento, CA (2017). (Talk)
4. S. Zhong, A. Bhagat, Q. Zhang, and A. Schwettmann, “Improved Apparatus to Study Matter-Wave Quantum Optics in Sodium Spinor Bose-Einstein Condensate,” DAMOP, Sacramento, CA (2017). (Poster)
3. Q. Zhang, D. Nematollahi, A. Schwettmann, and E. Tiesinga, “Collisional Spin Evolution in Microwave-dressed $F=1$ Spinor Bose-Einstein Condensates,” DAMOP, Providence, RI (2016). (Poster)
2. D. Nematollahi, Q. Zhang, J. Altermatt, S. Zhong, M. Goodman, A. Bhagat, and A. Schwettmann, “Appratus to Study Matter-wave Quantum Optics in Spin Space in a Sodium Spinor Bose-Einstein Condensate,” DAMOP, Providence, RI (2016). (Poster)
1. D. Nematollahi, A. Foster, K. Yates, J. Altermatt, H. Lee, Q. Zhang, and A. Schwettmann, “Experimental apparatus to study cold collisions in sodium spinor Bose-Einstein condensates,” DAMOP, Columbus, OH (2015). (Poster)